

Accurate estimation of large vessel length in growing children and adolescents for the purpose of pulse wave velocity calculation.

by

Lee-Roy C. Witbooi



Thesis presented in fulfilment of the requirements for the degree Master of Anatomy at
Stellenbosch University

iyUNIVESITHI
STELLENBOSCH
UNIVERSITY



Supervisor: Prof, S. Innes

Co-supervisors: Prof, B. Page & Prof, R. Pitcher

December 2018

DECLARATION

By submitting this assignment/thesis/dissertation electronically, I declare that the entirety of the work contained therein is my own, original work, that I am the sole author thereof (save to the extent explicitly otherwise stated), that reproduction and publication thereof by Stellenbosch University will not infringe any third party rights and that I have not previously in its entirety or in part submitted it for obtaining any qualification.

Date: December 2018

ABSTRACT

Background

Cardiovascular disease is a major cause of death in adults worldwide. Early detection allows for early intervention to prevent vascular events such as strokes, heart attacks, etc. Although these vascular events typically occur in late adulthood, the underlying atherosclerosis often begins during childhood. Early subclinical atherosclerosis can be detected by measuring the elasticity of the large arteries, particularly when performed serially over time. Normally, the elasticity of a healthy aorta helps to slow down the speed of the pressure wave created by contraction of the heart muscle. This is an important way of maintaining smooth laminar blood flow.

Atherosclerosis causes the vessel wall to harden and lose elasticity. As the vessel wall hardens, the speed of the pressure wave increases.

Pulse wave velocity (PWV) is a sophisticated method of detecting early elasticity changes, and is a preferred non-invasive technique to measure arterial wall stiffness. The velocity calculation requires accurate measurement of both distance travelled and time taken for the pulse wave to travel between two points. The distance used for pulse wave velocity calculation is an approximation of the intraluminal distance travelled by the pulse wave and is estimated by measuring the distance between various surface anatomy landmarks. The expert consensus document on arterial wall stiffness described carotid–femoral PWV as the “gold standard” measurement of arterial wall stiffness, yet there is no consensus on the arterial path length estimation method. A variety of arterial path length estimation methods exist, and this makes inter-study comparison of PWV very difficult.

The purpose of the current study was to investigate the most accurate method of estimating the true distance travelled by the aorto-femoral pressure wave. We compared distances between a range of commonly used surface anatomy landmarks, and compared these to the true intraluminal distance measured on multi-planar reformations of archived computerized tomography imaging in children of varying ages. Our findings will allow standardization of PWV calculation in children and allow for inter-study comparisons.

Methods

Vessel lengths in children (aged 0-18 years) were measured with multi-planar reformation (MPR) imaging software. These measurements were then compared with the surface anatomy measurements also obtained using the MPR imaging software. The comparisons between vessel lengths and surface anatomy distances were performed in segments, since there were no whole body CT scans available on the Picture Archiving and Communication System (PACS) at the research site.

Results

The surface anatomy measurements from the suprasternal notch to the angle of the mandible (on the right) correlated well with the intraluminal vessel length from the origin of the brachiocephalic trunk to the external carotid at the angle of the mandible ($r^2=0.92$; $p<0.0001$). The surface anatomy measurements from the suprasternal notch to the midpoint of the right inguinal crease, correlated well with the intraluminal vessel length from the origin of the brachiocephalic trunk to the right femoral artery at the right inguinal ligament ($r^2=0.98$; $p<0.0001$). The surface anatomy measurements from the suprasternal notch to the xiphisternum, plus the surface distance between xiphisternum and the umbilicus, plus the surface distance between the umbilicus and the midpoint of the right inguinal crease, correlated well with the intraluminal vessel length from the origin of the brachiocephalic trunk to the right femoral artery at the right inguinal ligament ($r^2=0.97$; $p<0.0001$). The surface anatomy measurement from the suprasternal notch to the xiphisternum, plus the surface distance between the xiphisternum and the midpoint of right inguinal crease, correlated well with the intraluminal vessel length from the origin of the brachiocephalic trunk to the right femoral artery at the right inguinal ligament ($r^2=0.97$; $p<0.0001$). A regression equation is provided for each set of surface anatomy measurements, allowing further adjustment of measurements to more accurately represent the true intraluminal distance travelled by the pulse wave.

Conclusions

The surface anatomy distance between the suprasternal notch and the angle of the mandible, subtracted from the distance between the suprasternal notch and mid-inguinal crease, provides the closest approximation of true intraluminal distance travelled and would be the best method to standardize pulse wave velocity calculation in children and adolescents. However, surface anatomy estimations using the xiphisternum and umbilicus as landmarks produced very similar correlations.

UITREKSEL

Agtergrond

Kardiovaskulêre siekte is een van die voorste oorsake van dood in volwassenes wêreldwyd. Vroeë opsporing maak voorsiening vir vroeë intervensie om vaskulêre gebeure soos beroertes, hartaanvalle, ens. te voorkom. Alhoewel hierdie vaskulêre gebeure tipies in die laat volwassenheid voorkom, begin die onderliggende aterosklerose dikwels gedurende die kinderjare. Vroeë subkliniese aterosklerose kan opgespoor word deur die elastisiteit van arteries te meet, met jaarlikse opvolg ondersoeke. Die elastisiteit van 'n gesonde aorta help om die spoed van die pols wat deur die samespanning van die hartspier geskep word, te vertraag. Dit is 'n belangrike manier om egalige laminêre bloedvloei te handhaaf. Aterosklerose veroorsaak dat bloedvate verhard en elastisiteit verloor. Soos die bloedvate verhard, verhoog die pols spoed.

Pols spoed/snelheid berekenings ondersoeke is 'n gesofistikeerde metode om vroeë bloedvaat elastisiteits veranderings op te spoor, en is vir baie die ondersoek van keuse om vir arteriële bloedvaat styfheid te meet. Die snelheidsberekening vereis akkurate meting van beide afstand agelê en tyd wat dit neem vir die pols om tussen twee punte te beweeg. Die afstand wat gebruik word vir hierdie ondersoek is 'n skatting en word gemeet met behulp van 'n maatband oor die liggaamsoppervlak. Die deskundige konsensus dokument oor arteriële bloedvat styfheid beskryf karotis-femorale pols snelheids berekenings ondersoek as die "gouestandaard" meting vir arteriële wandstyfheid, maar daar is geen konsensus oor die arteriële padlengte skattingsmetode nie. 'n Verskeidenheid van arteriële padlengte skattings metodes bestaan, en dit maak inter-studie vergelyking in verband met pols snelheid berekenings baie moeilik.

Die doel van hierdie studie was om die akkuraatste skattings metode van afstand wat deur die aorto-femorale pols afgelê word te ondersoek, deur oppervlakanatomiese afstande, wat verkry is met behulp van 3D rekenaar tomografie (RT) beelde, te vergelyk met bloedvaat lengtes wat verkry was met behulp van multi-planêre rekonstruksie rekenaar tomografie beelde in kinders van verskillende ouderdomme. Om sodoende pols snelheid berekenings ondersoeke in kinders te standaardiseer en inter-studie vergelykings in verband met pols snelheid berekenings te vergemaklik.

Metodes

Bloedvaat lengtes is gemeet met behulp van multi-planêre rekonstruksie (MPR) beeldings sagteware (IntelliSpace Portal, Koninklike Philips elektroniese NV, Nederland) by kinders (tussen die ouderdomme 0 tot 18 jaar). Hierdie metings is dan vergelyk met die oppervlakanatomie metings wat ook verkry is met behulp van die MPR beeldings sagteware. Hierdie vergelykings is in segmente uitgevoer, aangesien daar geen RT-skanderings beskikbaar was, wat vanaf die basis van die skedel tot by die pelvis strek nie, by die hospitaal waar die studie uitgevoer was nie.

Resultate

Die oppervlakanatomiese meting vanaf die suprasternale kerf tot by die hoek van die mandibel (regs) het positief gekorreleer met die bloedvaat metings vanaf die oorsprong van die brachiokefaliese stam tot by die eksterne karotis by die hoek van die mandibel ($r^2 = 0.92$; $p < 0,0001$). Die oppervlaksanatomiese meting vanaf die suprasternale kerf tot by die middelpunt van die lies vou, het positief gekorreleer met die bloedvaat metings vanaf die oorsprong van die brachiokefaliese stam tot by die regter femorale arterie by die inguinale ligament ($r^2 = 0.98$; $p < 0,0001$). Die oppervlakanatomiese meting vanaf die suprasternale kerf tot by die xifisternum, plus die oppervlakafstand vanaf die xifisternum tot by die umbilikus, plus die oppervlakafstand vanaf die umbilikus tot by die middelpunt van die regter lies vou, positief gekorreleer met die bloedvaatmetings vanaf die oorsprong van die brachiokefaliese stam tot by die regter femorale arterie by die inguinale ligament ($r^2 = 0.97$; $p < 0,0001$). Die oppervlaksanatomiese meting vanaf die suprasternale kerf tot by die xifisternum, plus die oppervlakafstand vanaf die xifisternum tot by die middelpunt van die lies vou het positief gekorreleer met die bloedvaat metings vanaf die oorsprong van die brachiokefaliese stam tot die regter femorale arterie by die inguinale ligament ($r^2 = 0,97$; $p < 0,0001$). 'n Formule word verskaf vir elke stel oppervlakanatomie metings, wat die aanpassing van metings moontlik maak om die ware intraluminale afstand wat deur die pols aglê word, meer akkuraat voor te stel.

Gevolgtrekkings

Die oppervlak anatomie afstand tussen die suprasternale kerf en die hoek van die mandibel moet afgetrek word van die afstand tussen die suprasternale kerf en die regter lies vou, aangesien dit die naaste benadering bied van ware intraluminale afstand agelê en sal die beste metode wees om pols snelheid ondersoek in kinders and adolessente te standaardiseer.

ACKNOWLEDGEMENTS

First and foremost, I would like to thank God for his never-ending grace, mercy, and provisions during what ended up being one of the toughest times of my life.

I would also like to thank my supervisors (in no particular order), Prof Steve Innes, Prof Ben Page and Prof Richard Pitcher for their guidance, expert advice and encouragement throughout this difficult project. I look forward to collaborating with all of you in the near future again.

Nobody has been more important to me in the pursuit of this project than the members of my family. I would like to thank my grandparents, whose love and guidance are with me in whatever I pursue. They are the ultimate role models. Most importantly, I wish to thank my loving and supportive wife, Chantol, and my two wonderful children, Lynn and Chad, who provide unending inspiration.

CONTENTS

CHAPTER 1	1
1.1 LITERATURE REVIEW	1
1.1.1 Carotid–femoral Pulse wave velocity	1
1.1.2 Anatomy to be estimated: Aorta	3
1.1.3 Atherosclerosis and the aorta	6
1.1.4 Effect of atherosclerosis on the pulse	10
1.1.5 Basic principles of multidetector-row helical computed tomography (CT)	11
1.1.5.1 Multi-planar Reformation	16
1.1.5.2 Principles of CT Angiography (CTA)	18
1.1.5.3 Ionizing radiation	19
CHAPTER 2	20
2.1 MATERIAL AND METHODS	20
2.1.1.1 Background: estimation of the true distance travelled	20
2.1.1.2 Background: surface anatomy landmarks for pulse wave velocity.	22
2.1.2 Research design	27
2.1.2.1 Six surface anatomy distance points	28
2.1.2.2 Six large vessel distance points	28
2.1.2.3 Data sets and respective comparisons	29
2.1.3 Methods of data collection	34

2.1.3.1 Measuring the vessel distance between the origin of the brachiocephalic trunk to the external carotid artery (at angle of mandible) via the right common carotid artery (TC+CB+BE).	34
2.1.3.2 Measuring the surface anatomy distance between the angle of the mandible to the suprasternal notch (AS).	36
2.1.3.3 Vessel distance between the origin of the brachiocephalic trunk to the aorta at the xiphisternum (TX).	38
2.1.3.4 Measuring the surface anatomy distance between the suprasternal notch to the xiphisternum (SX).	40
2.1.3.5 Measuring the vessel distance between the aorta at the xiphisternum to the aortic bifurcation, and from the aortic bifurcation to the right femoral artery at the right inguinal ligament (XA+AF).	42
2.1.3.6 Measuring the surface anatomy distance from the xiphisternum to the midpoint of the right inguinal crease (XI).	43
2.1.3.7 Measuring the surface anatomy distance from the xiphisternum to the umbilicus and the distance between the umbilicus to the midpoint of the right inguinal crease (XU+UI).	44
2.1.3.8 Vessel distance between the origin of the brachiocephalic trunk to the aortic bifurcation, and from the aortic bifurcation to right femoral artery at the inguinal ligament (TX+XA +AF).	45
2.1.3.9 Measuring the surface anatomy distance between the suprasternal notch to the midpoint of the right inguinal crease (SI).	47
2.1.3.10 Measuring the surface anatomy distance between the suprasternal notch to the xiphisternum, and the surface distance between xiphisternum and the midpoint of the right inguinal crease (SX+XI).	48

2.1.3.11 Measuring the surface anatomy distance between the suprasternal notch and the xiphisternum, and the surface distance between xiphisternum and the umbilicus, plus the surface distance between the umbilicus and the midpoint of the right inguinal crease (SX+ XU+UI).	49
CHAPTER 3	50
3.1 RESULTS	50
3.1.1 Scatterplot of TC+CD+BE compared to AS	52
3.1.2 Scatterplot of TX compared to SX	53
3.1.3 Scatterplot of XA+AF compared to XI	54
3.1.4 Scatterplot of XA +AF compared to XU+UI	55
3.1.5 Scatterplot of TX+XA+AF compared to SI	56
3.1.6 Scatterplot of TX+XA+AF compared to SX+XI	57
3.1.7 Scatterplot of TX+XA+AF compared to SX+XU+UI	58
3.2 Summary of results	59
CHAPTER 4	61
4.1 DISCUSSION	61
CHAPTER 5	64
5.1 CONCLUSION	64
6. REFERENCES	65

TABLES

1.1 Distinguishing features of arteries.	8
2.1 Six surface anatomy distances used for PWV calculations, with associated abbreviations.	28
2.2 Six large vessel distances used for PWV calculation, with associated abbreviations.	28
2.3 Data sets and respective comparisons.	29
3.1 Demographics for each comparison group.	50
3.2 Summary outcome of each comparison.	59

FIGURES

1.1: Anterior view of the aortic arch and it's branches.	3
1.2: Right lateral view of the brachiocephalic trunk and it's branches in the neck (a). Anterior view of the brachiocephalic trunk and its branches (b).	4
1.3: Lateral view of the thoracic aorta.	5
1.4: Detailed anterior view of the abdominal aorta and it's branches.	5
1.5: Anterior view of the abdominal aorta	6
1.6: Basic structure on arteries.	7
1.7: Photomicrographs of a transverse section of a healthy artery (a) and a partially obstructed artery (b).	9
1.8: Layers of the heart wall.	10
1.9: Illustrating the pulse point of the common carotid artery, lateral to the larynx (a) and the right femoral artery, inferior to the inguinal ligament (b).	11
1.10: Illustrating the x-ray tube movement and patient/couch movement.	13
1.11: Illustration of the difference between spiral and helical.	13
1.12: Image of slip-rings inside the gantry.	14

1.13: Illustrating interpolated data between known data points.	15
1.14: Illustration of a solid state detector, with its scintillating material and photodiode	15
1.15: Illustration of a multidetector array, with thousands of individual detectors.	16
1.16: An anterior view of a MIP (a), SSD of the colon (b) and anterior view of a volume rendering display (c).	17
2.1: The true intraluminal distance travelled by the pressure wave for carotid-femoral PWV calculations, are demonstrated by the blue arrows	21
2.2: Axial (a) and sagittal (b) view of the right internal and external carotid arteries.	22
2.3: Lateral view of the external and internal carotid arteries.	23
2.4: Anterior view of the sternum and it's three parts.	23
2.5: Details of the umbilical cord.	24
2.6: Surface marking of the aortic bifurcation (5).	25
2.7: Anterosuperior view of the pelvis.	26
2.8: Medial view of the pelvic bone.	27
2.9: Surface marking of the superior anterior iliac spine (1), pubic tubercle (3) and femoral arteries (7).	27
2.10: Illustration of comparison, TC+CD+BE to AS.	30
2.11: Illustration of comparison, TX to SX.	31
2.12: Illustration of comparison, XA+AF to XI.	31
2.13: Illustration of comparison, XA+AF to XU+UI.	32
2.14: Illustration of comparison, TX+XA+AF to SI.	32
2.15: Illustration of comparison, TX+XA+AF to SX+XI.	33
2.16: Illustration of comparison, TX+XA+AF to SX+XU+UI.	33

- 2.17: Illustrating the placement of the first marker (seed) on the coronal (a), sagittal (b) and axial (c) images, for measurements starting at the brachiocephalic trunk. 35
- 2.18: Illustration of vessel centerline TC+CD+BE on a curved coronal (a), and on a curved sagittal (b) MPR. 36
- 2.19: Illustrating surface measurement AS on an AP 3D volume rendered image (a) and a lateral 3D volume rendered image (b), using magic glass. 37
- 2.20: Illustrating surface measurement AS on an oblique 3D volume rendered image (a) and an AP 3D volume rendered images (b), after the magic glass have been removed. 38
- 2.21: Illustrating the start and end points of the vessel measurement TX on a lateral view of a 3D volume rendered image. 39
- 2.22: Illustrating the start and end points of the vessel measurement TX on a sagittal curved MPR view. 39
- 2.23: Illustrating the start and end point of the vessel measurement TX on an oblique view of a 3D volume rendered image, and illustrating the upper edge of T10. 40
- 2.24: Illustrating surface measurement SX, using the magic glass. 41
- 2.25: Illustrating surface measurement SX, after the magic glass has been removed. 41
- 2.26: Illustrating how to estimate the position of the inguinal ligament. 42
- 2.27: Illustrating the start and end points of the vessel measurement XI on a coronal (a) and sagittal (b) curved MPR. 43
- 2.28: Illustration of surface measurement XI (a), and this was compared to vessel distance XA+AF in red (b). 44
- 2.29: Illustration of surface measurement XU+UI (a), and this was compared to vessel distance XA+AF in red (b). 45
- 2.30: Demonstration of the intra-arterial path length on a curved multi-planar reformat (a & c) and on a lateral volume rendered image (b), starting at the origin of the brachiocephalic trunk and ending in the right femoral artery. 46
- 2.31: Illustration of surface measurement SI, using the magic glass (a), and then displaying the distance after the magic glass has been removed (b). 47
- 2.32: Illustration of surface measurement SX+XI, using the magic glass (a), and then displaying the distances after the magic glass has been removed (b). 48

2.33: Illustration of surface measurement $SX+XU+XI$, using the magic glass (a), and then displaying the distances after the magic glass has been removed (b).	49
3.1: Age for each comparison group.	50
3.2: Percentage of male and female for each comparison.	51
3.3: Scatterplot of $TC+CD+BE$ compared to AS	52
3.4: Scatterplot of TX compared to SX	53
3.5: Scatterplot of $XA+AF$ compared to XI	54
3.6: Scatterplot of $XA+AF$ compared to $XU+UI$	55
3.7: Scatterplot of $TX+XA+AF$ compared to SI	56
3.8: Scatterplot of $TX+XA+AF$ compared to $SX+XI$	57
3.9: Scatterplot of $TX+XA+AF$ compared to $SX+ XU+UI$	58

LIST OF ABBREVIATIONS

3D	THREE-DIMENSIONAL
AF	AORTIC BIFURCATION TO RIGHT FEMORAL ARTERY AT INGUINAL LIGAMENT
ALARA	AS LOW AS REASONABLY ACHIEVABLE
AP	ANTERIOR-POSTERIOR
BE	CAROTID BIFURCATION TO EXTERNAL CAROTID AT ANGLE OF MANDIBLE
BMI	BODY MASS INDEX
CB	ORIGIN OF RIGHT COMMON CAROTID TO CAROTID BIFURCATION
CT	COMPUTED TOMOGRAPHY
CTA	COMPUTED TOMOGRAPHY ANGIOGRAPHY
DAS	DATA ACQUISITION SYSTEM
FMD	FLOW-MEDIATED DILATATION
IMT	INTIMA-MEDIA THICKNESS
IQR	INTERQUARTILE RANGE
MIP	MAXIMUM INTENSITY PROJECTION
MPR	MULTI-PLANAR REFORMATION
MRI	MEGNATIC RESONANCE IMAGING
PWV	PULSE WAVE VELOCITY
SI	SUPRASTERNAL NOTCH TO MIDPOINT OF THE RIGHT INGUINAL CREASE
SSD	SHADED SURFACE DISPLAY
SVD	SHADED VOLUME DISPLAY
SX	SUPRASTERNAL NOTCH TO XIPHISTERNUM
T10	TENTH THORACIC VERTEBRAE
TC	ORIGIN OF BRACHIOCEPHALIC TRUNK TO ORIGIN OF RIGHT COMMON CAROTID
TX	ORIGIN OF BRACHIOCEPHALIC TRUNK TO AORTA AT THE XIPHISTERNUM

UI	UMBILICUS TO MIDPOINT OF THE RIGHT INGUINAL CREASE
XA	AORTA AT THE XIPHISTERNUM TO AORTIC BIFURCATION
XI	XIPHISTERNUM TO MIDPOINT OF THE RIGHT INGUINAL CREASE
XU	XIPHISTERNUM TO UMBILICUS

CHAPTER 1

1.1 LITERATURE REVIEW

This chapter describes the purpose of pulse wave velocity calculations. The chapter then looks at the anatomy and histology of the elastic and muscular arteries. The focus then shifts to atherosclerosis and the basic principles of computerized tomography (CT), as all measurements will be performed on CT images.

PubMed (<https://www.ncbi.nlm.nih.gov.ez.sun.ac.za/pubmed>) was used on the World Wide Web to search for electronic journal articles on these topics. Articles were sourced through the University of Stellenbosch University Faculty of Health Sciences library website (<http://library.sun.ac.za>). Electronic copies of journal articles were downloaded and saved. Text books were provided by the Health Sciences library, Stellenbosch University.

1.1.1 Carotid–femoral Pulse wave velocity

Carotid–femoral Pulse wave velocity (PWV) is considered the “gold standard” for measuring arterial wall stiffness (Laurent et al., 2006), which is a reliable method of monitoring for and identifying the early stages of atherosclerosis. Identifying atherosclerosis early in its pathogenesis allows early intervention to prevent progression of atherosclerotic vascular disease. Interventions may include: balanced diets, regular exercise, anti-smoking campaigns or even drug treatments. The pulse wave velocity calculation gives clinicians a good idea of the distensibility of a vessel, by measuring the velocity at which the arterial pulse wave travels through the circulatory system. A stiffer vessel will have a faster pulse wave velocity compared to a healthy (more elastic) vessel. This highly reproducible technique involves measuring the time it takes the arterial pulse to travel a specific distance, and then dividing the distance by the time, to calculate the velocity. Time is obtained by measuring the interval delay between the pulse wave arriving at a proximal and distal sensor that are placed on fiducial points, most commonly over the external carotid and femoral arteries. Arrival of the pulse wave is identified using various devices that monitor the arterial pressure waveform, such as the Vicorder® applanation tonometry device (SMART Medical: Moreton-in-Marsh, United Kingdom). The

distance used for pulse wave velocity calculations is an estimate of the distance travelled by the pulse wave and is obtained using a tape measure over the body surface.

However a variety of arterial path length estimation methods exist. Many studies have already highlighted the importance of standardizing methodologies, as the use of different arterial path length estimations produces noticeable different results. (Surgawara et al, 2010) (Weber, Ammer, Rammer, Adji, O'Rourke, Wassertheurer, Rosenkranz, Eber, Bernd: 2009). This makes inter-study comparisons of PWV data very difficult and creates confusion regarding normal values for PWV in children of different ages.

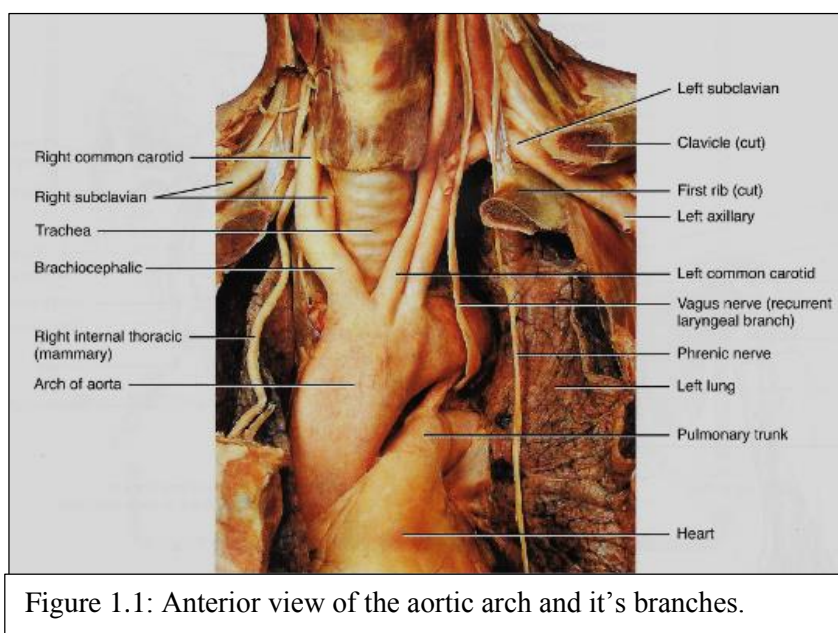
Results from a study conducted in adults by Weber et al (2009) indicated that subtracting the distance from the carotid location to the sternal notch from the distance between the sternal notch and the femoral site of measurement, would provide the best estimate of true distance travelled by the pulse wave, used in carotid-femoral PWV calculation. In contrast, results from a study by Sugawara et al (2010), indicate that the carotid-suprasternal notch distance be subtracted from carotid-femoral distance, provided the closest approximate in adults. However, both of these studies were done in adults, and there is a lack of similar studies in children.

Alternatives to pulse wave velocity include arterial ultrasonography examinations such as intima-media thickness (IMT), where the thickness of the tunica intima and the tunica media is measured, and flow-mediated-dilation (FMD), where artery dilation is measured when blood flow increases. These ultrasound examinations have high prognostic value, however these techniques are highly operator dependent and require a high degree of technical expertise, which limit reproducibility. In addition, they may take longer to perform and may be subject to operator bias. Pulse wave velocity calculations are easier to perform; the fully automated Vicorder device is highly reproducible and has high prognostic value compared to other noninvasive techniques used for detecting sub-clinical atherosclerosis.

1.1.2 Anatomy to be estimated: Aorta

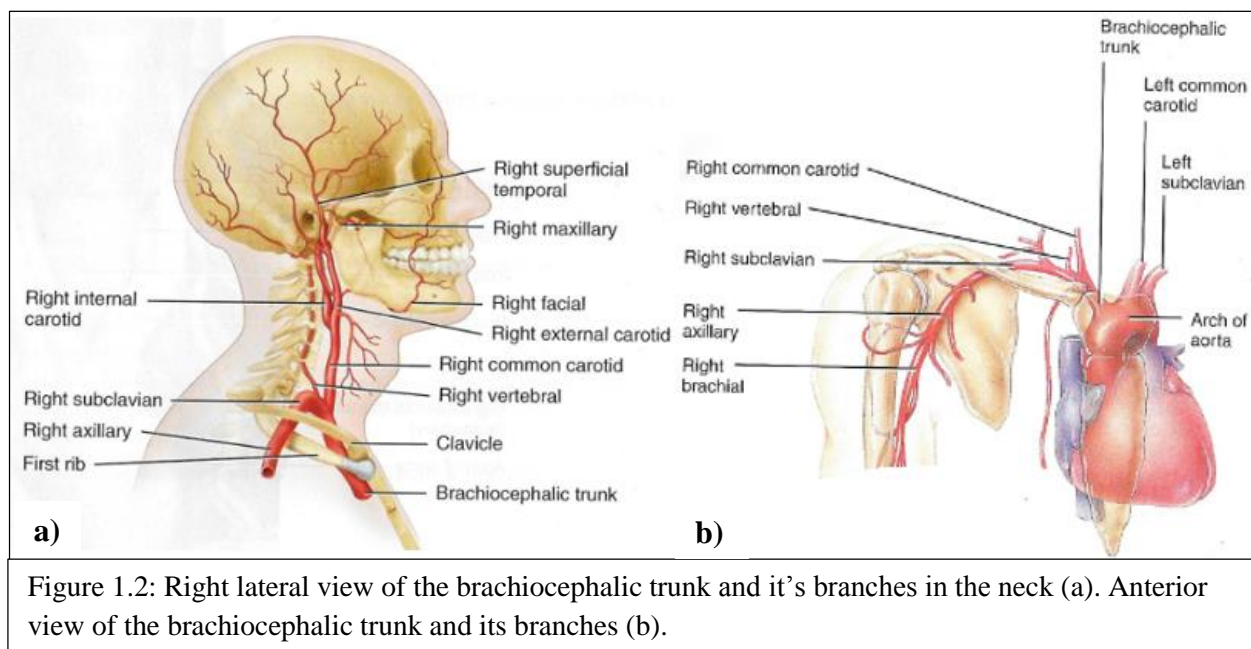
Traditional methods of estimating distance travelled by the pulse wave are likely to be inaccurate, since an assumption is made that the aorta and major vessels are straight, where in fact the aorta follows the shape of the vertebral column, with its lordotic curve and kyphotic curve. Change in the direction of blood flow at bifurcations is also not considered.

According to Tortora & Derrickson (2011:831-832), the aorta ascends from the left ventricle alongside the pulmonary trunk (ascending aorta). It then curves to the left and posteriorly over the pulmonary bifurcation towards the vertebral column (arch of the aorta). There are three major branches that originates from the aortic arch, they are the brachiocephalic artery, the left common carotid artery and the left subclavian artery as shown in figure 1.1.



(Tortora & Derrickson, 2011: 836)

The first branch of the aortic arch that extends superiorly and that slightly bends to the right is called the brachiocephalic trunk (figure 1.1 & 1.2). It is the largest branch of the aortic arch and divides into the right subclavian artery and the common carotid artery, posterior to the right sternoclavicular joint (figure 1.2b). The common carotid artery in turns divides into the internal and external carotid arteries at the superior border of the larynx (1.2a). Just anterior to the sternocleidomastoid muscle at the superior border of the larynx, the carotid pulse can be felt in the external carotid artery. (Tortora & Derrickson, 2011: 832)



(Tortora & Derrickson, 2011: 835)

From the level of the fourth or fifth thoracic vertebrae, the aorta descends caudally in close proximity to the thoracic vertebral bodies (thoracic aorta) see figure 1.3. It then passes through the diaphragm (aortic hiatus) and follows the vertebral column to the level of the fourth lumbar vertebra where it divides into the two common iliac arteries. The section between the Aortic hiatus and the bifurcation is called the abdominal aorta, as shown in figure 1.4 and 1.5 (Tortora & Derrickson, 2011:837-839).

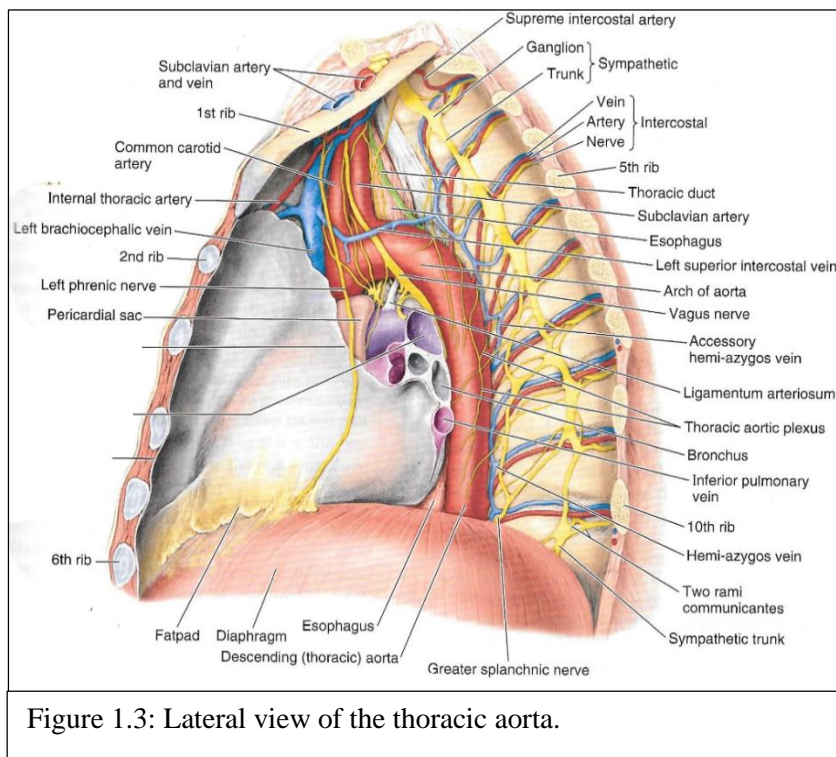


Figure 1.3: Lateral view of the thoracic aorta.

(Moore, Dally & Agur, 2014: 167)

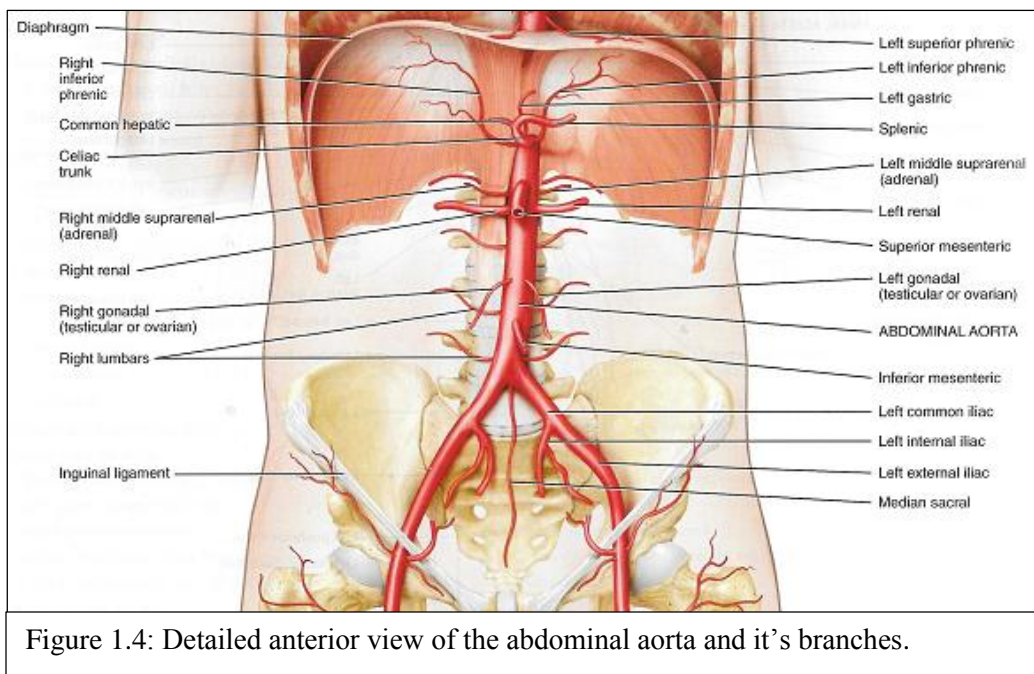
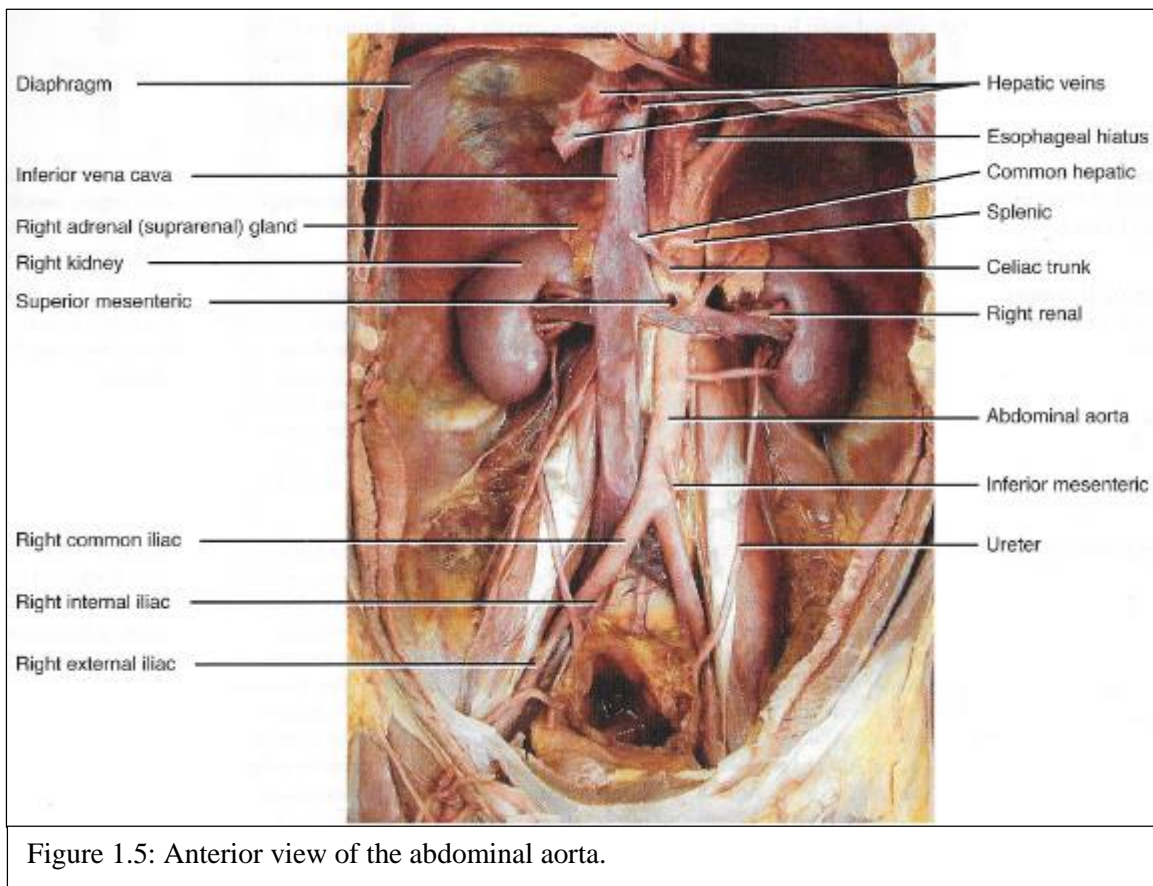


Figure 1.4: Detailed anterior view of the abdominal aorta and its branches.

(Tortora and Derrickson, 2011: 830)



(Tortora and Derrickson, 2011: 843)

1.1.3 Atherosclerosis and the aorta

The tunica intima, tunica media and the tunica externa are the three layers of an artery (figure 1.6). The tunica intima is the inner-most coat and contains a lining of endothelium (simple squamous epithelium), a basement membrane as well as a layer of elastic tissue (intima elastic). This is the layer that is the closest to the lumen. The tunica media is the thickest layer and consists of elastic fibre and smooth muscle fibres. The walls of the arteries easily stretch without tearing in response to a small increase in pressure, because it has plentiful elastic fibres. The tunica externa is the outermost layer of an artery and it consists of elastic and collagen fibres. (Tortora & Grabowski, 2003:697)

Because the tunica media contains a high proportion of elastic fibres, the largest-diameter arteries are called the elastic arteries. The elastic arteries help the propel blood onwards while the ventricles are relaxing. “As the blood is ejected from the heart into elastic arteries, their high

elastic wall stretch accommodates the surge of blood". The elastic fibres function as a pressure reservoir for a short time. (Tortora & Grabowski, 2003:697).

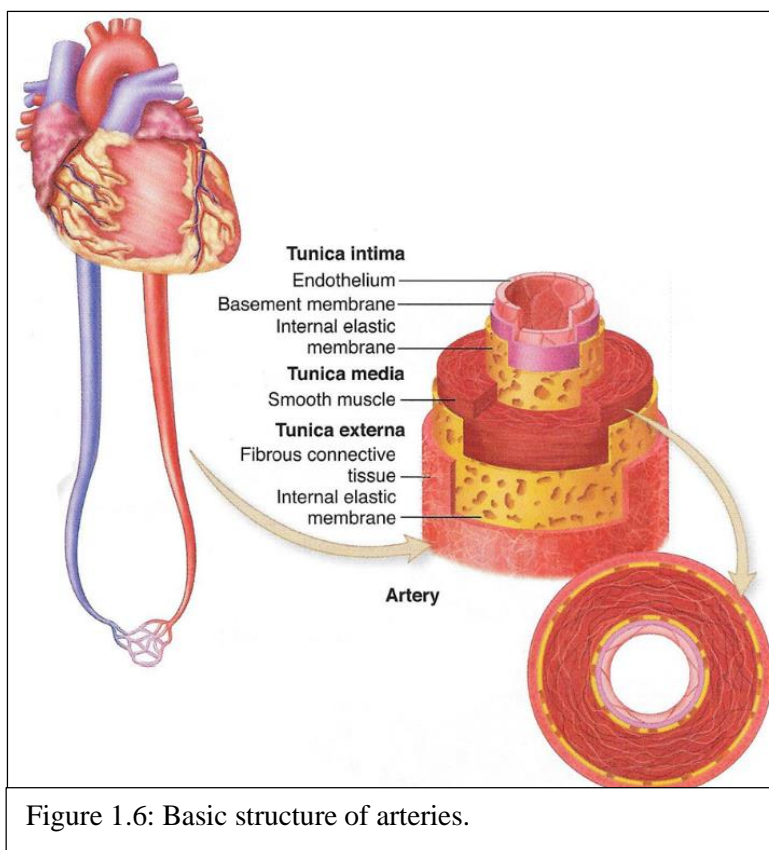


Figure 1.6: Basic structure of arteries.

(Patton, Thibodeau & Douglas: 377-378)

Based on their size and characteristics of their tunica media, arteries are classified into three types. The largest arteries are called the elastic arteries. The medium-sized arteries are called the muscular arteries and the small arteries are called the arterioles (Table 1.1). (Ross & Pawlina, 2006: 372)

Table 1.1: Distinguishing features of arteries.

BLOOD VESSEL	SIZE	TUNICA INTERNA	TUNICA MEDIA	TUNICA EXTERNA	EXAMPLES	FUNCTION
ELASTIC ARTERIES	Largest arteries in the body.	Well-defined internal elastic lamina	Thick and dominated by elastic fibres; well-define external elastic lamina	Thinner than tunica media.	Aorta, Pulmonary trunk, brachiocephalic artery, common carotid artery & common iliac arteries	Conduct blood from heart to muscular arteries.
MUSCULAR ARTERIES	Medium-sized arteries.	Well-defined internal elastic lamina	Thick and dominated by smooth muscle; thin external elastic lamina.	Thicker than tunica media.	Femoral arteries & axillary arteries.	Distribute blood to arterioles.
ARTERIOLES	Microscopic.	Thin with a fenestrated internal elastic lamina that disappears distally	1 or 2 layers of circularly oriented smooth muscle; distal most smooth muscle cells forms a precapillary sphincter.	Loose collagenous connective tissue and sympathetic nerves.		Deliver blood to capillaries and help regulate blood flow from arteries to capillaries.

(Tortora & Derrickson, 2011: 810)

Atherosclerosis is a common disease, which affect elastic and muscular arteries, in which lipid material infiltrates the tunica intima and accumulates in macrophages. This stimulates the growth of fibroblasts and myointimal cells, with collagen deposition to produce a plaque called atheroma, that causes the intima to thicken. (Young, O'Dowd & Woodford. 2014: 148)

The muscle cells in the tunica media can be replaced by non-contractile and non-elastic collagen as a result of severe atheroma. This causes the artery wall to lose elasticity. (Young, O'Dowd & Woodford. 2014: 148)

According to Tortora and Derrickson (2011: 791), cardiovascular disease affects about seven million people annually and is the leading cause of death in both men and women in the developed world. Most cardiovascular disease results from the effects of atherosclerosis. (Mayo Clinic, n.d)

When these atheroma burst, they can trigger a blood clot and this may lead to acute loss of blood supply such as stroke or myocardial infarction. An accumulation of atherosclerotic plaques can also lead to a chronic reduction in blood flow to the myocardium (figure 1.7). (Tortora & Derrickson, 2011:791)

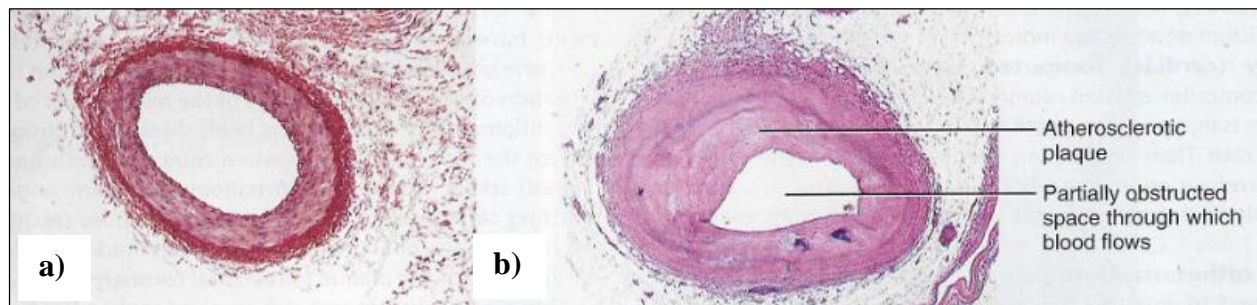


Figure 1.7: Photomicrographs of a transverse section of a healthy artery (a) and a partially obstructed artery (b).

(Tortora & Derrickson, 2011:791)

The myocardium is the thick middle layer of the heart, between the fibrous pericardium and the endocardium. It is composed largely of cardiac muscle, and is the contractile layer of the heart. It comprises the bulk of the heart wall (figure 1.8). A reduction in blood flow to the myocardium can lead to a myocardial infarction (heart attack), and can cause permanent myocardial damage of even death. (Patton, Thibodeau & Douglas: 377-378)

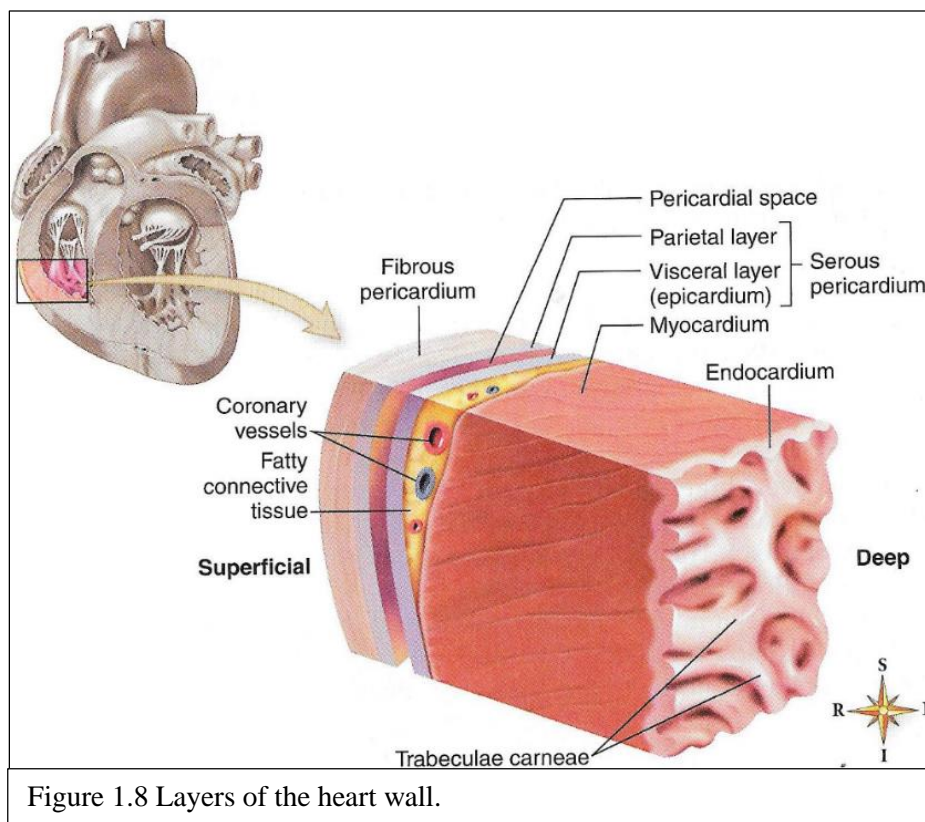


Figure 1.8 Layers of the heart wall.

(Patton, Thibodeau & Douglas: 377)

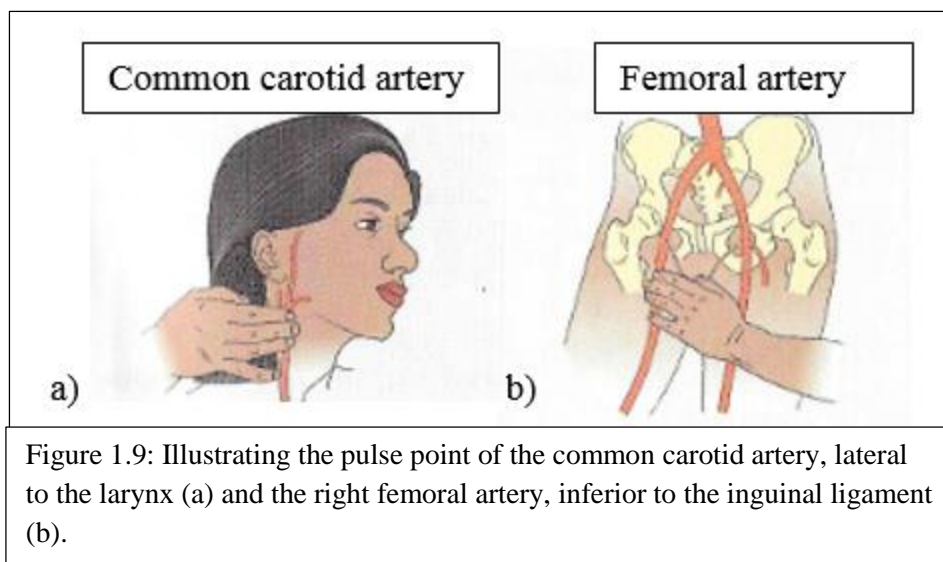
1.1.4 Effect of atherosclerosis on the pulse

After each systole of the left ventricle, the elastic arteries expand and recoil to create a travelling pressure wave. This pressure wave is called the pulse and is the strongest in the arteries closest to the heart. It is possible to evaluate the pulse as it can be felt in some superficial arteries and in some arteries that run over bones. (Tortora and Grabowski, 2003: 713)

Conditions such as atherosclerosis greatly increase the speed of the pulse/pressure wave.

Increased speed of the pulse/pressure wave can be detected with carotid-femoral pulse wave

velocity calculations. The pulse points used for this calculation are the common carotid artery pulse and the right femoral artery pulse (figure 1.9).



(Tortora and Grabowski, 2003: 714)

1.1.5 Basic principles of multidetector-row helical computed tomography (CT)

Currently surgeons rely exclusively on Computer Tomography (CT) imaging and multi-planar reconstruction (MPR) imaging software to do measurements of large vessels, for endo-vascular aortic repair.

Previous research which utilized CT imaging, evaluated the accuracy of a certain measurement software that was created for aortic stent-graph planning (Isokangas, Hietala, Perälä, & Tervonen, 2003). They concluded that “the software enables accurate measurements perpendicular or parallel to the semi-automatically created centerline path.” We are therefore of the opinion that MPR is a reliable technique for determining true vessel lengths radiologically, which will be the ‘gold standard’ used in the current study.

In the current study, three dimensional (3D) volume rendered images were used to perform surface anatomy measurements. To the best of our knowledge, to date there are no studies that were performed to assess the accuracy and reliability of surface anatomy measurement on 3D volume rendered imaging. However Calhoun et al (1999) concluded from their research that

centered on volume rendering, that “volume rendering is a flexible, accurate 3D imaging technique that can help the radiologist more effectively interpret the large volumes of data generated by modern CT scanners. To obtain accurate results, however, the radiologist must understand the effect of parameter selection on the resulting image” Prior to data collection for the current study, the accuracy of the three-dimensional linear measurements was verified using a phantom. The same phantom that is used routinely to perform daily calibrations.

The linear distance measured on the 3D volume rendered images were identical to distances measured using a sliding caliper. Levi-Marpillat et al (2013) concluded from their research that it is crucial to assess distances using a sliding caliper, instead of a flexible tape as one can easily overestimate the distance with flexible tape. They added that the overestimation depends on the body mass index (BMI) and not on gender.

Multi-planar reformats and three-dimensional volume rendering would not have been possible if it wasn't for the rapid development of multidetector-row helical CT.

Just as in other x-ray examinations, a well-collimated beam is directed onto the patient, and the attenuated image-forming radiation is detected by an image receptor. The image receptor in multidetector-row helical CT is not film or an image-intensifier, but a solid state detector.

Computer software is used to analyze the signal from the detector and to reconstruct an image.

Computer monitors are then used to display the images. (Bushong, 2004: 423)

In multidetector-row helical CT, the x-ray tube continuously rotates around the patient, while the couch that the patient lies on moves through the rotating x-ray beam (figure 1.10). Previously this was known as spiral CT, but this was misnamed (figure 1.11). Data collection happens continuously, because the x-ray tube is energized continuously. With the first and second generation CT scanners this was not possible, because the x-ray tube was connected to electrical cables that limited the rotation to 180 degrees, and after every gantry rotation needed to be rewound to its starting position. The current generation of CT scanner contains electromagnetic devices called slip-rings. These electromagnetic devices eliminate the use of electrical cables as it conducts electricity and electrical signals through brushes and rings (figure 1.12). The electricity and electrical signals are transmitted from a rotating surface onto a fixed surface.

There are three slip-rings within a multidetector-row helical CT scanner: one that provides a high

voltage power to both the x-ray tube and the high voltage generator; a second that provides low voltage power to control systems on the gantry; and a third that transfers digital data from the rotating detector array. (Bushong, 2004: 446) These slip-rings not only eliminate entanglement of the cables, but it also allows the x-ray tube and detector array to rotate at high speeds of up to 0.5 second per rotation without any gantry vibration. (El-Khoury, et al, 2004: 2)

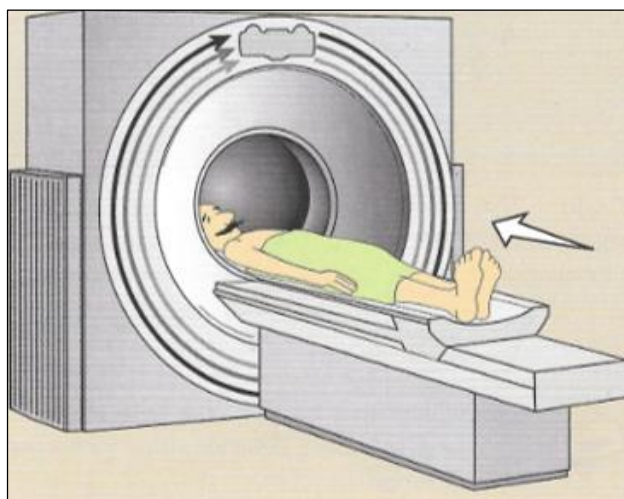


Figure 1.10: Illustrating the x-ray tube movement and patient/couch movement.

(Bushong, 2013: 442)

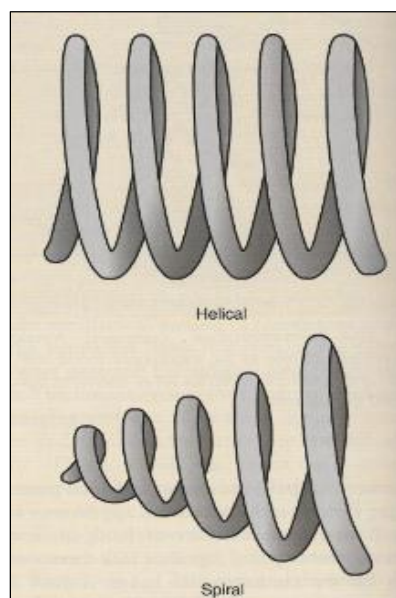


Figure 1.11: Illustration of the difference between spiral and helical

(Bushong, 2013: 442)

It is not only electrical cables that can hamper continuous scanning. During an examination the x-ray tube generates a lot of heat and that is why an x-ray tube with a large heat tolerance and high cooling rate is needed for multidetector-row helical CT scanners as many examinations can last for more than one minute. (Bushong, 2013: 446)

Data collected during a CT examination, can be used to reconstruct an image at any z-axis position. This is made possible by a mathematical process called interpolation. According to Prokop and Galanski (2003), the table feed is not related to the position of where the images are reconstructed.

Interpolation is to estimate a value between two known values, as graphically shown in figure 1.13. The computer program used to perform data interpolation is called an interpolation algorithm. When performing linear interpolation of values that are separated by 360 degrees, prominent blurring occurs when these images are formatted into sagittal and coronal views. One hundred-and-eighty (180) degree linear interpolation was the solution to the blurring problem (Bushong, 2013: 443). According to Bushong (2001) the reason for it to be called linear interpolation, is because “it assumed a straight-line relationship between the two known data points.”

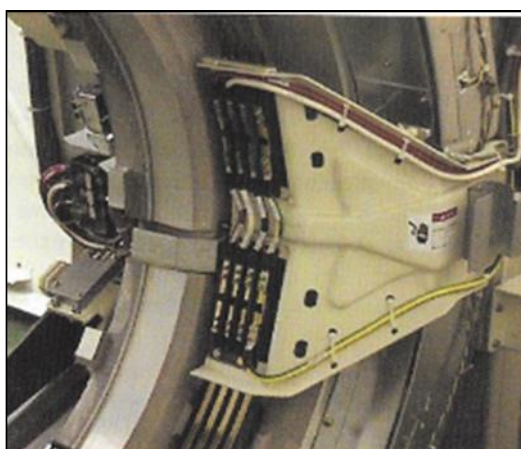


Figure 1.12: Image of slip-rings inside the gantry.

(Bushong, 2013: 449)

This 180 degree linear interpolation also allows for the helical pitch ratio to be more than one. According to Prokop and Galanski (2003), this is the ratio of table movement per gantry rotation, in millimeters, to the x-ray beam width, also in millimeters. This means less radiation to the patient, and also allows for larger volumes of tissue to be scanned in a single breath-hold. The latter is very important when doing CT angiography (CTA), to eliminate motion artifacts.

As mentioned previously, the image receptors in multidetector-row helical CT are called detectors. A detector that consists of a scintillating crystal and a photodiode combination is called a solid-state detector (figure 1.14), and a detector that consists of gas-containing chambers, is called a gas ionizing detector. The latter is considered old technology and is not used in multidetector-row helical CT. Solid state detector has a large dynamic range, as well as a high quantum

efficiency. A single linear detector array contains thousands of individual detectors, as shown in figure 1.15. A multidetector-row helical CT scanner contains multiple linear detector arrays. There are however different types of detector combinations for signal summation. Each individual detector is connected to a data acquisition system or a DAS. This DAS is a computer controlled electronic amplifier and switching device, that selects the detector combinations, according to width. The width refers to the detector beam collimation width. (Bushong, 2004:451)

The detector combination, where all the detector rows are of identical width, is called a matrix detector. The detector where the detector rows grow in width from the center is called an adaptive array detector. A hybrid detector, has smaller detector rows in the center and larger detector rows toward the border and are used in all sixteen-slice CT scanners. (Prokop & Galanski, 2003: 21-23)

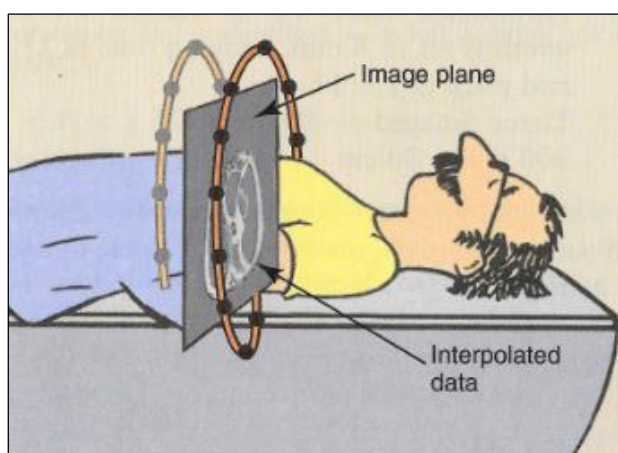


Figure 1.13: Illustrating interpolated data between known data points.

(Bushong, 2013: 443)

(Cunningham & Judy, 2000: 7)

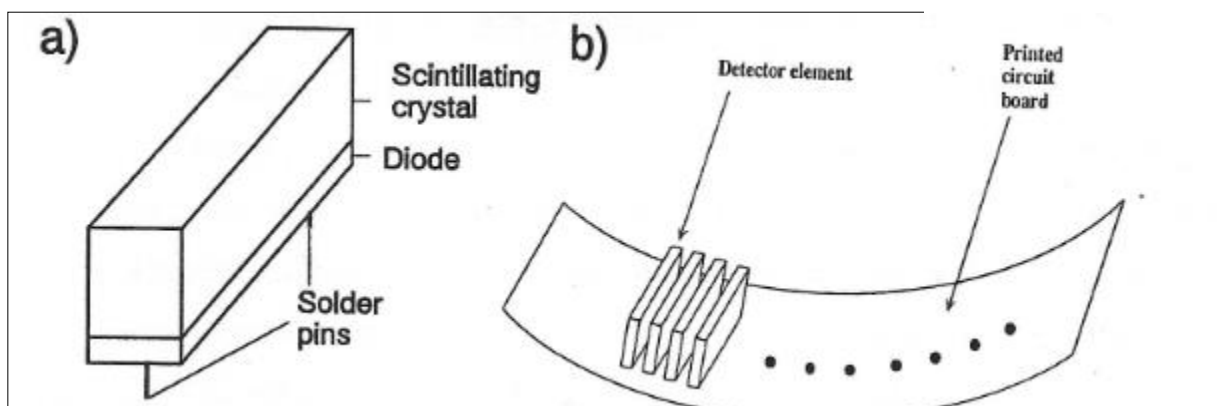
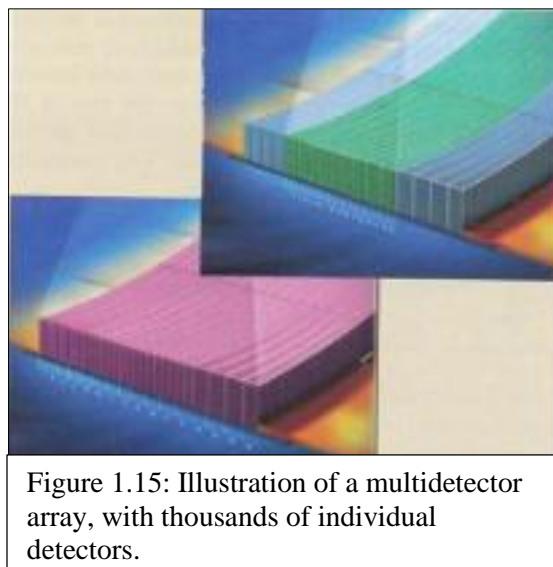


Figure 1.14: Illustration of a solid state detector, with its scintillating material and photodiode (a). Multiple individual detectors are placed side by side to form a detector array (b).



(Bushong, 2013: 447)

1.1.5.1 Multi-planar Reformation

Multidetector-row helical CT performs exceptionally well when it comes to three dimensional multi-planar reformations. A three-dimensional image is rendered from stacking axial images. The 3D MPR algorithms used most frequently are maximum intensity projection (MIP), shaded surface display (SSD) and shaded volume display (SVD). (Bushong, 2013: 451)

When using the MIP algorithms for CT angiograms, it will result in a high contrast three-dimensional image of contrast-filled vessels as shown in figure 1.16a. This is considered the simplest form of 3D imaging in multidetector-row helical CT, as it only uses 10% of the 3D data points. There is however as downside to this images reconstruction method as it only displays superimposed vessel (lacks vessel depth). (Bushong, 2013: 451)

Shaded surface display is regularly used for virtual colonoscopy. This computer aided technique has been borrowed from computer aided design and manufacturing applications. A shaded surface display is used to display organ surface as shown in figure 1.16b. (Bushong, 2013: 452)

The third 3D MPR algorithm that is used frequently is the surface volume display. The images one obtains from a surface volume display appear very three-dimensional. A surface volume image such as the one in figure 1.16c, is called a 3D volume rendered image. (Bushong, 2013: 452)

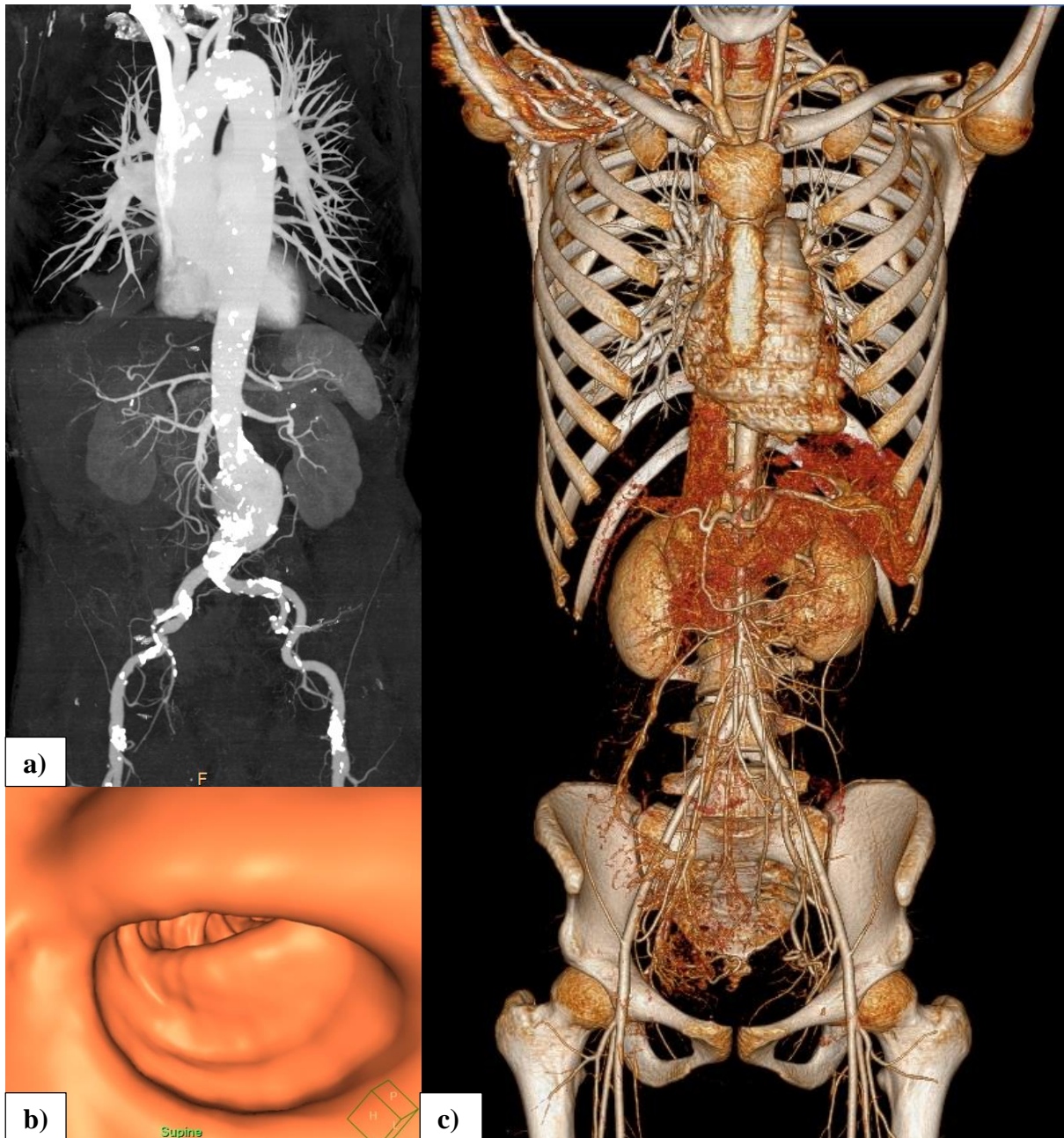


Figure 1.16: An anterior view of a MIP (a), SSD of the colon (b) and anterior view of a volume rendering display (c).

1.1.5.2 Principles of CT Angiography (CTA)

To obtain an image that displays the major arteries, like the one in figure 1.16a and 1.16c, is not possible without administering vascular contrast.

According to Prokop and Galanski (2003:11) a high vascular contrast is the foundation for CT angiography (CTA) to capture the arterial enhancement and generate angiogram-like vascular images. This technique is called Bolus tracking.

With CT angiography a small catheter is placed in a vein of the arm, to inject an iodine-rich contrast. While the contrast flows through the blood vessels to the various organs of the body, the CT scanner acquires imaging data (bolus tracking). When scanning is done the imaging data is processed by multi-planar reconstruction imaging software, for the images to be reviewed in different planes and projections demonstrating anatomy and pathology. (Radiology info, 2015)

Some of the advantages of CT angiography include: demonstrating anatomical detail of blood vessels more accurately than other modalities (MRI and Ultrasound). It is less invasive than conventional angiography where placement of a femoral or brachial catheter is required. It is cheaper than conventional angiography and is less time consuming. It utilizes intravenous injection and therefore reduces the risk of thrombo-embolic complications. Only a single bolus injection is needed to allow for an entire volume of data to be acquired. (Parker, 2003)

One disadvantage of CT angiography is that it can only serve as diagnostic test, whereas conventional angiography serves as both diagnostic and therapeutic intervention. Secondly, CT angiography may not be performed on patients with kidney failure (the use of iodinated contrast medium may put further strain on the kidneys). Thirdly, there is a risk of the patient being allergic to the iodine contrast media. (Parker, 2003)

1.1.5.3 Ionizing radiation

One major downside of CT is the exposure to ionizing radiation. Ionizing radiation such as x-rays can be harmful to humans. Intense x-rays can cause skin burns, leukemia, cancer and other harmful effects, although the degree of these effects is not known for certain.

Some of the early effects of radiation on humans are local tissue damage (skin, gonads and extremities) and acute radiation syndromes, such as hematologic syndrome, gastrointestinal syndrome and central nervous system syndrome.

The late effects of radiation will include leukaemia, malignant disease (lung cancer, bone cancer, thyroid cancer and breast cancer), local tissue damage (skin, gonads and eyes), life span shortening and genetic damage. (Bushong, 2004: 484)

Because there are many benefits to diagnostic application of x-ray, it is still used in hospitals, as the benefits outweigh the risks. The radiology personnel are therefore trained to keep the radiation exposure to a patient as low as reasonably achievable (ALARA), and still be able to deliver high-quality diagnostic images/CT images.

Radiology Info.org (2015) stated that “every effort will be made to reduce radiation while performing CT angiography, including tailoring the scan parameters specifically to your body type and weight. The scanning area will also be limited to the area of interest to avoid unnecessary radiation to other body parts.”

CT remains the examination of choice for vascular studies, even though magnetic resonance imaging (MRI) allows the characterization of cardiovascular structure, function, and blood flow without exposing the patient to ionizing radiation (Hong, 2015). This may be due to the longer examination times, anaesthetic is needed for children, and MRI exams are more expensive.

Due to the exposure to ionizing radiation, it would be impractical to combine PWV calculation with a CT angiogram, to obtain the more accurate distance travelled by the aorto-femoral pressure wave.

CHAPTER 2

2.1 MATERIAL AND METHODS

Ethical approval was sought from Health Research Ethics Committee of Stellenbosch University. A retrospective collection of CT scans between January 2010 to May 2018 were used. Since the images were part of an archive database, there was no direct interaction with patients and a waiver of individual informed consent was requested from the ethics committee. Personal information was kept strictly confidential and identifying information was not captured.

The main aim of this study was to investigate the most accurate estimation of distance travelled by the aorto-femoral pressure wave, by comparing distances obtained using various surface anatomy landmarks to intraluminal vessel distances in children of varying ages, in order to standardize PWV calculation in children and allow for inter-study comparisons.

Vessel lengths in children (aged 0-18 years) were measured with multi-planar reformation (MPR) imaging software called IntelliSpace Portal (version 4). These measurements were then compared with surface anatomy measurements also obtained using the same MPR imaging software. The comparisons between vessel lengths and surface anatomy distances were performed in segments, since there were no whole body CT scans available on the Picture Archiving and Communication System (PACS) at the research site.

CT scans of patients with congenital abnormalities of skeleton, as well as CT scans of patients with any disease likely to distort the gross anatomy of the large vessels were excluded from this study.

2.1.1.1 Background: Estimation of the true distance travelled

The Vicorder device measures the time delay between the pulse wave arriving at the carotid cuff and the pulse wave arriving at the femoral cuff. During the time that the pulse wave travels from the heart to the carotid (fig 2.1 green arrows), that same pulse wave (on its way to the femoral artery) will have reached somewhere in the thoracic aorta (fig 2.1 purple arrows). Thus the true distance travelled is the intraluminal distance between this unknown point in the thoracic aorta, and the femoral artery (fig 2.1 blue arrows). However, since that indeterminate point in the

thoracic aorta cannot be detected, the distance between it and the origin of the brachiocephalic artery (which is where the pulse wave separates, fig 2.1 green and purple arrows) is assumed to be equal to the distance from the brachiocephalic origin to the carotid cuff. The true distance travelled is then estimated to be the distance from the brachiocephalic origin to the carotid cuff, subtracted from the distance between the brachiocephalic origin and the femoral cuff.

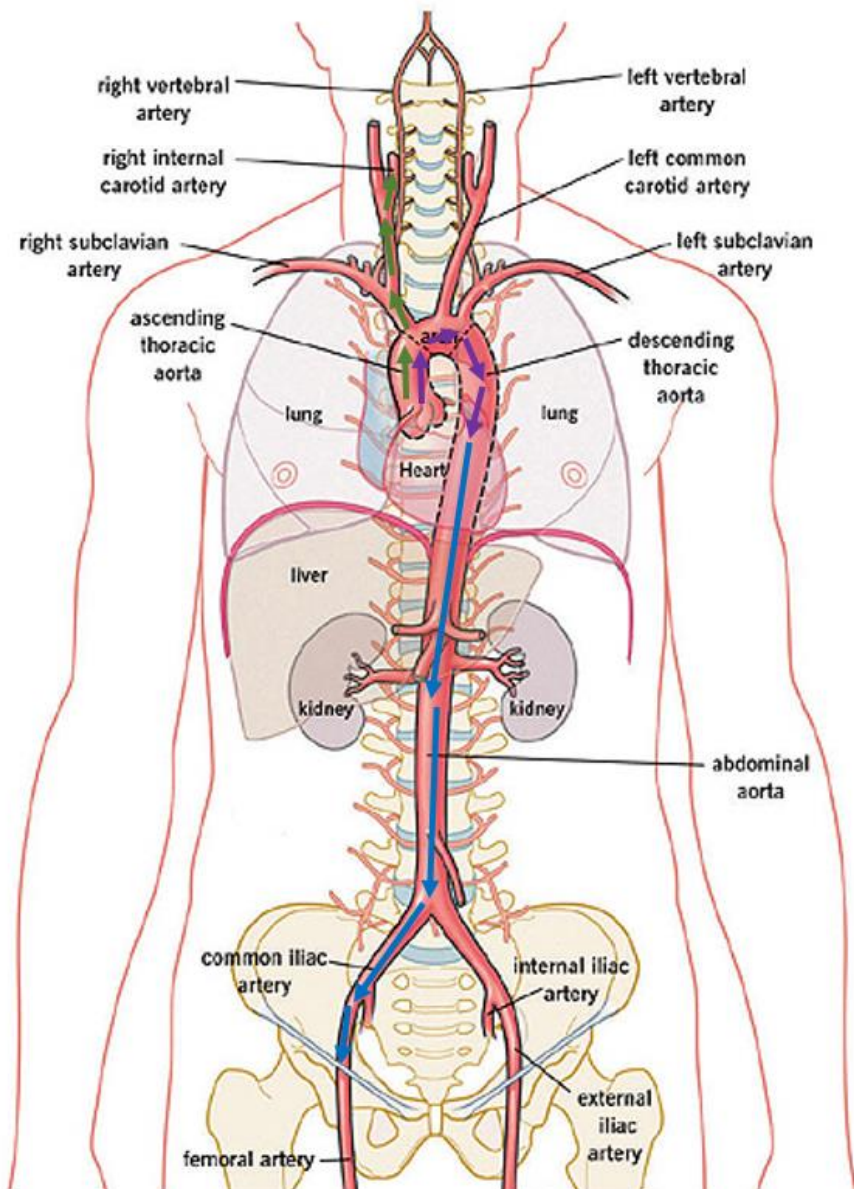


Figure 2.1: The true intraluminal distance travelled by the pressure wave for carotid-femoral PWV calculations, are demonstrated by the blue arrows.

2.1.1.2 Background: surface anatomy landmarks for pulse wave velocity

In the clinical setting, the operator uses surface anatomy landmarks together with a tape measure/sliding caliper to estimate the true distance travelled by the aorto-femoral pressure wave. Lumley (2002: 4) stated that “all doctors and other clinical professionals need to know the range of normal anatomy, to be able to identify the position of the deeply related structures”

The suprasternal notch, xiphisternum, umbilicus, are the surface anatomy landmarks mostly commonly used to estimate vessel length for the purpose of PWV calculations, together with the recording site in the neck and the recording site on the femur.

For this study we used the angle of the mandible as a surface anatomy landmark to estimate the position of the external carotid artery in the neck and the right mid-inguinal crease to estimate the position of the right femoral artery.

Angle of mandible: The lower jawbone is called the mandible, it is the largest and strongest facial bone and articulates with the temporal bones. (Patton, Thibodeau & Douglas:159).

According to Backhouse and Hutchings (1998: 33), when the common carotid artery divides into the internal and external carotid arteries, the external carotid artery first runs anteriomedial to the internal carotid (figure 2.2a), and later more lateral behind the neck of the mandible (figure 2.2b).

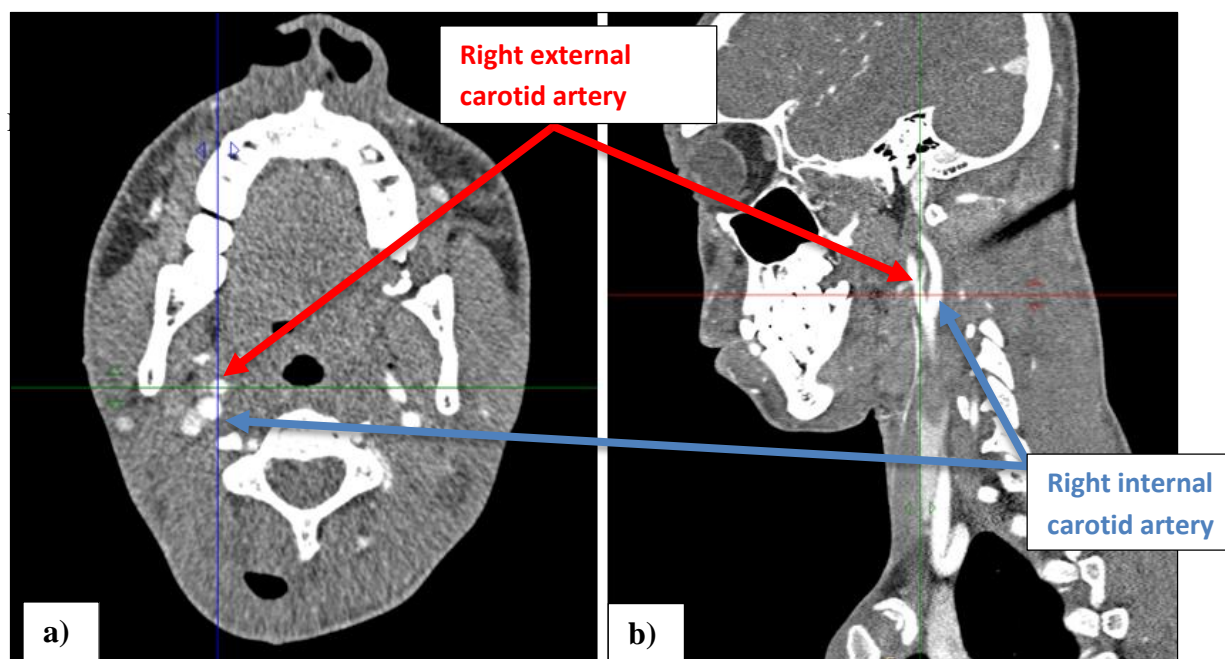


Figure 2.2: Axial (a) and sagittal (b) view of the right internal and external carotid arteries.

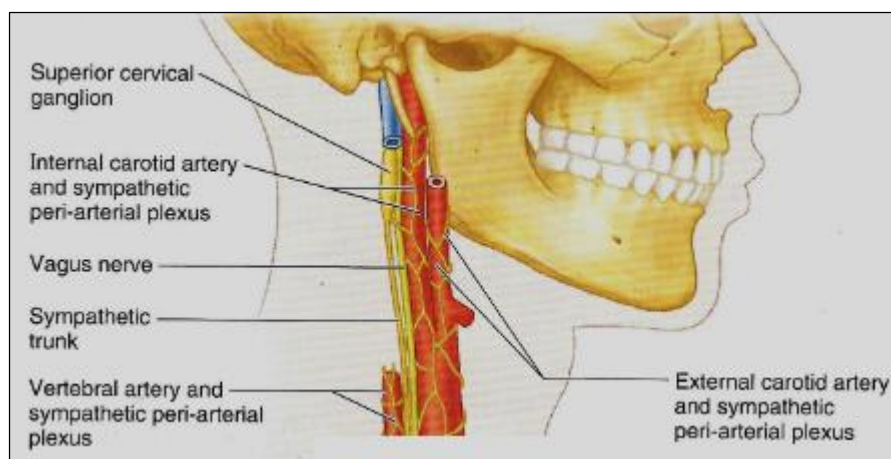


Figure 2.3: Lateral view of the external and internal carotid arteries.

(Moore, Dally & Agur, 2014: 1016)

The suprasternal notch and the xiphisternum: The sternum is the flat bone that consists of three parts namely the manubrium, the body and the xiphoid process/xiphisternum. These segments typically fuse during the mid-twenties. The sternum is located in the center of the anterior thoracic wall. The superior aspect of the manubrium is called the suprasternal notch and the small inferior part of the sternum is called the xiphoid process or the xiphisternum (figure 2.4). (Tortora & Derrickson, 2011: 245)

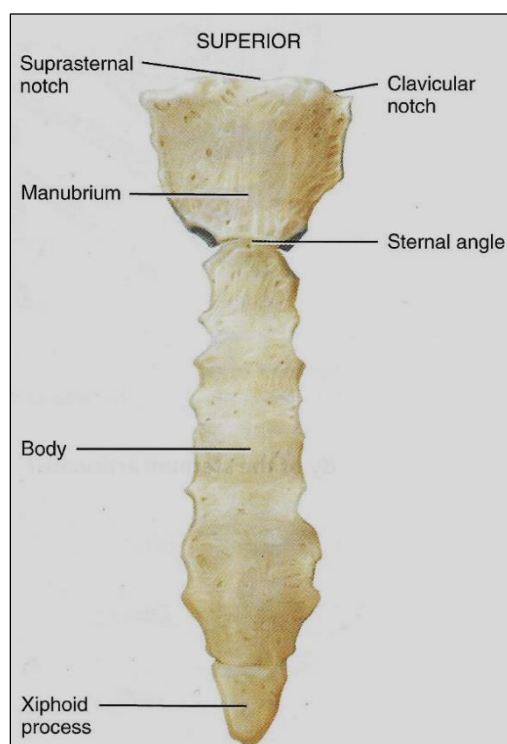


Figure 2.4: Anterior view of the sternum and its three parts.

(Tortora & Derrickson, 2011: 245)

The umbilicus: The umbilical cord is the connection between the embryo/fetus and the placenta. It consists of two umbilical arteries, an umbilical vein, mucous connective tissue and a layer of amnion (figure 2.5). After a female has given birth to an infant, the umbilical cord is tied off. Two weeks after birth, the small portion of the umbilical cord that remained, falls off. The area where the umbilical cord was attached becomes covered by skin and scar tissue forms. The scar is called the umbilicus. When standing in the anatomical position, the aortic bifurcation is believed to be on the same axial/transverse level of the umbilicus (figure 2.6). (Tortora & Derrickson, 2011: 1194)

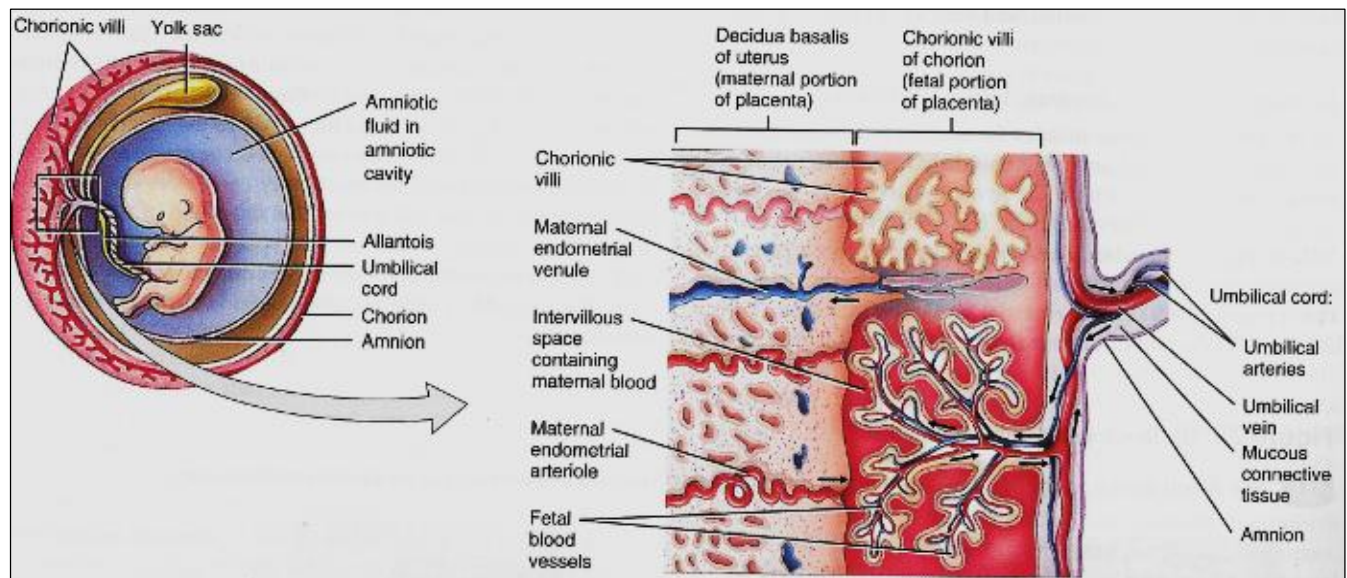
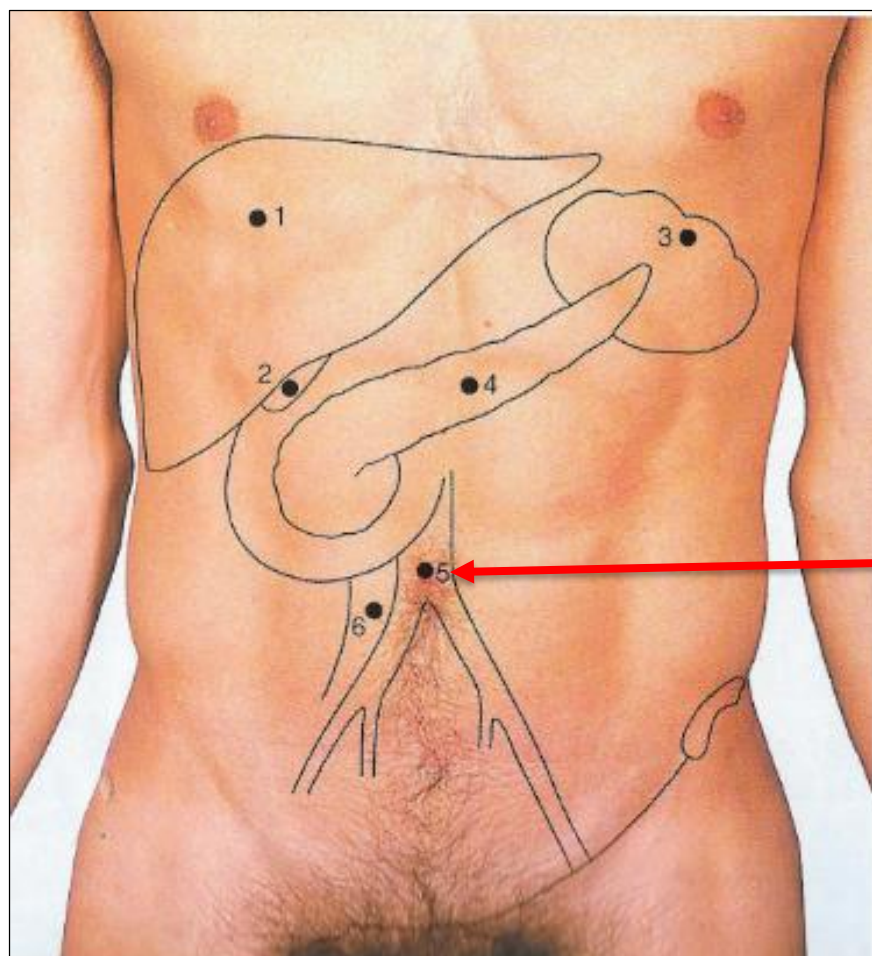


Figure 2.5: Details of the umbilical cord.

(Tortora & Derrickson, 2011: 1194)



Abdominal aorta divides at the level of the umbilicus

(Lumley, 2002:44)

Figure 2.6: Surface marking of the aortic bifurcation (5).

The pelvic girdle is used to estimate the position of the femoral artery. It consists of two pelvic/hip bones, the sacrum and the pubic symphysis (figure 2.7). During infancy the pelvic bone consist of three bones, they are the ilium, ischium and pubis. These bones are separated by cartilage and fuse in the mid-twenties. That is why anatomists commonly describe each pelvic bone as three separate bones. Each of the three components of the pelvic bones has many surface features, but for this research project only one of the ilium and one of the ischium is important.

The ilium is the largest of the three bone and the iliac is the superior border of the ilium. The ilium ends anteriorly in a blunt “anterior superior iliac spine” (figure 2.8). (Tortora & Derrickson, 2011: 267)

The anterior and inferior part of the pelvic bone is called the pubis, consist of a superior ramus, a body and an inferior ramus. The superior border of the body is called the pubic crest, and the projection at the lateral end is called the pubic tubercle (figure 2.8). (Tortora & Derrickson, 2011: 267)

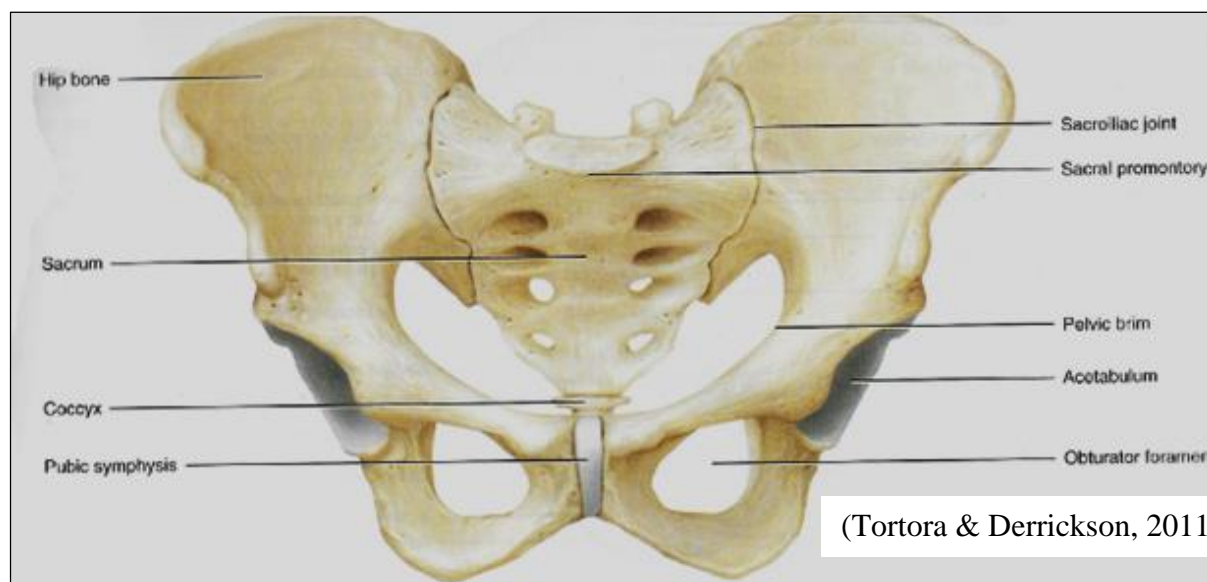
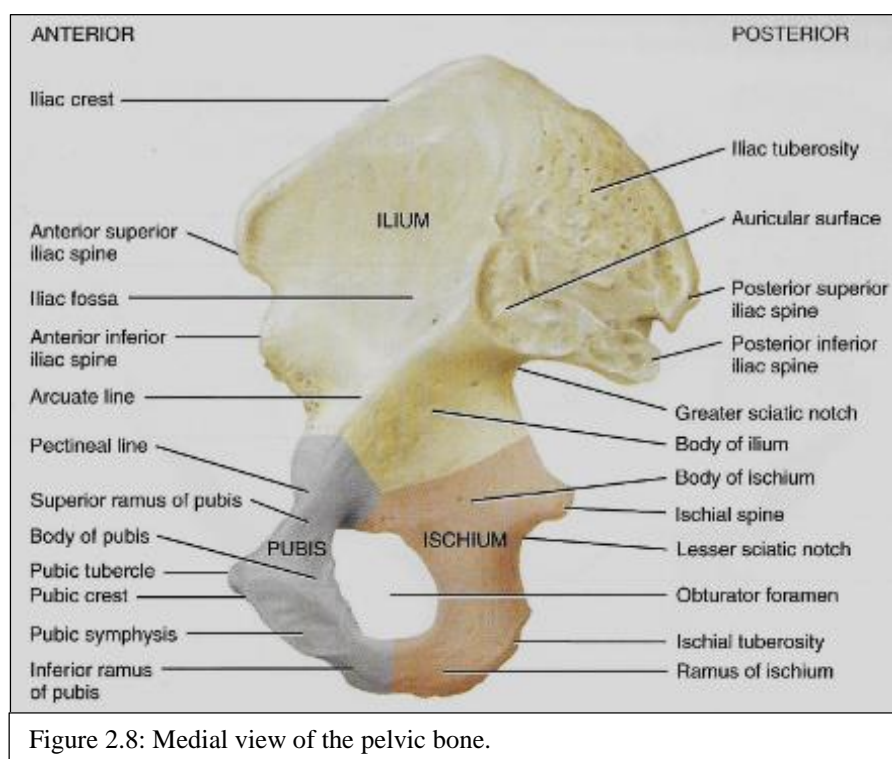


Figure 2.7: Anterosuperior view of the pelvis.



(Tortora & Derrickson, 2011: 268)

The surface marking for the start of the right femoral artery is midway between the anterior superior iliac spine and the symphysis pubis/pubis tubercle. This surface marking is also known as mid-inguinal crease (figure 2.9). (Lumley, 2002:45)

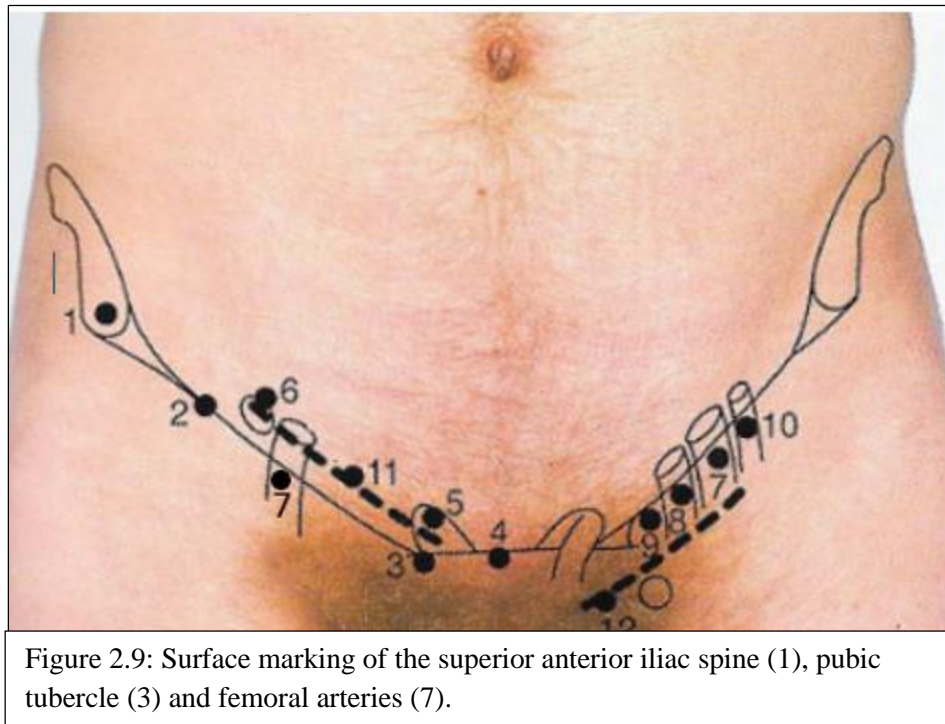


Figure 2.9: Surface marking of the superior anterior iliac spine (1), pubic tubercle (3) and femoral arteries (7).

(Lumley, 2002:45)

2.1.2 Research design

CT scans from individuals aged less than 18 years were used. The scans were stored on the picture archiving and communication system (PACS), of an academic hospital in Cape Town, South Africa. Since there were no CT scans that included both the angle of the mandible and the pelvis, the comparisons of surface anatomy distances to vessel lengths were performed in segments as described below.

2.1.2.1 Six surface anatomy distance points

Table 2.1 refers to each of six surface anatomy distance points, described most commonly in existing literature for PWV calculations. These surface anatomy distances were collected using the Advance Vascular Analyses (AVA) application within IntelliSpace Portal (Philips, 2008: 12). The vessel measurements and the surface anatomy measurements in this study were entered into a Microsoft Office Excel 2010 spreadsheet and then transferred into Statistica 13.3 for statistical analysis.

Table 2.1: Six surface anatomy distances used for PWV calculations, with associated abbreviations.

Six surface anatomy points	Abbreviations
<u>A</u> ngle of the mandible to <u>S</u> uprasternal notch	AS
<u>S</u> uprasternal notch to <u>X</u> iphisternum	SX
<u>S</u> uprasternal notch to Midpoint of the right <u>I</u> nguinal crease	SI
<u>X</u> iphisternum to <u>U</u> mbilicus	XU
<u>X</u> iphisternum to Midpoint of the right <u>I</u> nguinal crease	XI
<u>U</u> mbilicus to Midpoint of the right <u>I</u> nguinal crease	UI

2.1.2.2 Six large vessel distance points

Table 2.2 refers to each of the six vessel distances, described most commonly in existing literature for PWV calculations. These vessel distances were collected using the Advance Vascular Analyses (AVA) application within IntelliSpace Portal (Philips, 2008: 12).

Table 2.2: Six large vessel distances used for PWV calculation, with associated abbreviations.

Six large vessel point	Abbreviations
Origin of brachiocephalic <u>T</u> runk to Origin of right <u>C</u> ommon carotid	TC
Origin of right <u>C</u> ommon carotid to Carotid <u>B</u> ifurcation	CB
Carotid <u>B</u> ifurcation to <u>E</u> xternal carotid at angle of mandible	BE
Origin of brachiocephalic <u>T</u> runk to Aorta at the <u>X</u> iphisternum	TX
Aorta at the <u>X</u> iphisternum to <u>A</u> ortic bifurcation	XA
<u>A</u> ortic bifurcation to Right <u>F</u> emoral artery at inguinal ligament	AF

2.1.2.3 Data sets and respective comparisons

On sagittal, coronal, axial and 3D volume rendered images, the operator measured the components of at least one of the sets of distances presented in Table 2.3 (i.e. scan sequences did not need to encompass the entire length to be eligible):

Table 2.3: Data sets and respective comparisons.

	Surface anatomy measurements	Large vessel measurements
Set 1	AS	TC+CB+BE
Set 2	SX	TX
Set 3	XI	XA+AF
Set 4	XU+UI	XA+AF
Set 5	SI	TX+XA+AF
Set 6	SX + XI	TX+XA+AF
Set 7	SX + XU +UI	TX+XA+AF

Graphically, the data sets and respective comparisons can be represented as follows:

Large vessel measurement	Corresponding surface anatomy measurements		
TC	AS		
CB			
BE			
TX	SI	SX	
XA		XI	XU
AF			UI

Each of the surface anatomy distance or combination of surface anatomy distances were compared to their respective large vessel distance.

AS was compared	to	(TC + CB + BE);
SX was compared	to	TX;
XI was compared	to	(XA + AF);
(XU + UI) was compared	to	(XA + AF);
SI was compared	to	(TX + XA + AF);
(SX + XI) was compared	to	(TX + XA + AF);
(SX + XU + UI) was compared	to	(TX + XA + AF).

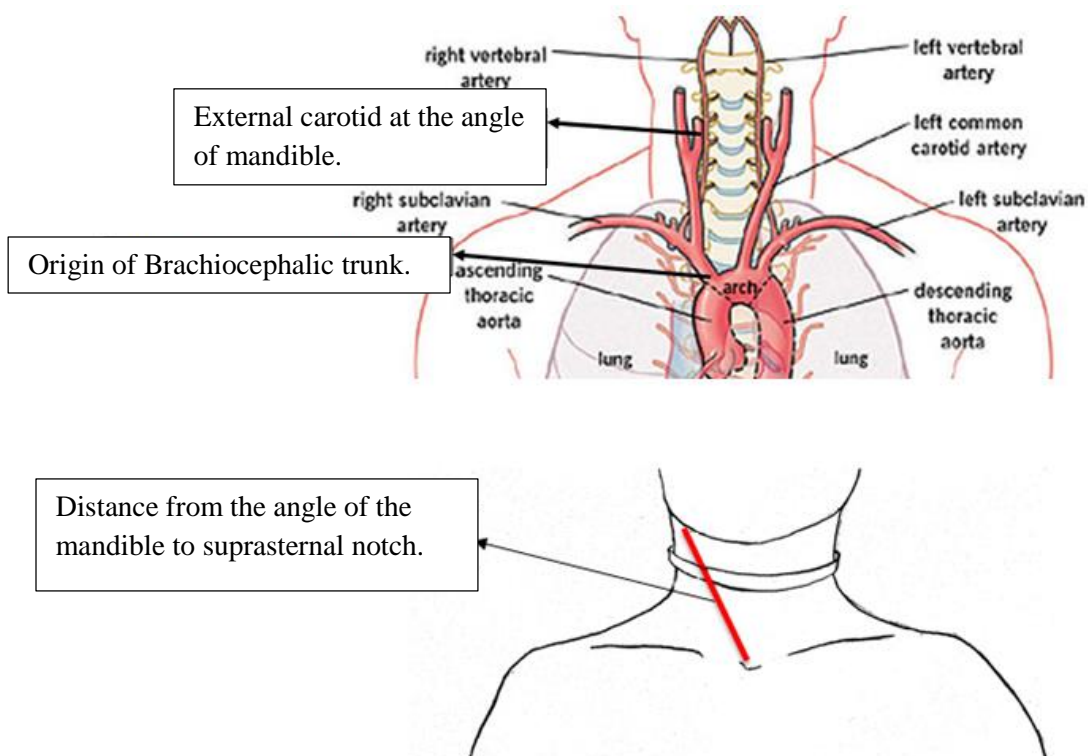


Figure 2.10: Illustration of comparison, TC+CD+BE (origin of the brachiocephalic trunk to the external carotid at the angle of the mandible on the right) to AS (suprasternal notch to the angle of the mandible)

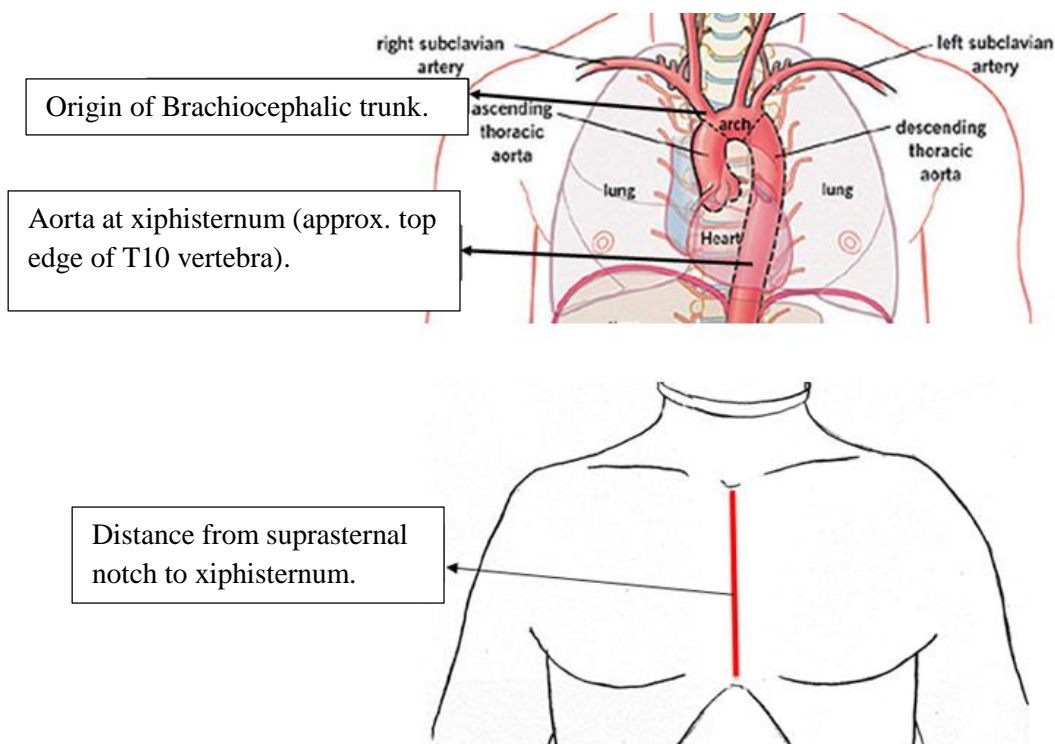


Figure 2.11: Illustration of comparison, TX (origin of the brachiocephalic trunk to the aorta at the xiphisternum) to SX (suprasternal notch to the xiphisternum).

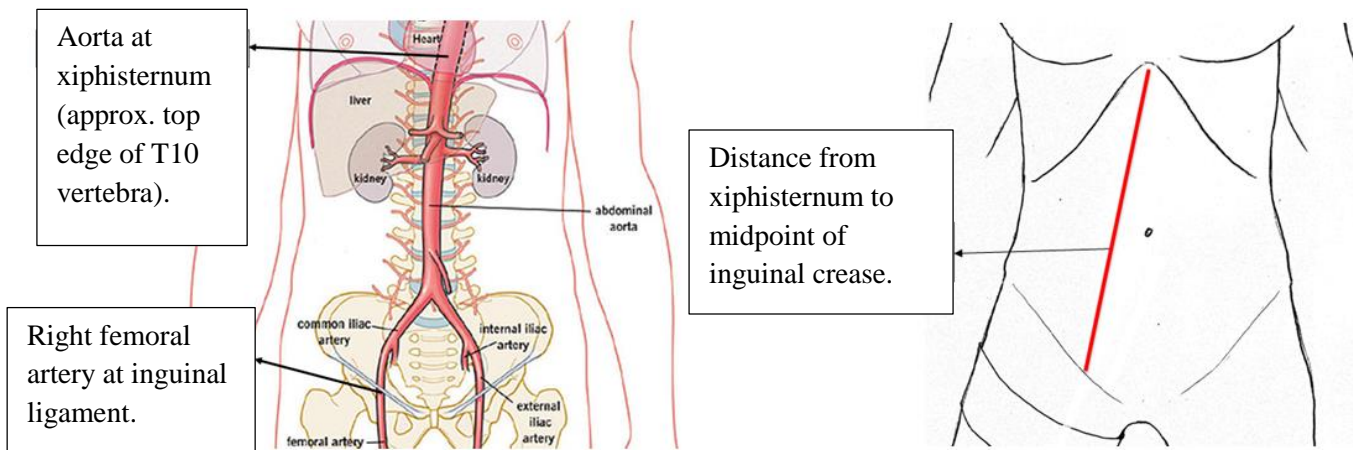


Figure 2.12: Illustration of comparison, XA+AF (aorta at the xiphisternum to the right femoral artery at the inguinal ligament) to XI (xiphisternum to the midpoint of the right inguinal crease).

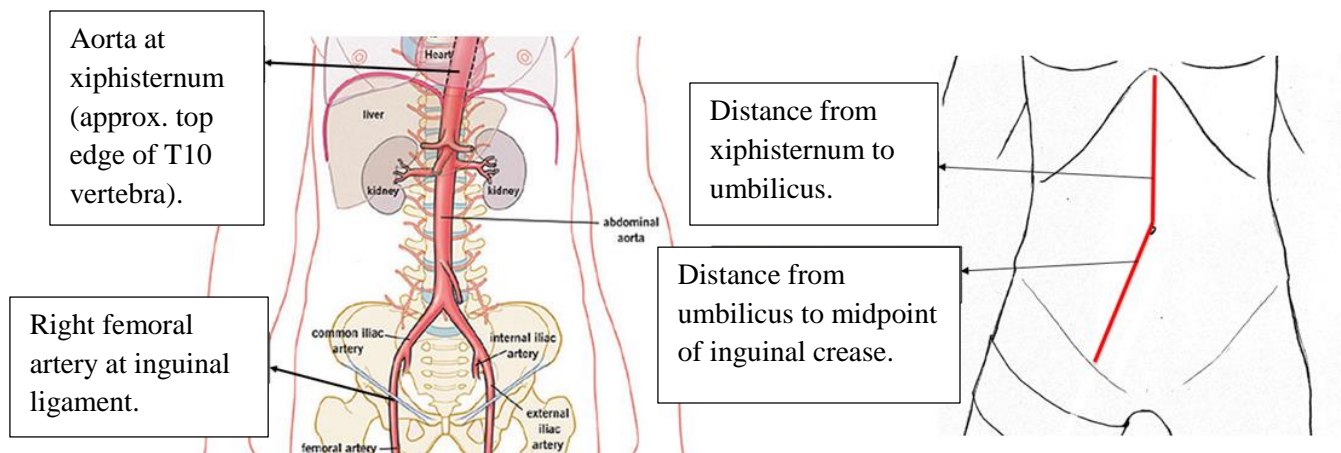


Figure 2.13: Illustration of comparison, XA+AF (aorta at the xiphisternum to the right femoral artery at the inguinal ligament) to XU+UI (xiphisternum to the umbilicus, plus umbilicus to the midpoint of the right inguinal crease)

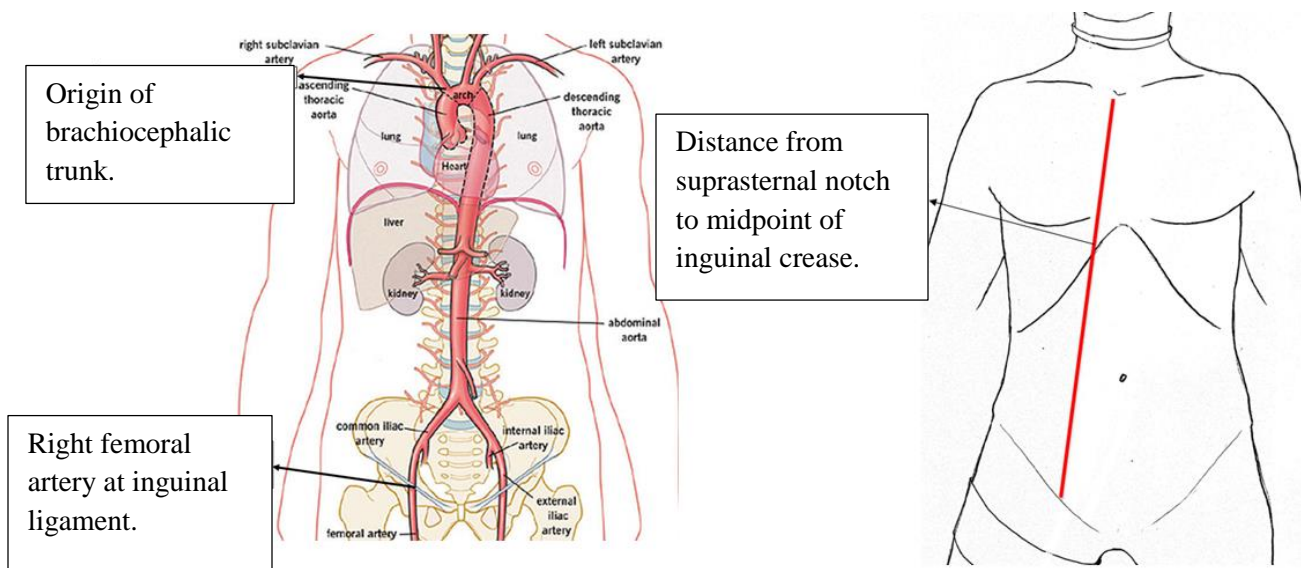


Figure 2.14: Illustration of comparison, TX+XA+AF (origin of the brachiocephalic trunk to the right femoral artery at the inguinal ligament) to SI (suprasternal notch to the midpoint of the right inguinal crease)

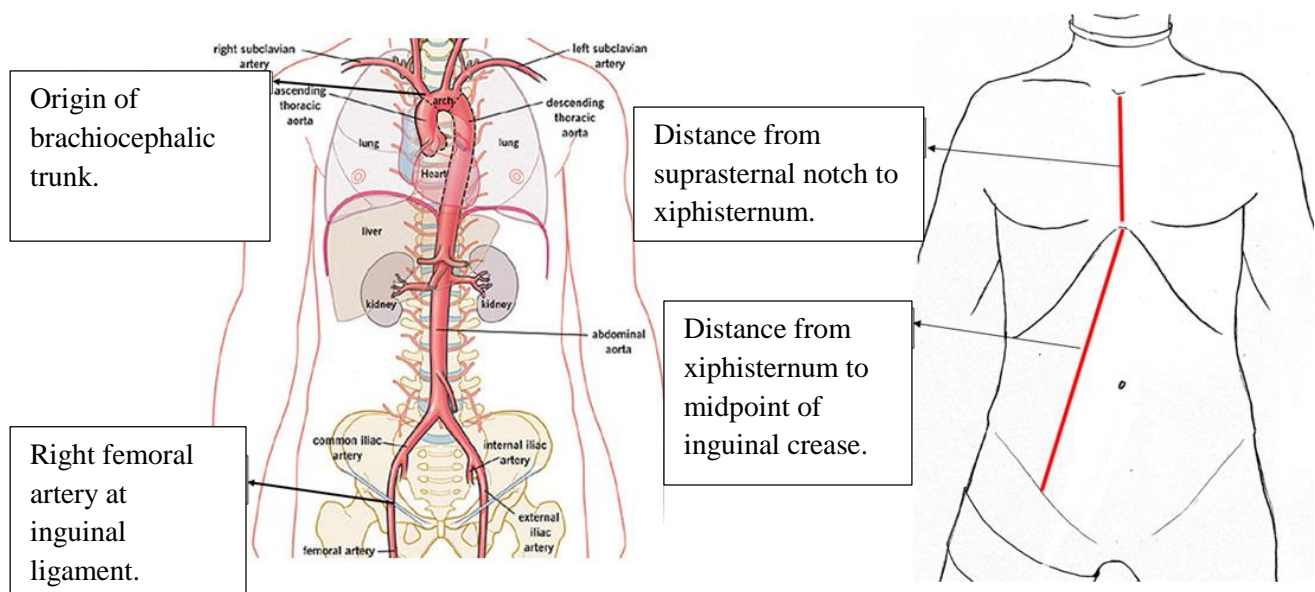


Figure 2.15: Illustration of comparison, TX+XA+AF (origin of the brachiocephalic trunk to the right femoral artery at the inguinal ligament) to SX+XI (suprasternal notch to the xiphisternum, plus xiphisternum to the midpoint of the right inguinal crease)

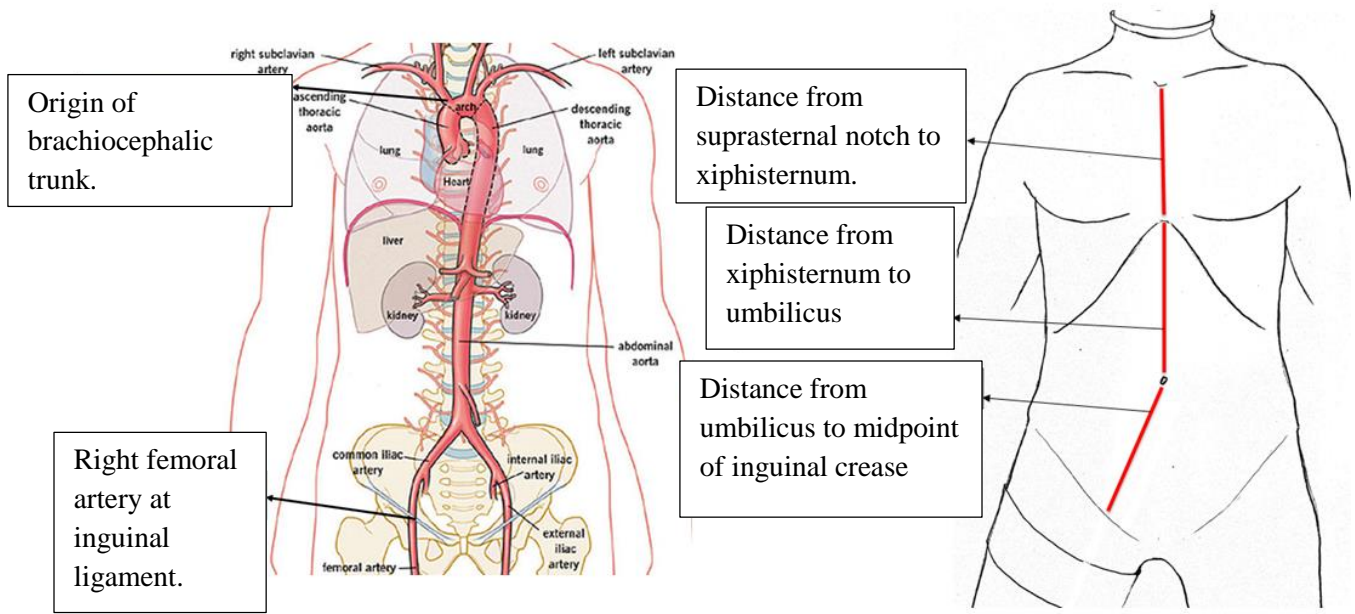


Figure 2.16: Illustration of comparison, TX+XA+AF (origin of the brachiocephalic trunk to the right femoral artery at the inguinal ligament) to SX+XU+UI (suprasternal notch to the xiphisternum, plus xiphisternum to the umbilicus, plus umbilicus to the midpoint of the right inguinal crease).

2.1.3 Methods of data collection

DICOM images were transferred from the Picture Archiving and Communication System to the IntelliSpacePortal server/program. The images were opened on a diagnostic reporting workstation that had IntelliSpacePortal installed. Semi-automated centerline paths of major vessels were created with the Advanced Vascular Analysis (AVA) application within IntelliSpacePortal, by placing serial markers along the vessel using the axial, sagittal, coronal, and 3D volume rendered images. The “Vessel Path” (manual and automatic) buttons became active after at least four markers were placed. By selecting the “Vessel Path” button after all markers were placed, the system calculated and displayed a new centerline path.

The vessel was named by clicking on its name in the “Vessel Name Selection list” or by typing a new name. Tools (Edit and Extend) in the “Vessel Extraction” tab, allowed the researcher to edit/correct centerlines (in cases where the centerlines did not pass through the center of the lumen) and to extend them, if the vessel was not automatically identified.

Once the vessel centerline was extracted, the “Measurements” tab of AVA application was selected to perform general measurements of vessel sections as described above. Using the 3D volume rendered image in the measurement stage, the rendering parameters were changed to display skin surface, and surface anatomy distances were measured. All distances were measured in millimeters.

2.1.3.1 Measuring the vessel distance between the origin of the brachiocephalic trunk to the external carotid artery (at angle of mandible) via the right common carotid artery (TC+CB+BE).

In the vessel extraction stage of the AVA application, serial seeds (markers) were placed starting at the origin of the brachiocephalic trunk (figure 2.17a, b & c) and ending at the external carotid artery at the level of the angle of the mandible (right), using the axial, coronal, sagittal and 3D volume rendered images. Markers were placed approximately 10 millimeters apart. The manual “Vessel Path” button was selected to extract the vessel centerline.

In the measurement stage of the of the AVA application, the length of the vessel centerline from the brachiocephalic trunk to the external carotid artery at the angle of the mandible (right) were measured (figure 2.18 a & b).

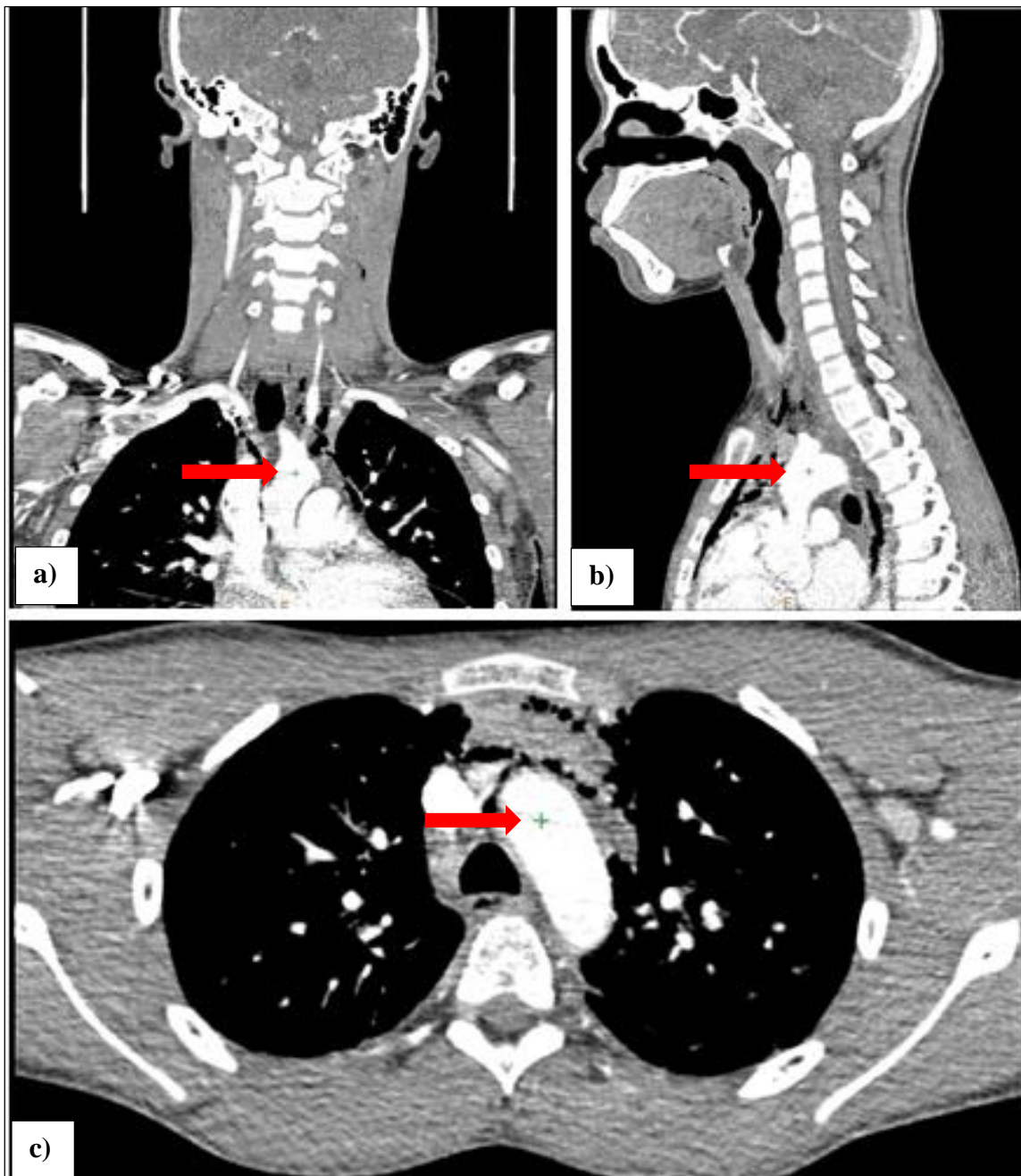


Figure 2.17: Illustrating the placement of the first marker (seed) on the coronal (a), sagittal (b) and axial (c) images, for measurements starting at the brachiocephalic trunk.

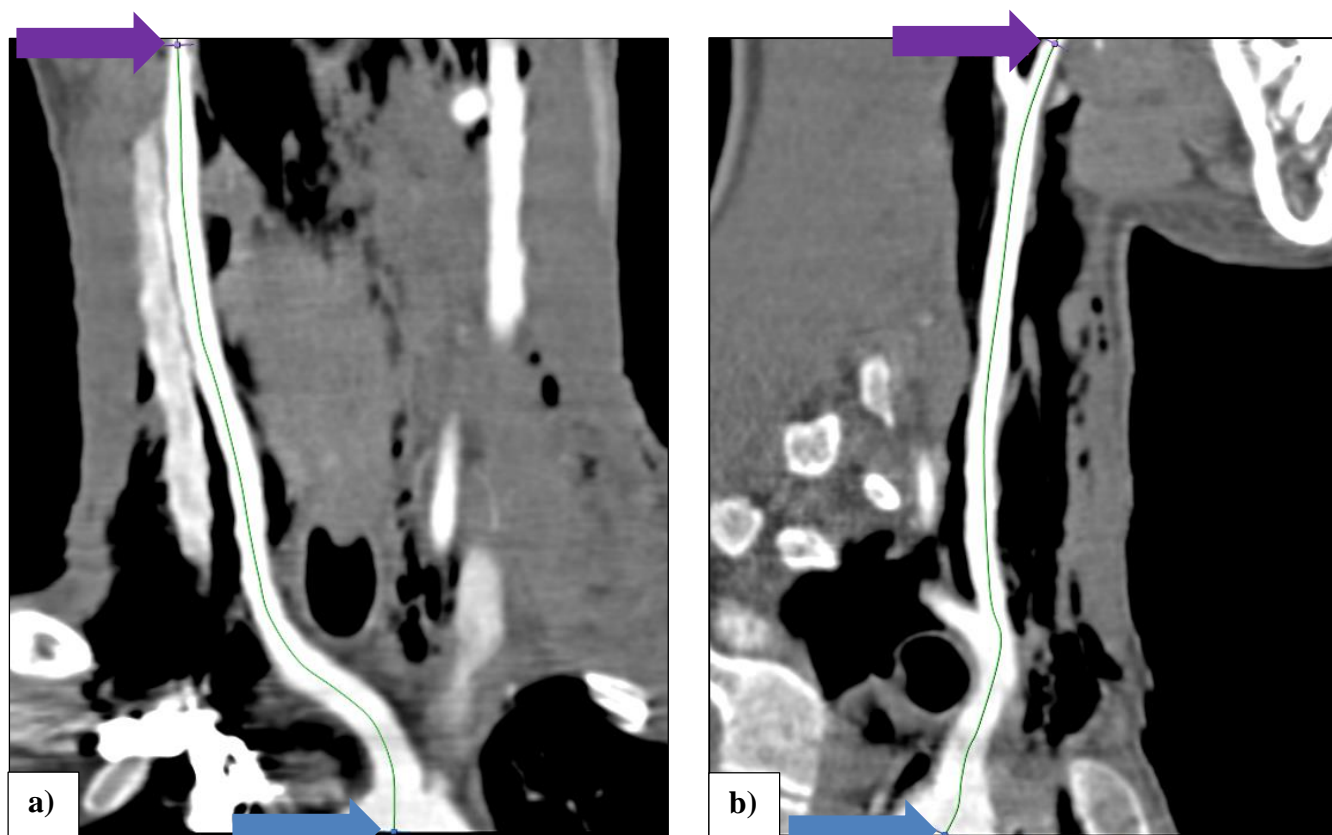


Figure 2.18: Illustration of vessel centerline TC+CD+BE on a curved coronal (a), and on a curved sagittal (b) MPR.

2.1.3.2 Measuring the surface anatomy distance between the angle of the mandible to the suprasternal notch (AS).

In the measurement stage of the AVA application, the rendering parameters of the volume rendered image were changed to display skin surface. The “magic glass” function was selected from the “right click menu”. This “magic glass” function is an enhanced visualizing window that can be superimposed on top of the volume rendered image (that displayed skin surface). It is a moveable mini-window which can be set with its own windowing, image enhancement and rendering parameters to enable the operator to “look through” the skin at the anatomical structures beneath. It was used on top of the volume rendered image (that displayed skin surface). The rendering parameters inside the active magic glass window were changed, to visualize the precise position of the underlying supra-sternal notch (figure 2.19a) and the angle of the mandible (figure 2.19b). The surface distance between these two points was then measured on a

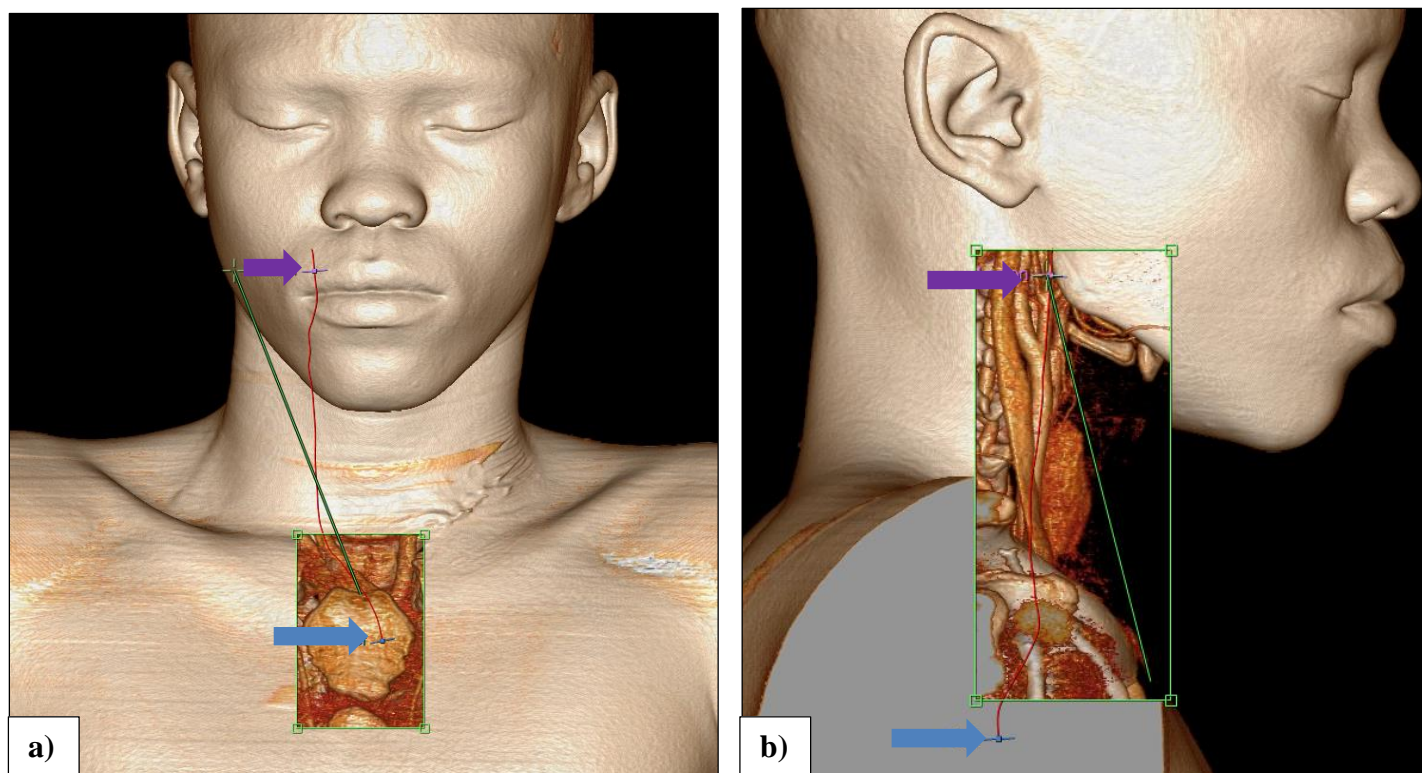


Figure 2.19: Illustrating surface measurement AS on an AP 3D volume rendered image (a) and a lateral 3D volume rendered image (b), using magic glass.

45 degree view as shown in figure 2.20a. Thereafter the volume rendered image was turned 90 degrees (lateral) as shown in figure 2.19b, to check the measuring line placement on the face (angle of the mandible) and then back to zero degrees (AP) position to check the measuring line placement on the supra-sternal notch as shown in figure 2.19a.

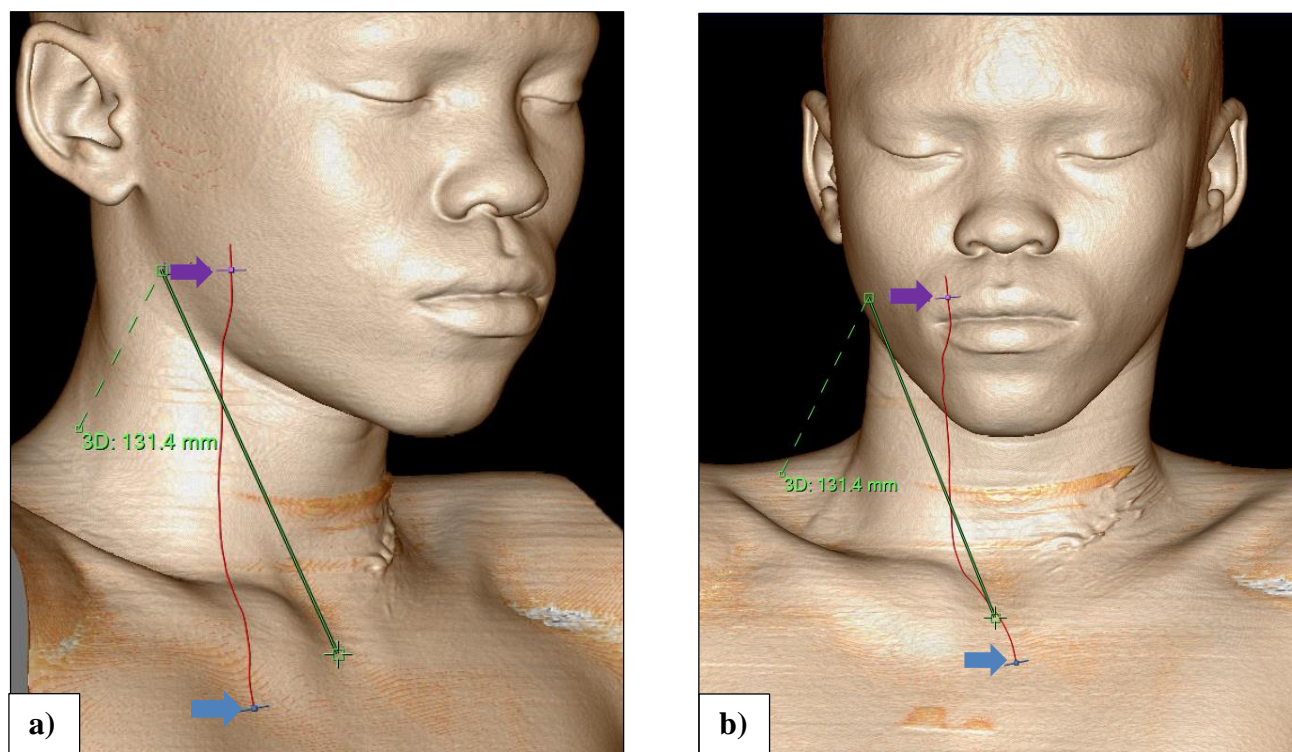


Figure 2.20: Illustrating surface measurement AS on an oblique 3D volume rendered image (a) and an AP 3D volume rendered images (b), after the magic glass have been removed.

2.1.3.3 Vessel distance between the origin of the brachiocephalic trunk to the aorta at the xiphisternum (TX).

In the vessel extraction stage of the AVA application, serial seeds (markers) were placed in the aortic arch, approximately 10 millimeters apart starting at the origin of the brachiocephalic trunk, using the axial, coronal and sagittal images (figure 2.17 a, b & c). From the origin of the descending aorta, only the axial images were used to place markers. The manual “Vessel Path” button was selected to extract the vessel centerline.

In the measurement stage of the AVA application, the length of the vessel centerline from the origin of the brachiocephalic trunk to the distal thoracic aorta at the level of the upper edge of the 10th thoracic vertebrae (figure 2.21, 2.22 & 2.23).

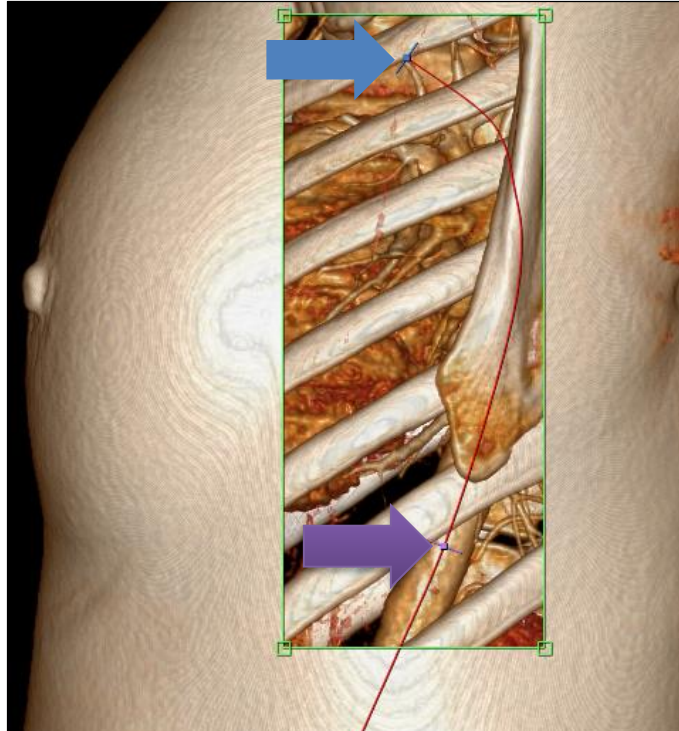


Figure 2.21: Illustrating the start and end points of the vessel measurement TX on a lateral view of a 3D volume rendered image.

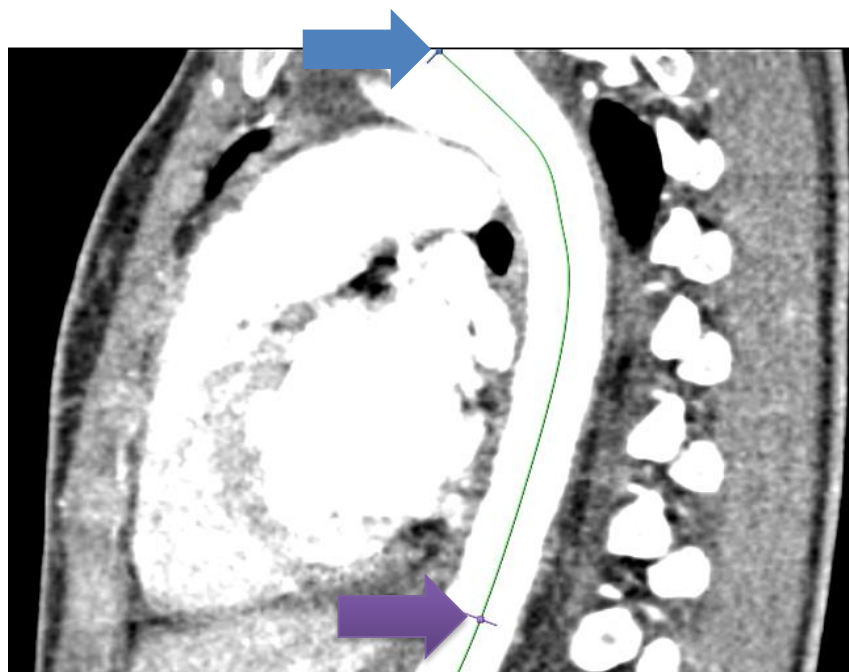
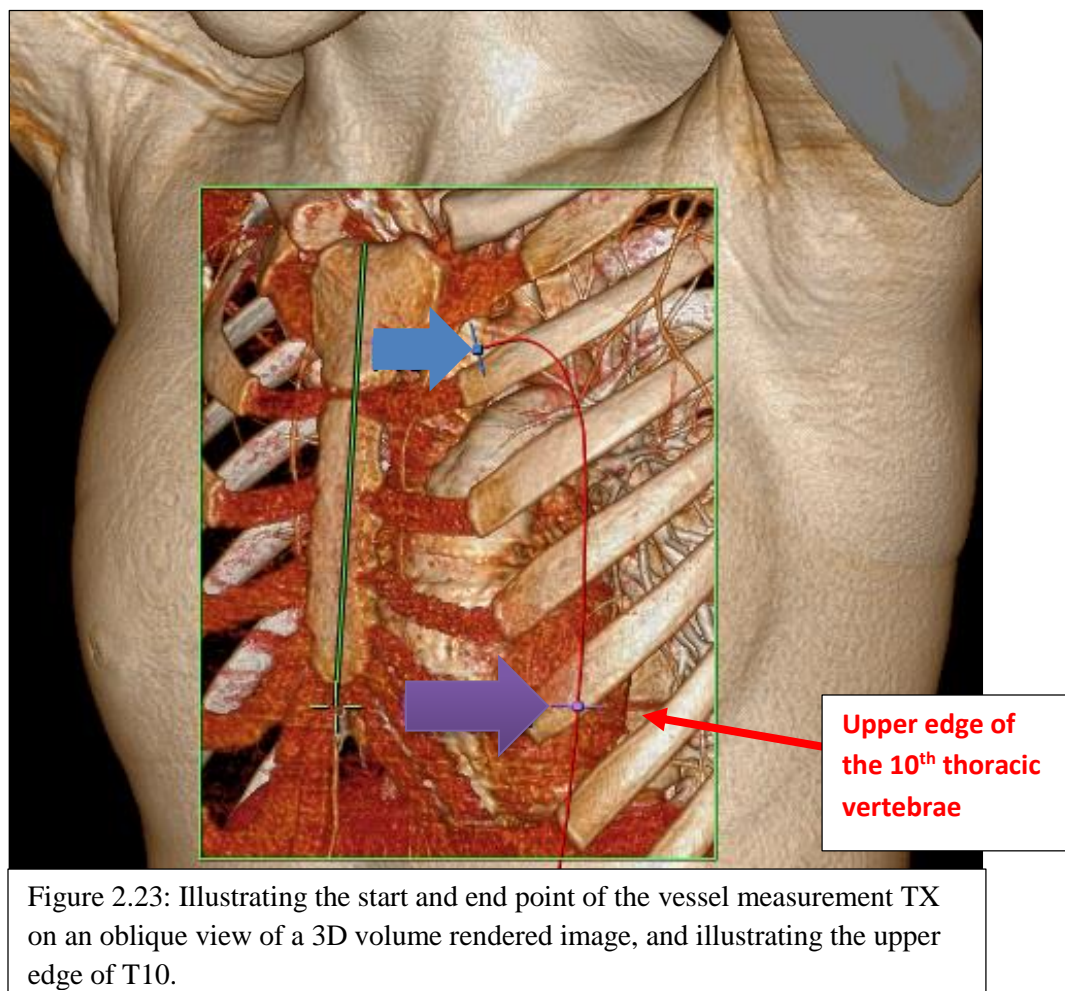


Figure 2.22: Illustrating the start and end points of the vessel measurement TX on a sagittal curved MPR image.



2.1.3.4 Measuring the surface anatomy distance between the suprasternal notch to the xiphisternum (SX).

The rendering parameters of the volume rendered image were then changed to display skin surface. By using the “magic glass” function on top of the volume rendered image (that displayed skin surface), and changing the rendering parameters inside the active “magic glass” window, the researcher was able to measure the surface distance from the suprasternal notch to the xiphisternum at the level of the upper edge of the 10th thoracic vertebra as shown in figures 2.23, 2.24 and 2.25. Cartilage is not always visible on CT imaging and in the case of children, the xiphoid process consists of hyaline cartilage which only ossifies in mid-adulthood. Therefore, where the xiphisternum was indistinct, its position was estimated using the upper edge of the 10th thoracic vertebra as a guide.

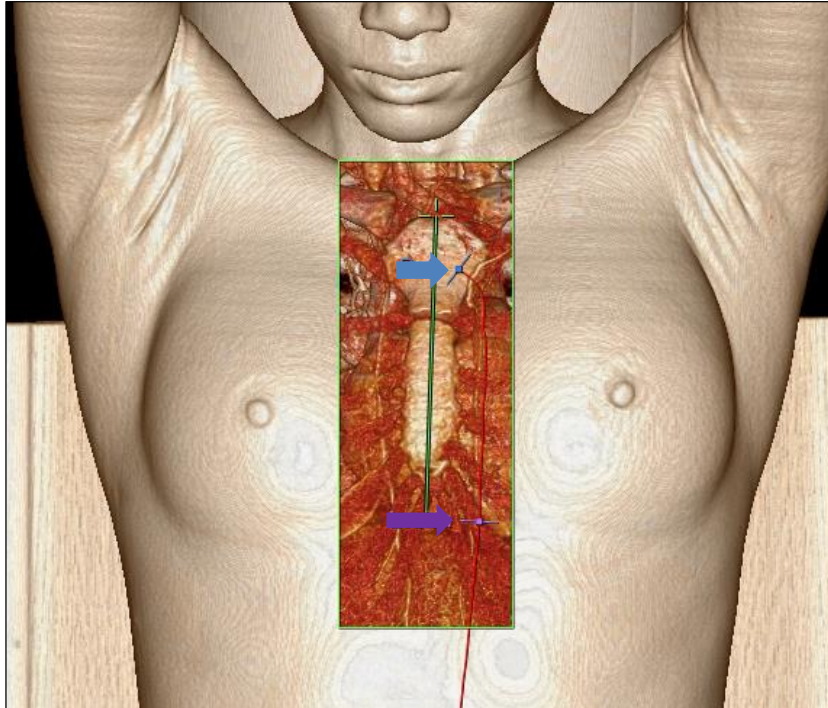


Figure 2.24: Illustrating surface measurement SX, using the magic glass.

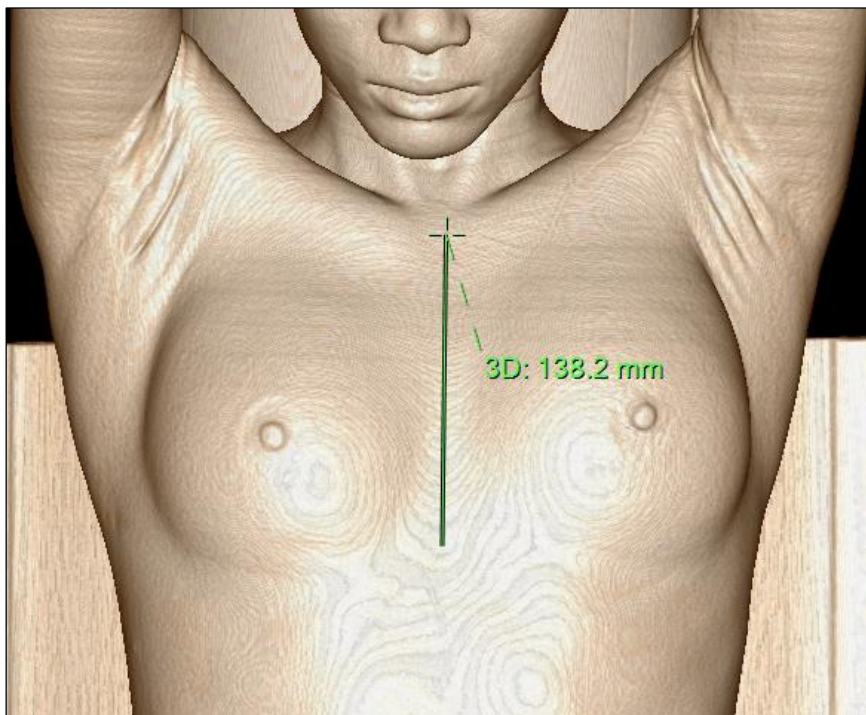
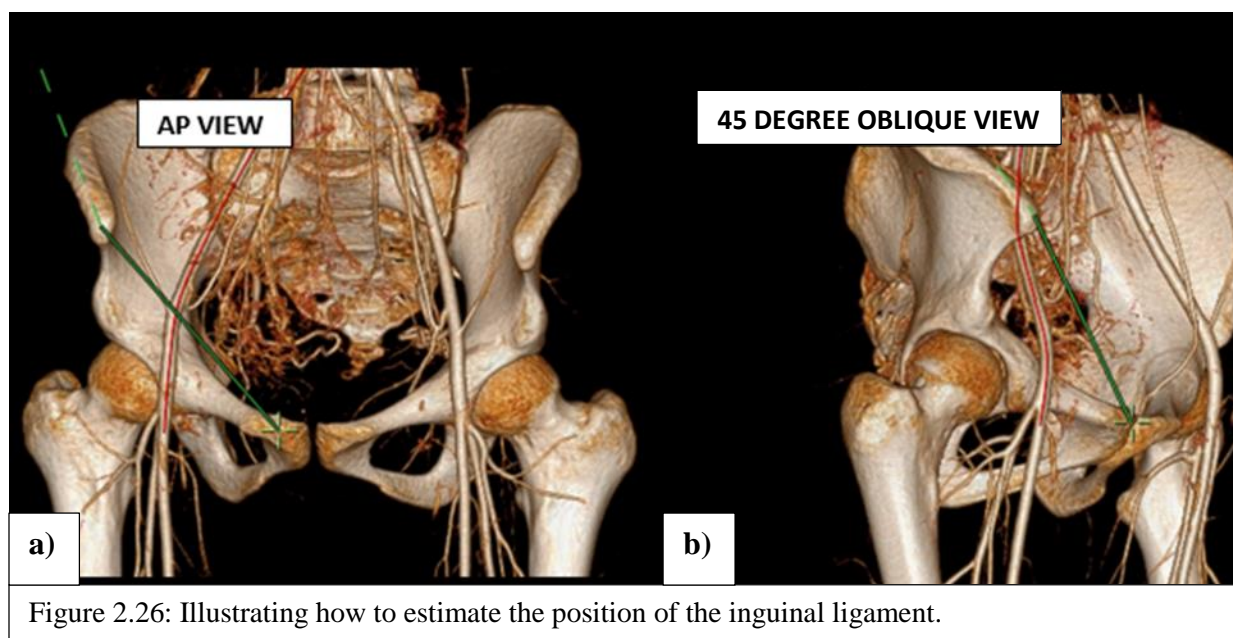


Figure 2.25: Illustrating surface measurement SX, after the magic glass has been removed.

2.1.3.5 Measuring the vessel distance between the aorta at the xiphisternum to the aortic bifurcation, and from the aortic bifurcation to the right femoral artery at the right inguinal ligament (XA+AF).

According to Tortora and Grabowski (2003: 332), the inguinal ligament runs from the anterior superior iliac spine to the pubic tubercle. Therefore a line was drawn from the right anterior superior iliac spine to the right pubic tubercle (figure 2.26 a & b), to estimate the position of the inguinal ligament and estimate the point at which the right femoral artery crosses it, since the inguinal ligament was not visible on CT imaging. The vessel centerline path was extracted by using the same seed (marker) placement method as above.

In the measurement stage, the length of the vessel was measured starting at the level of the upper edge of the 10th thoracic vertebra to the aortic bifurcation and from the aortic bifurcation to the right femoral artery at the level of right inguinal ligament (figure 2.27 a & b).



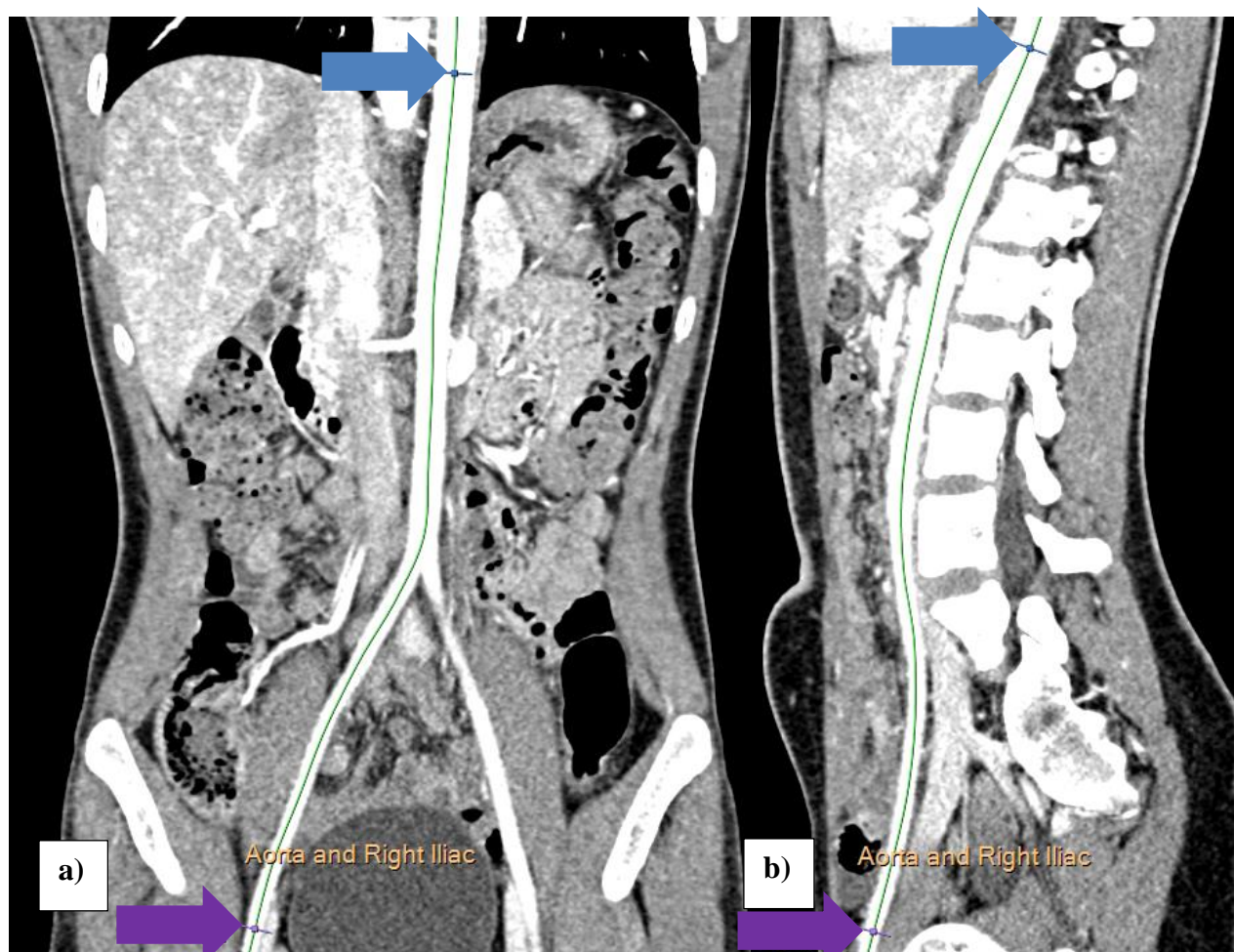


Figure 2.27: Illustrating the start and end points of the vessel measurement XI on a coronal (a) and sagittal (b) curved MPR.

2.1.3.6 Measuring the surface anatomy distance from the xiphisternum to the midpoint of the right inguinal crease (XI).

The rendering parameters of the volume rendered image were then changed to display skin surface. By using the “magic glass” function on top of the volume rendered image and changing the rendering parameters inside the active “magic glass” window, the researcher was able to measure the surface distance from the xiphisternum (at the level of the upper edge of the 10th thoracic vertebra) to the midpoint of the right inguinal crease (figure 2.28).

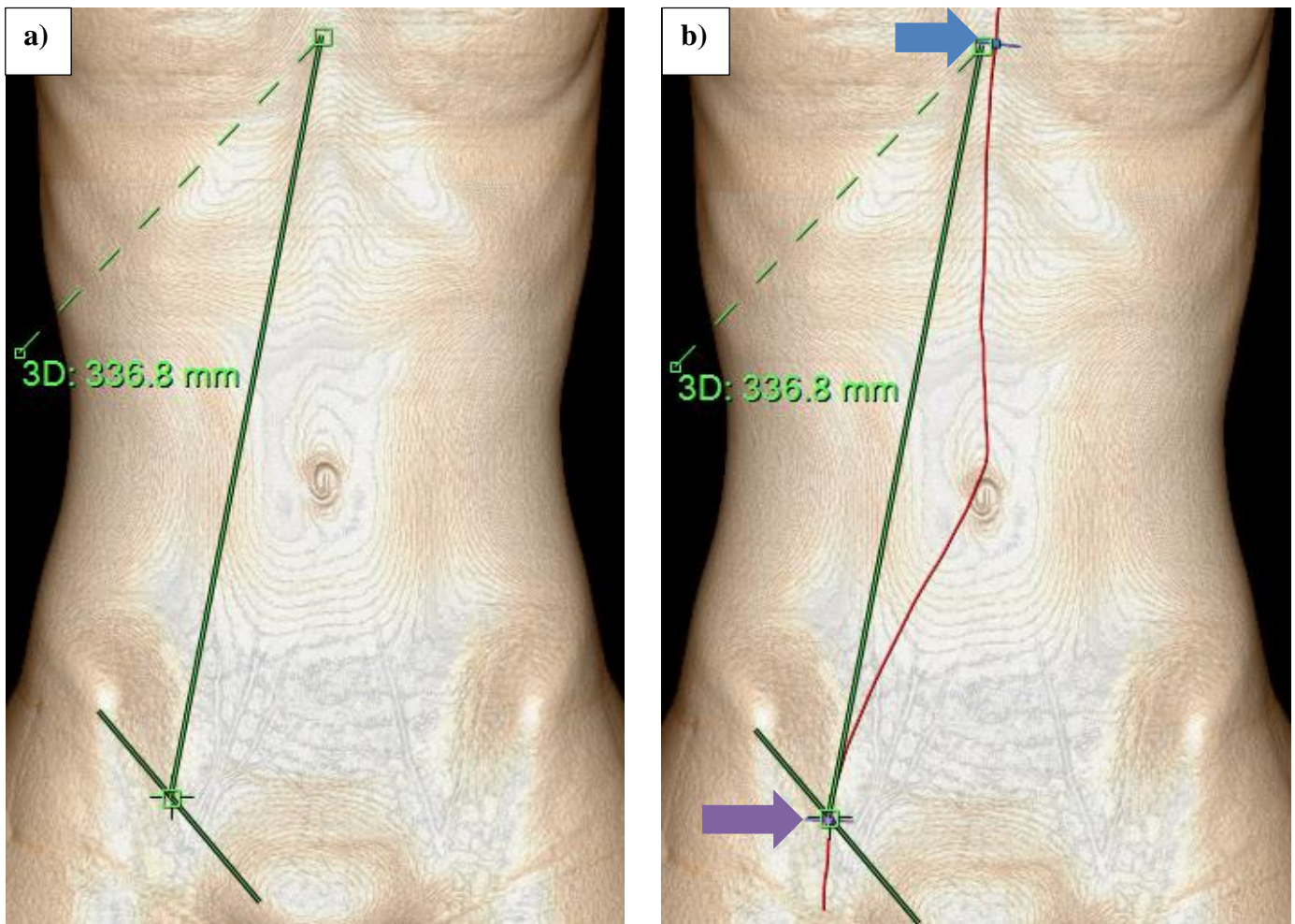


Figure 2.28: Illustration of surface measurement XI (a), and this was compared to vessel distance XA+AF in red (b).

2.1.3.7 Measuring the surface anatomy distance from the xiphisternum to the umbilicus and the distance between the umbilicus to the midpoint of the right inguinal crease (XU+UI).

The rendering parameters of the volume rendered image were then changed to display skin surface. By using the “magic glass” function on top of the volume rendered image and changing the rendering parameters inside the active “magic glass” window, the researcher was able to measure the surface distance from the xiphisternum (at the level of the upper edge of the 10th thoracic vertebra) to the umbilicus, and from the umbilicus to the midpoint of the right inguinal crease (figure 2.29).

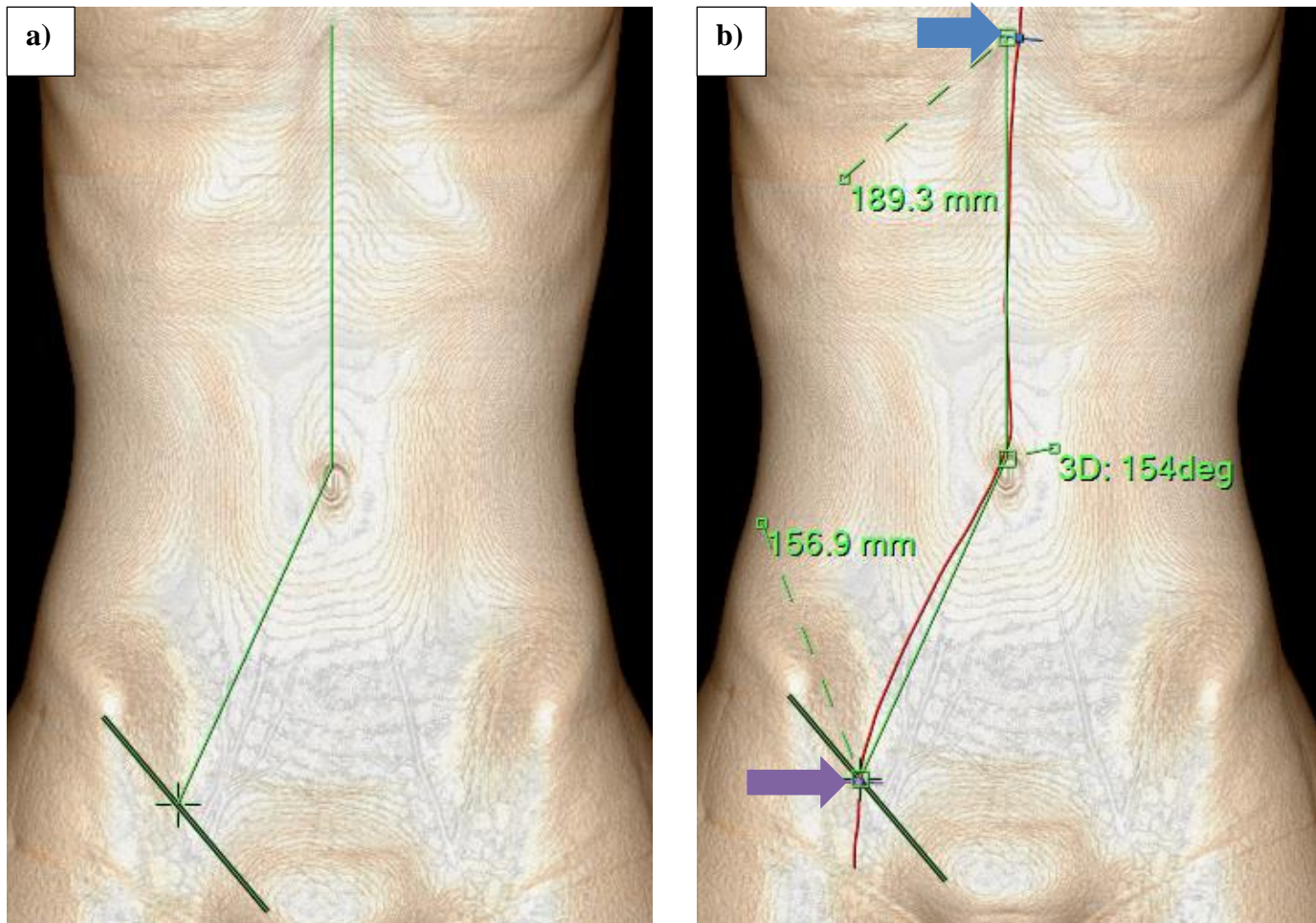


Figure 2.29: Illustration of surface measurement XU+UI (a), and this was compared to vessel distance XA+AF in red (b).

2.1.3.8 Vessel distance between the origin of the brachiocephalic trunk to the aortic bifurcation, and from the aortic bifurcation to right femoral artery at the inguinal ligament (TX+XA+AF).

In the vessel extraction stage of the AVA application, serial markers (seeds) were placed in the aortic arch starting at the origin of the brachiocephalic trunk to the right femoral artery at the inguinal ligament, using the axial, coronal, sagittal and 3D volume rendered images. From the origin of the descending aorta, only the axial images were used to place markers. The manual Vessel Path button was selected to extract the vessel centerline.

In the measurement stage of the AVA application, the length of the vessel centerline from the brachiocephalic trunk to the right femoral artery at the right inguinal ligament were measured (figure 2.30).

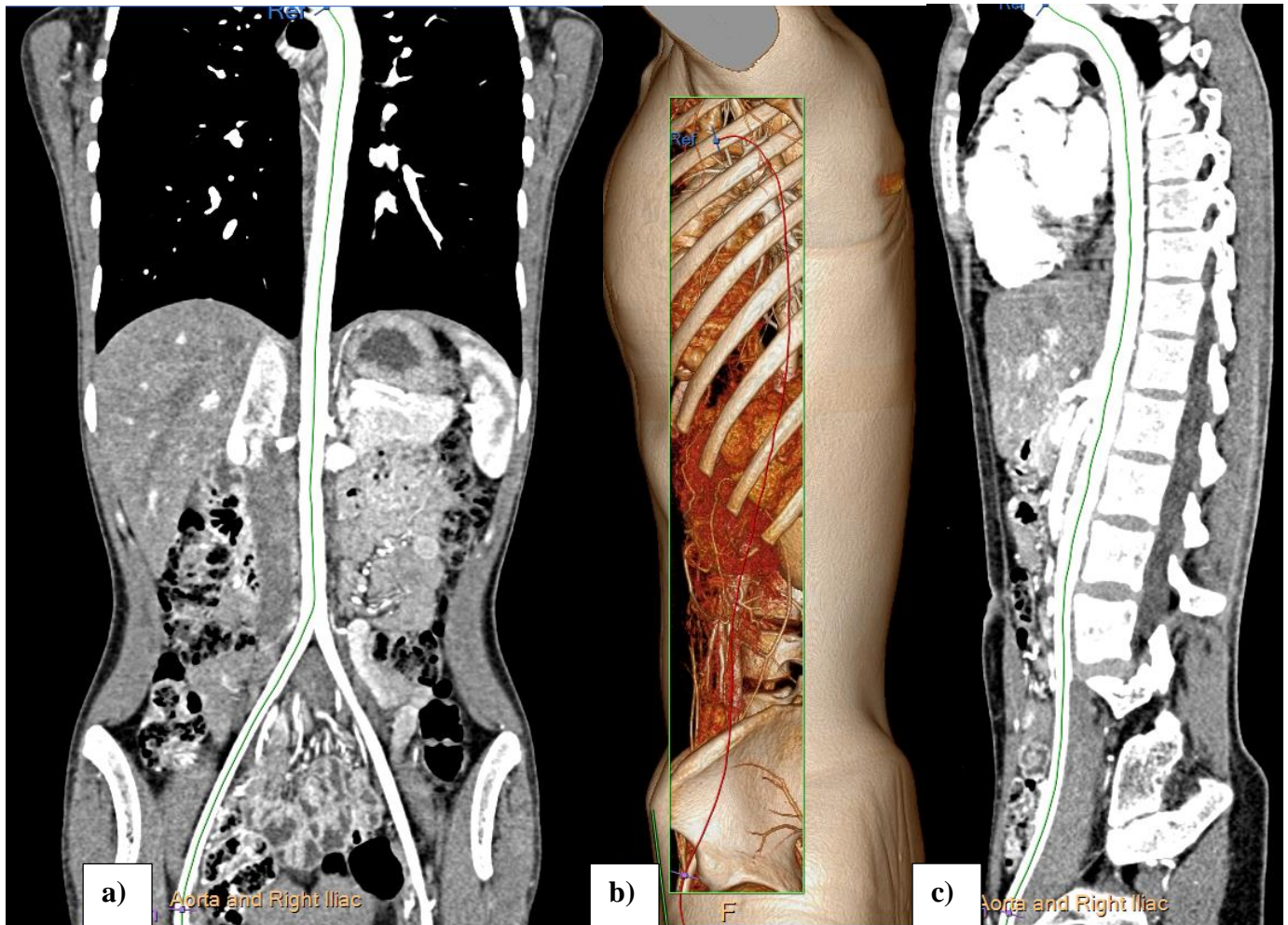


Figure 2.30: Demonstration of the intra-arterial path length on a curved multi-planar reformat (a & c) and on a lateral volume rendered image (b), starting at the origin of the brachiocephalic trunk and ending in the right femoral artery.

2.1.3.9 Measuring the surface anatomy distance between the suprasternal notch to the midpoint of the right inguinal crease (SI).

The rendering parameters of the volume rendered image were then changed to display skin surface. By using the “magic glass” function on top of the volume rendered image and changing the rendering parameters inside the active “magic glass” window, the researcher was able to measure the surface anatomy from the suprasternal notch to the midpoint of the right inguinal crease (figure 2.31).

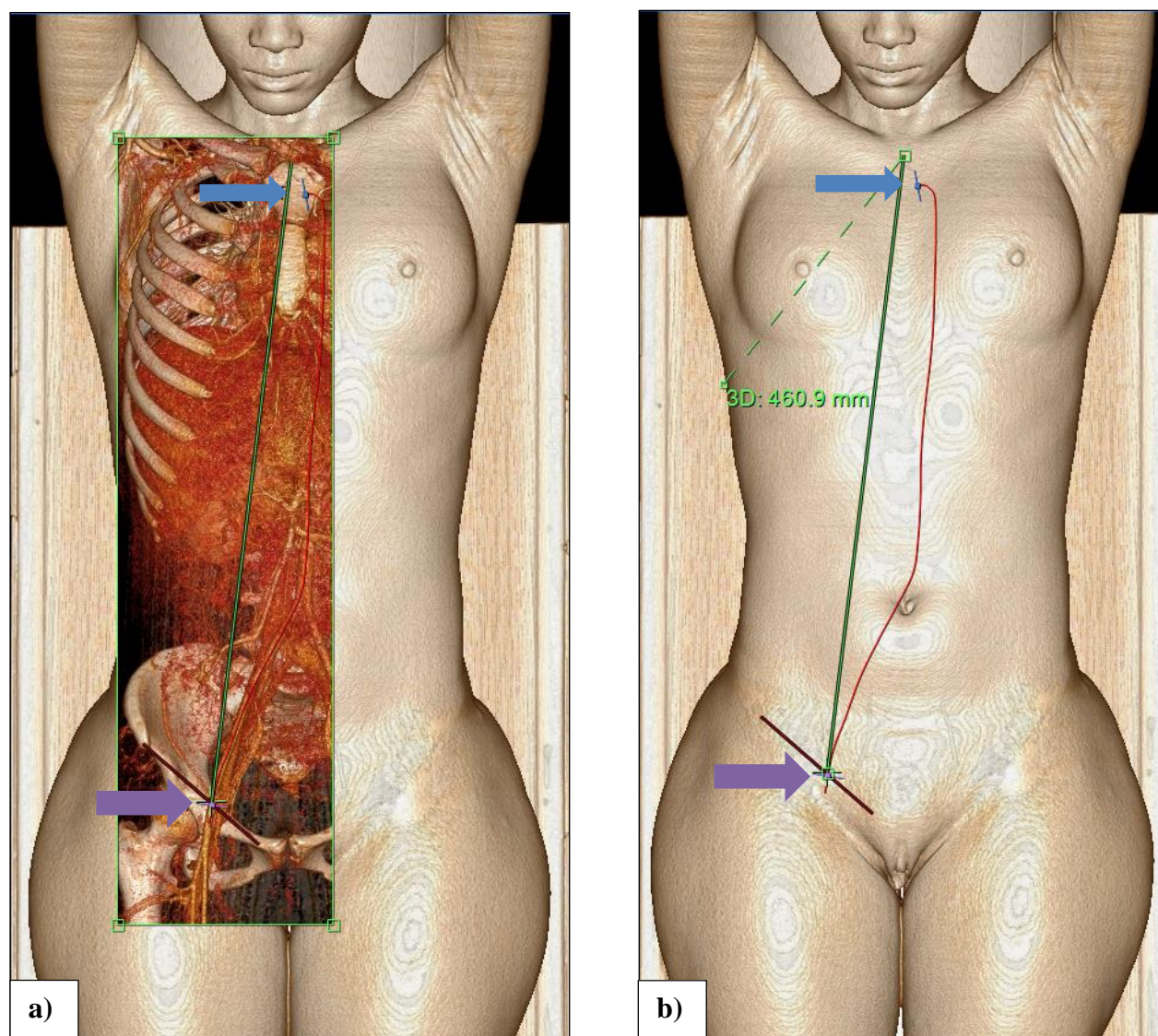


Figure 2.31: Illustration of surface measurement SI, using the magic glass (a), and then displaying the distance after the magic glass has been removed (b).

2.1.3.10 Measuring the surface anatomy distance between the suprasternal notch to the xiphisternum, and the surface distance between xiphisternum and the midpoint of the right inguinal crease (SX+XI).

By using the same method as above, the researcher was able to measure the surface anatomy distance from the suprasternal notch to the xiphisternum, and the surface distance between xiphisternum and the midpoint of the right inguinal crease (figure 2.32).

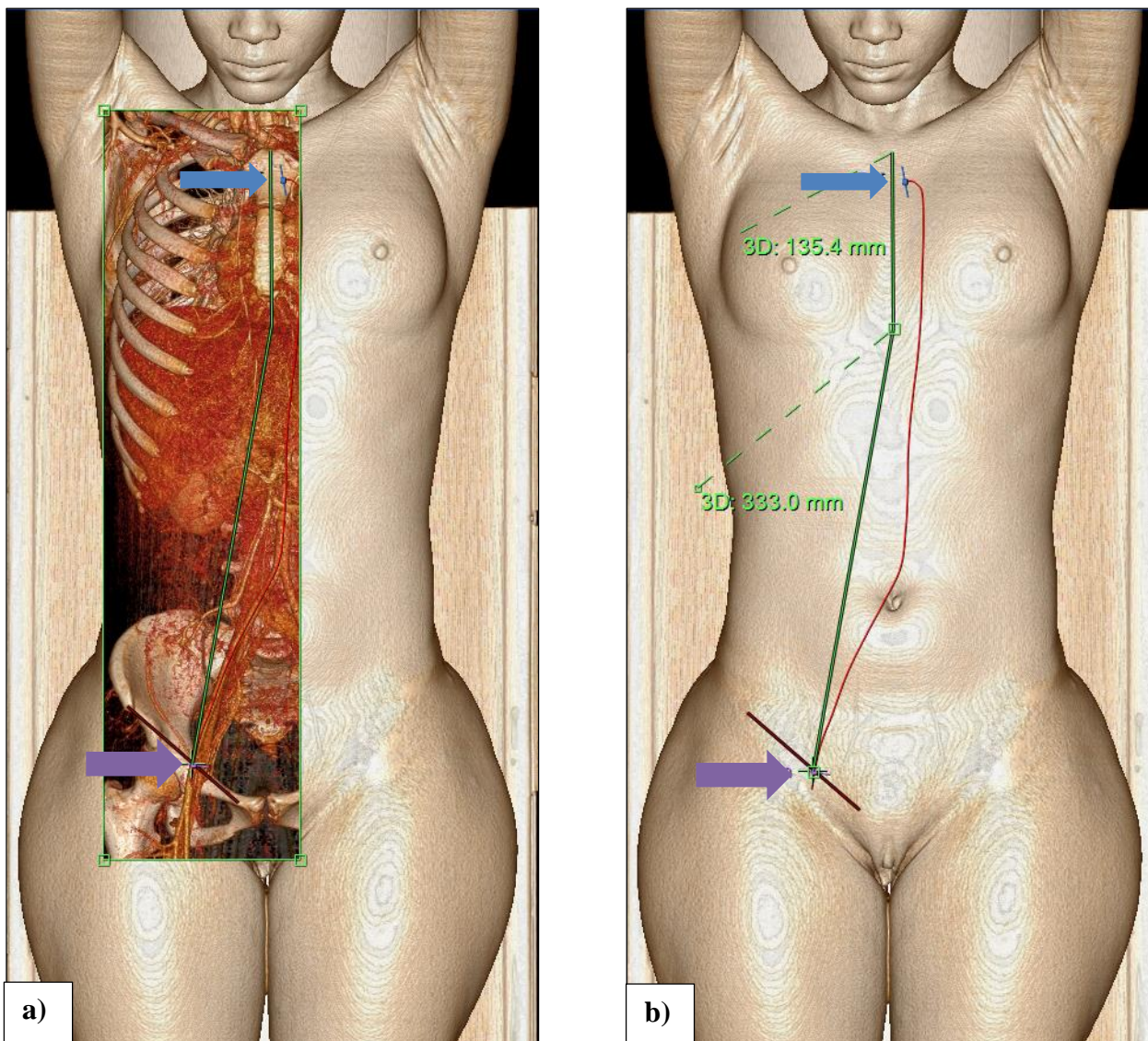


Figure 2.32: Illustration of surface measurement SX+XI, using the magic glass (a), and then displaying the distances after the magic glass has been removed (b).

2.1.3.11 Measuring the surface anatomy distance between the suprasternal notch and the xiphisternum, and the surface distance between xiphisternum and the umbilicus, plus the surface distance between the umbilicus and the midpoint of the right inguinal crease (SX+XU+UI).

By using the same method as above, the researcher was able to measure the surface anatomy distance from the suprasternal notch to the xiphisternum, and the surface anatomy distance between xiphisternum and the umbilicus, and the surface distance between the umbilicus and the midpoint of the right inguinal crease (figure 2.33).

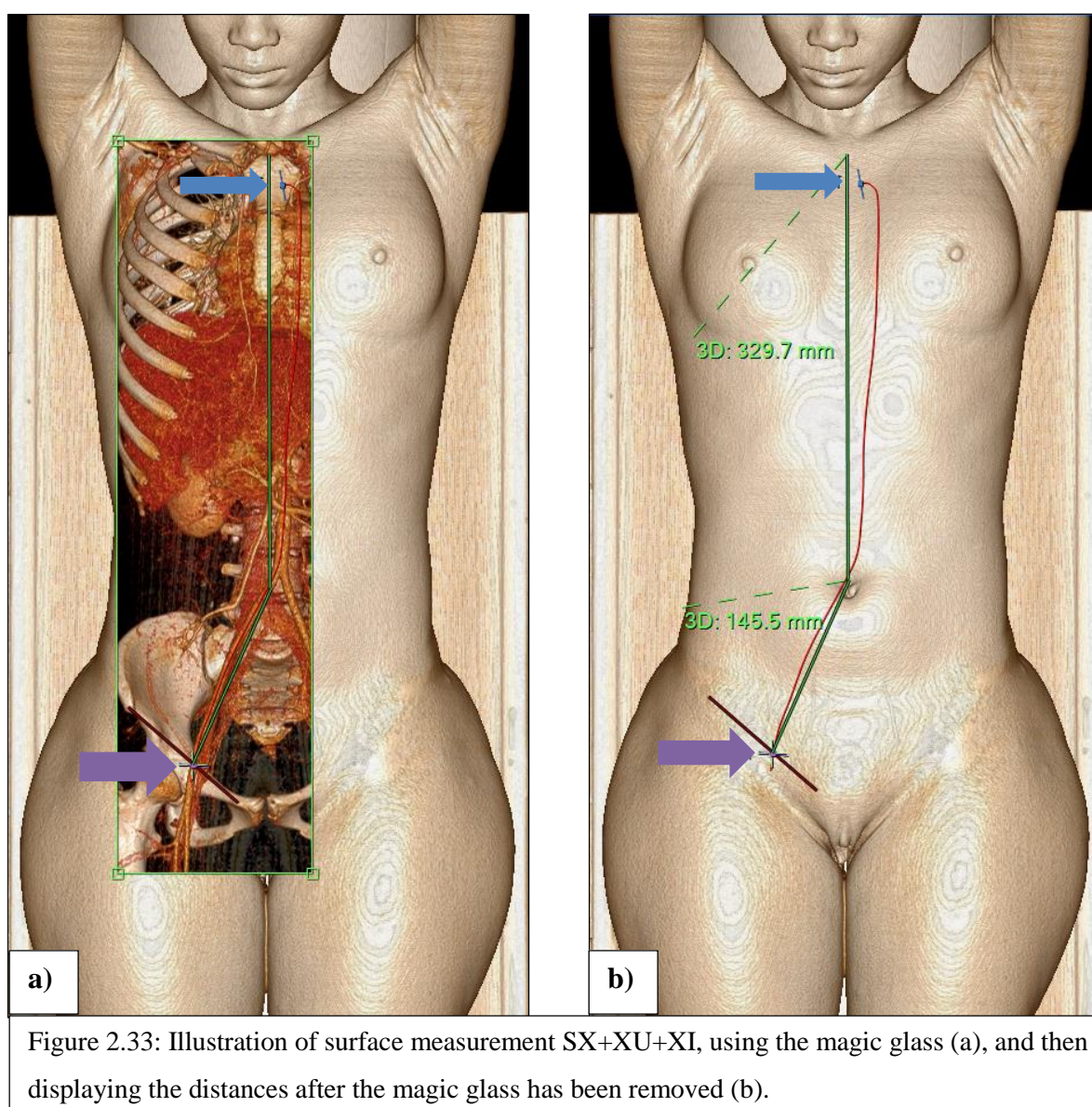


Figure 2.33: Illustration of surface measurement SX+XU+UI, using the magic glass (a), and then displaying the distances after the magic glass has been removed (b).

CHAPTER 3

3.1 RESULTS

Table 3.1: Demographics for each comparison group.

Comparison	Median age in years (IQR)	n
TC+CD+BE compared to AS	15 (11 - 17)	67
TX compared to SX	6 (2 - 11)	152
XA+AF compared to XI	13 (6 - 17)	105
XA+AF compared to XU+UI	13 (6 - 17)	107
TX+XA+AF compared to SI	15 (12 - 17)	18
TX+XA+AF compared to SX+XI	15 (12 - 17)	18
TX+XA+AF compared to SX+XU+UI	15 (13 - 17)	17

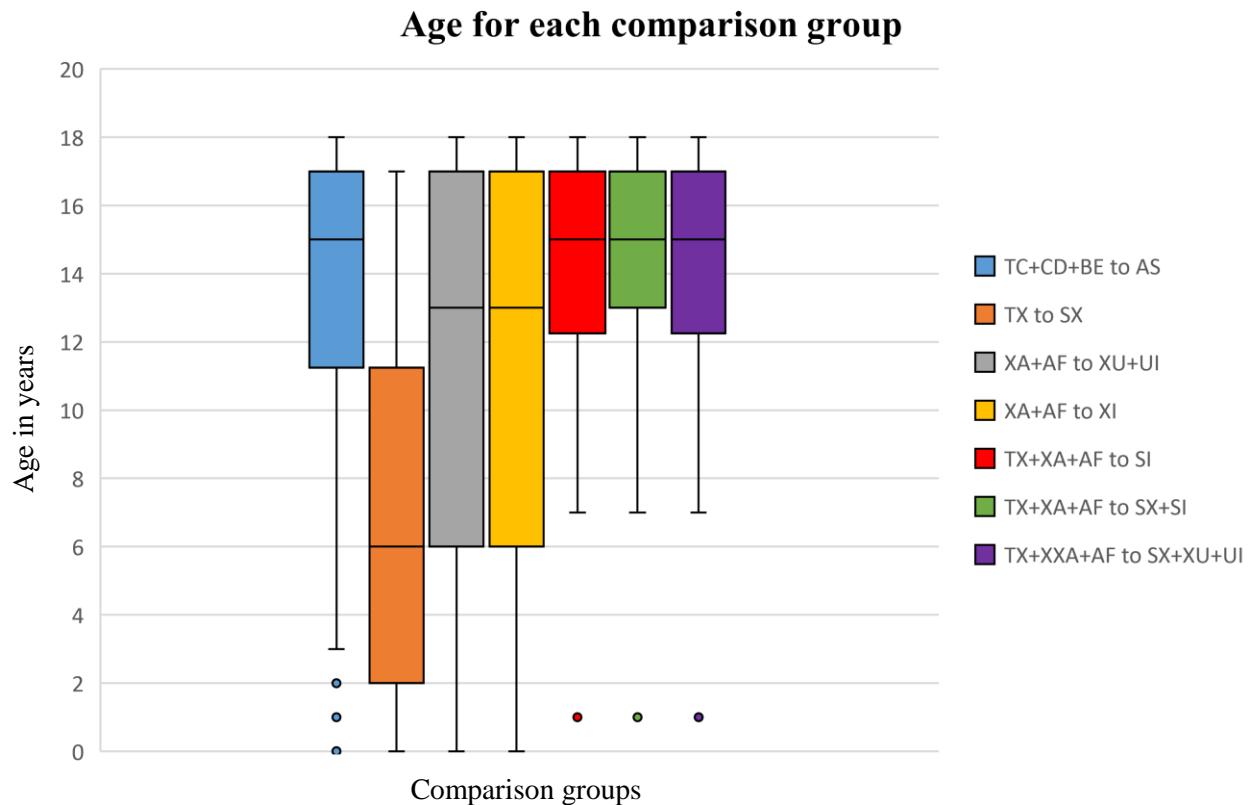


Figure 3.1: Age for each comparison group

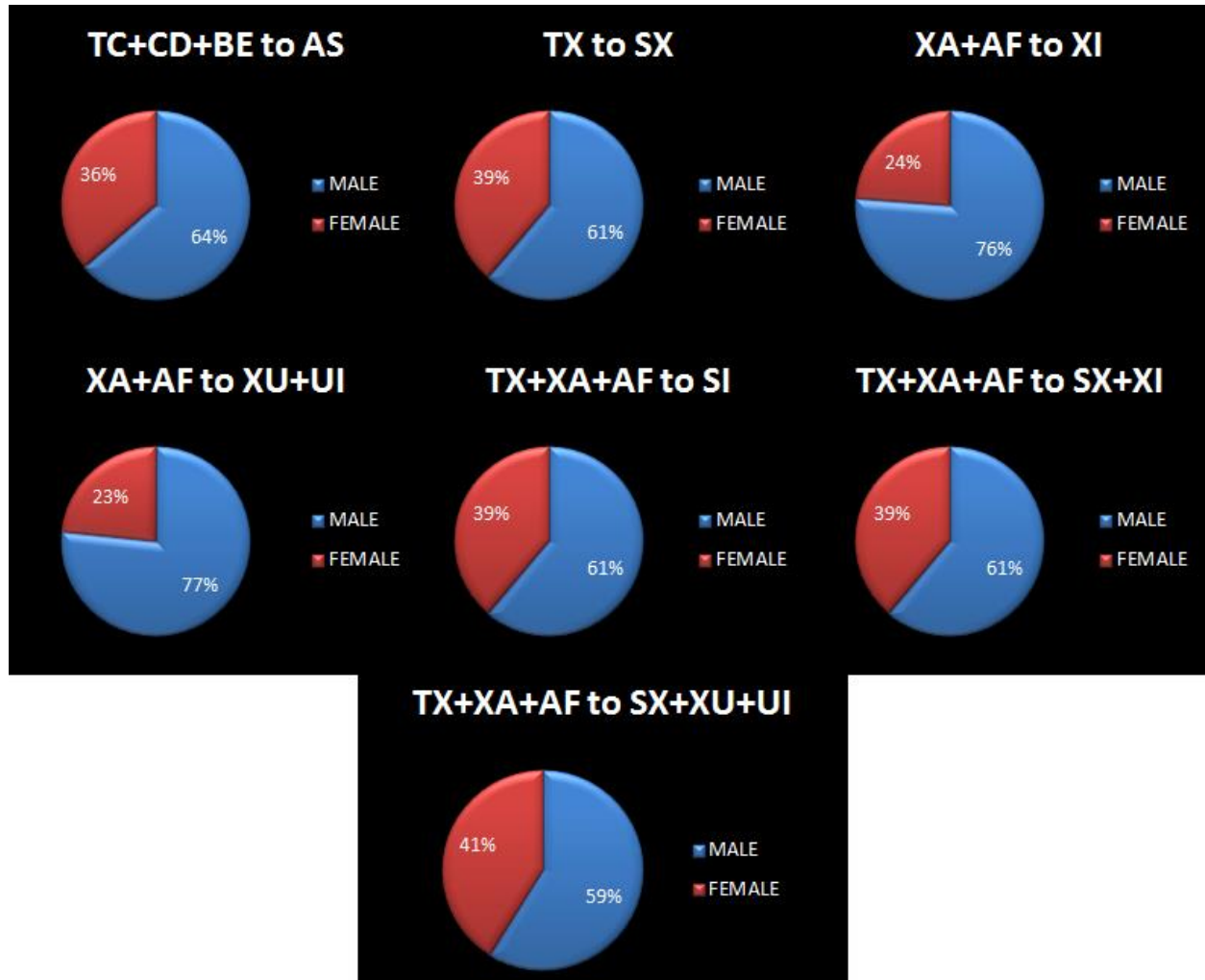


Figure 3.2: Percentage of male and female for each comparison.

3.1.1 Scatterplot of TC+CD+BE compared to AS

Sixty-six archived CT scans were used for this comparison, with the youngest person being nine months old and the oldest being eighteen years old.

Linear regression analysis showed a significant relationship between the surface anatomy measurements (AS) and vessel measurements (TC + CB + BE). There was a positive correlation between the two variables ($r^2 = 0.92$, $p < 0.0001$). A scatterplot summarizes the results (Figure 3.3).

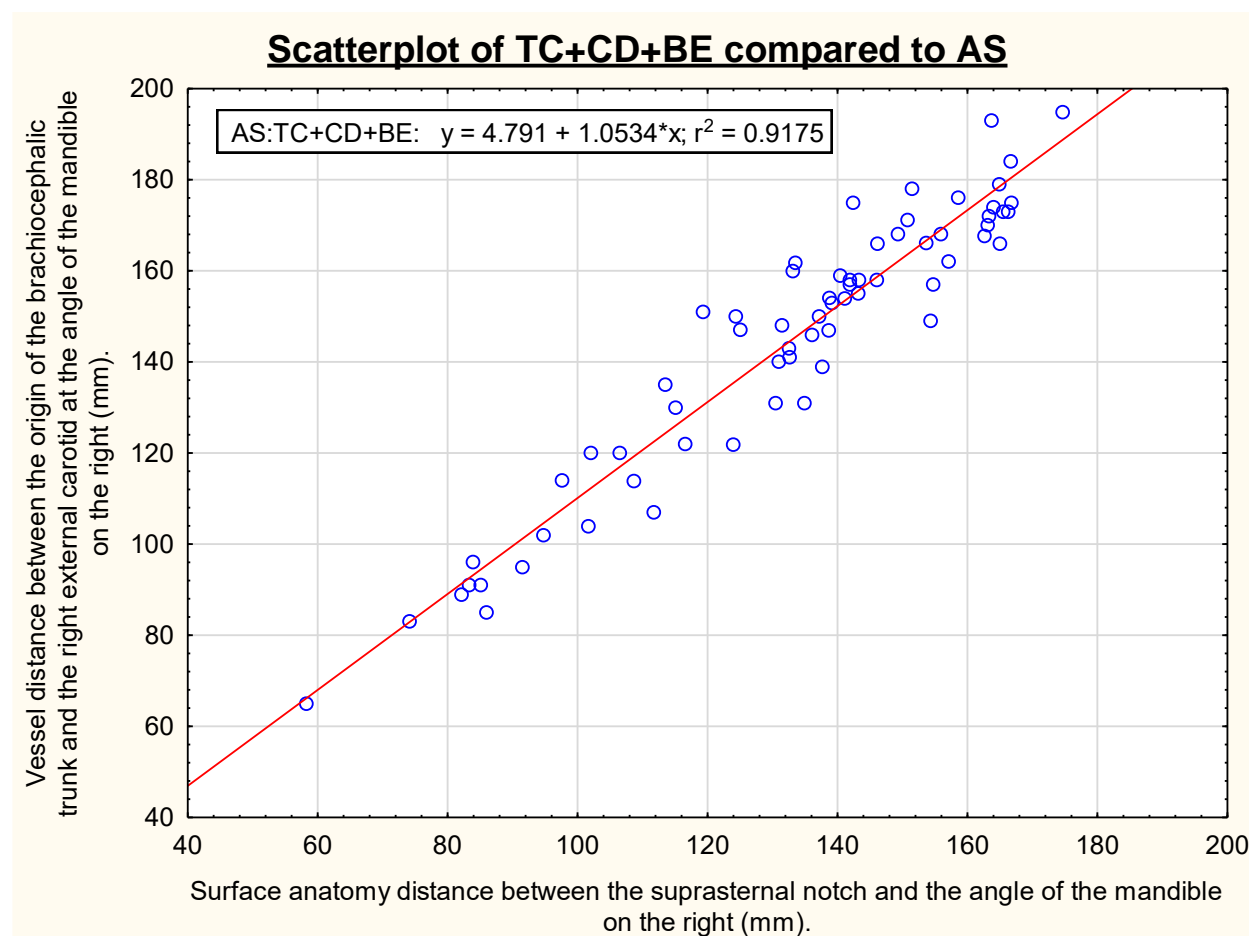


Figure 3.3: Relationship between vessel distance TC+CD+BE (origin of the brachiocephalic trunk to the external carotid at the angle of the mandible on the right) and surface anatomy distance AS (suprasternal notch to the angle of the mandible) in children younger than 18 years. Linear regression analysis showed a strong positive correlation ($r^2 = 0.92$).

3.1.2 Scatterplot of TX compared to SX

One hundred and fifty two archived CT scans were used for this comparison, with the youngest person being three weeks old and the oldest being seventeen years old.

Linear regression analysis showed a significant relationship between the surface anatomy measurements (SX) and vessel measurements (TX). There was a positive correlation between the two variables ($r^2 = 0.84$, $p < 0.0001$). A scatterplot summarizes the results (Figure 3.4).

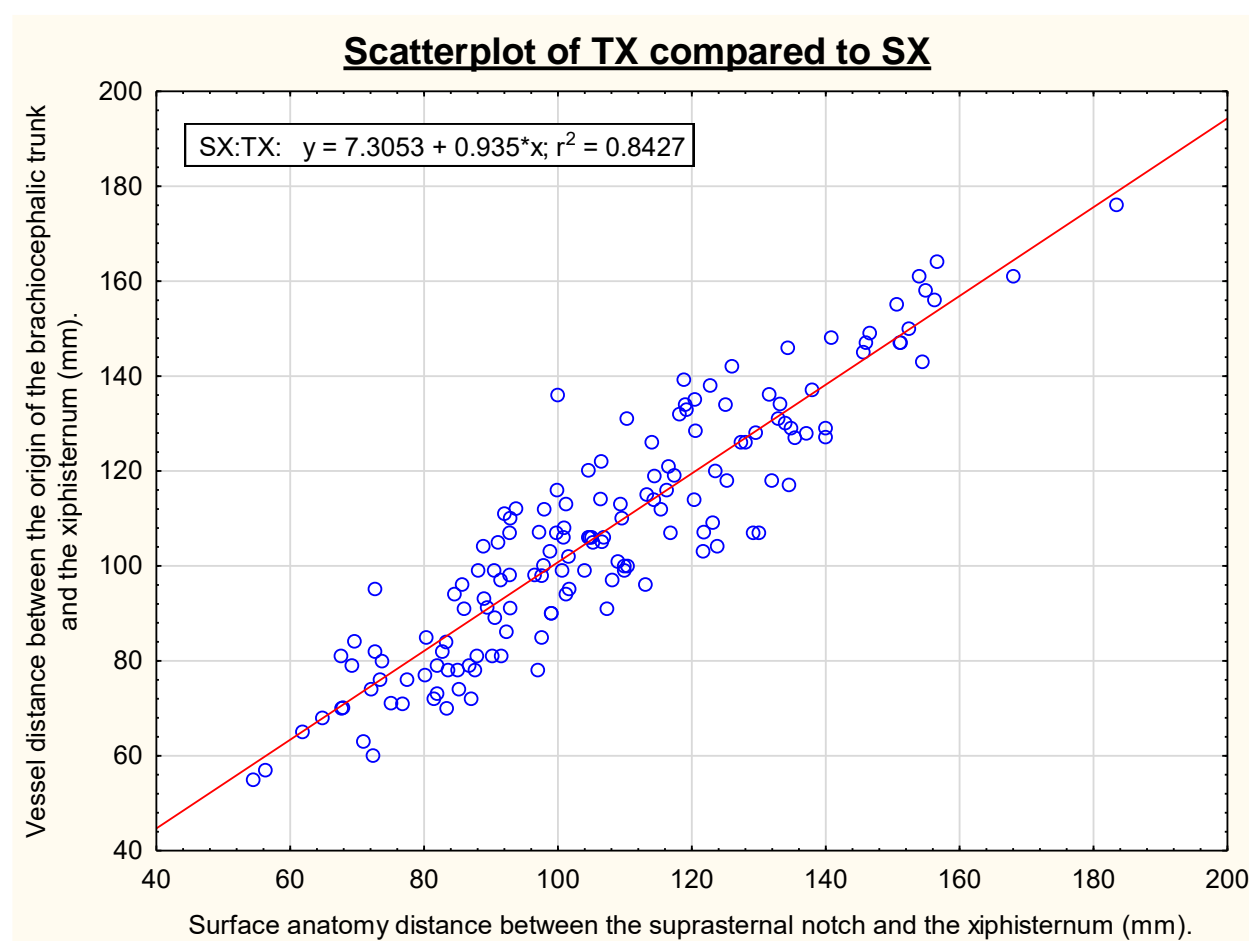


Figure 3.4: Relationship between vessel distance TX (origin of the brachiocephalic trunk to the aorta at the xiphisternum) and surface anatomy distance SX (suprasternal notch to the xiphisternum) in children younger than 18 years. Linear regression analysis showed a positive correlation ($r^2 = 0.84$).

3.1.3 Scatterplot of XA+AF compared to XI

One hundred and five archived CT scans were used for this comparison, with the youngest person being six weeks old and the oldest being eighteen years old.

Linear regression analysis showed a significant relationship between the surface anatomy measurements (XI) and vessel measurements (XA + AF). There was a positive correlation between the two variables ($r^2 = 0.99$, $p < 0.0001$). A scatterplot summarizes the results (Figure 3.5).

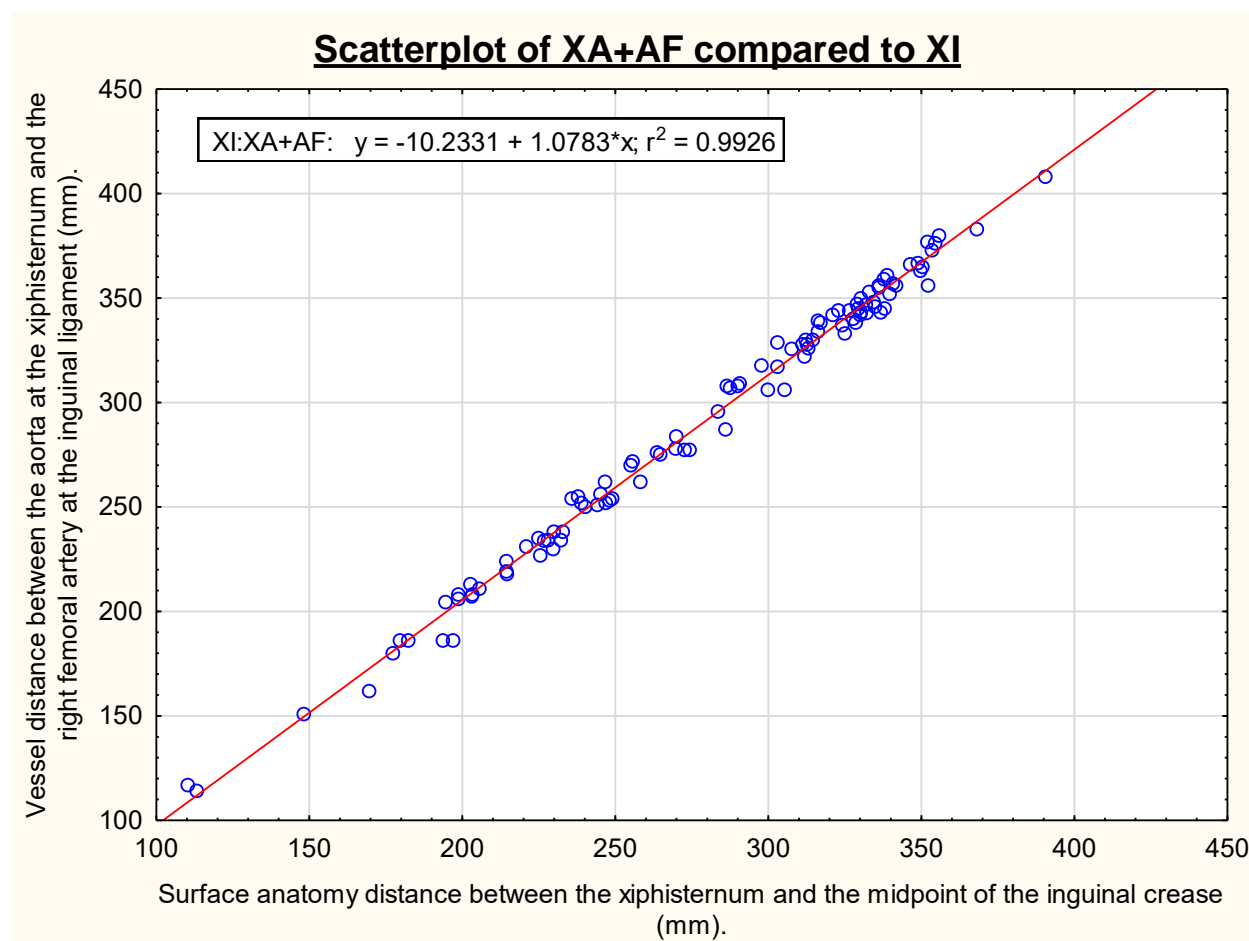


Figure 3.5: Relationship between vessel distance XA+AF (aorta at the xiphisternum to the right femoral artery at the inguinal ligament) and the surface anatomy distance XI (xiphisternum to the midpoint of the right inguinal crease) in children younger than 18 years. Linear regression analysis showed a very strong positive correlation ($r^2 = 0.99$).

3.1.4 Scatterplot of XA +AF compared to XU+UI

One hundred and seven archived CT scans were used for this comparison, with the youngest person being six weeks old and the oldest being eighteen years old.

Linear regression analysis showed a significant relationship between the surface anatomy measurements (XU+ UI) and vessel measurements (XA + AF). There was a positive correlation between the two variables ($r^2= 0.99$, $p<0.0001$), A scatterplot summarizes the results (Figure 3.6).

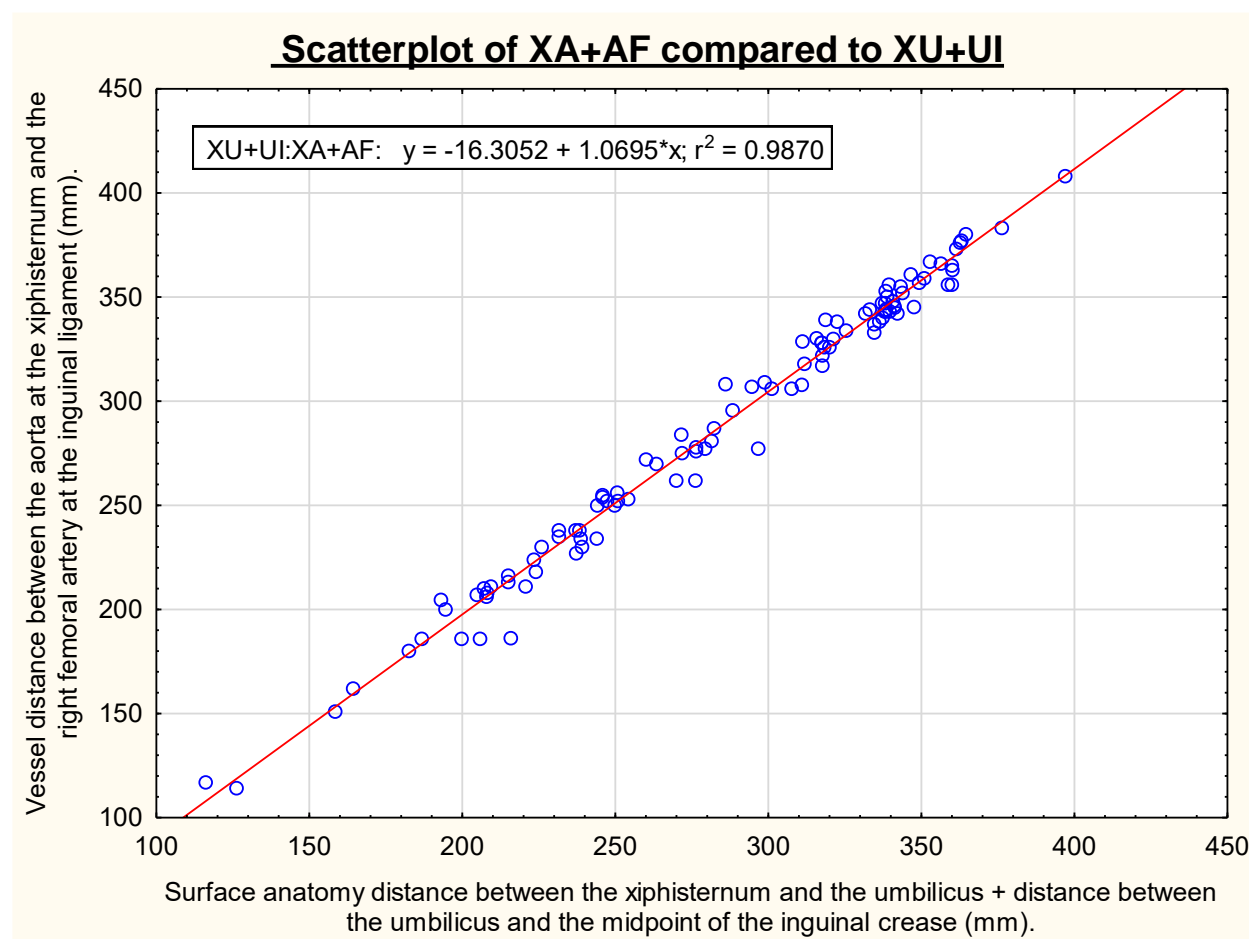


Figure 3.6: Relationship between vessel distance XA+AF (aorta at the xiphisternum to the right femoral artery at the inguinal ligament) and the surface anatomy distance XU+UI (xiphisternum to the umbilicus, plus umbilicus to the midpoint of the right inguinal crease) in children younger than 18 years. Linear regression analysis showed a very strong positive correlation ($r^2=0.99$).

3.1.5 Scatterplot of TX+XA+AF compared to SI

Eighteen archived CT scans were used for this comparison, with the youngest person being one year old and the oldest being eighteen years old.

Linear regression analysis showed a significant relationship between the surface anatomy measurements (SI) and vessel measurements (TX+XA+AF). There was a positive correlation between the two variables ($r^2 = 0.98$, $p < 0.0001$). A scatterplot summarizes the results (Figure 3.7).

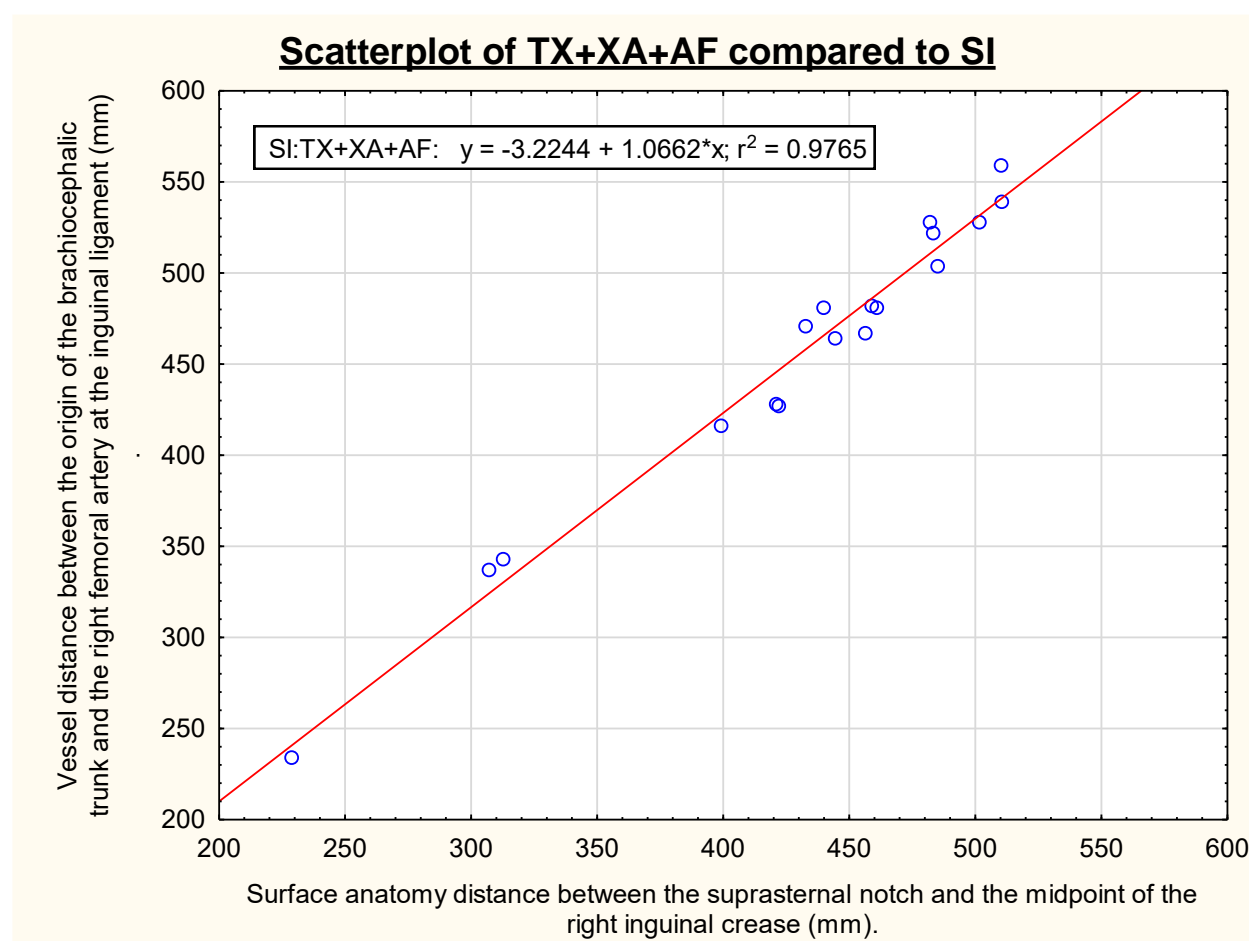


Figure 3.7: Relationship between vessel distance TX+XA+AF (origin of the brachiocephalic trunk to the right femoral artery at the inguinal ligament) and the surface anatomy distance SI (suprasternal notch to the midpoint of the right inguinal crease) in children younger than 18 years. Linear regression analysis showed a very strong positive correlation ($r^2 = 0.98$).

3.1.6 Scatterplot of TX+XA+AF compared to SX+XI

Eighteen archived CT scans were used for this comparison, with the youngest person being one year old and the oldest being eighteen years old.

Linear regression analysis showed a significant relationship between the surface anatomy measurements (SX+XI) and vessel measurements (TX+XA+AF). There was a positive correlation between the two variables ($r^2 = 0.97$, $p < 0.0001$). A scatterplot summarizes the results (Figure 3.8).

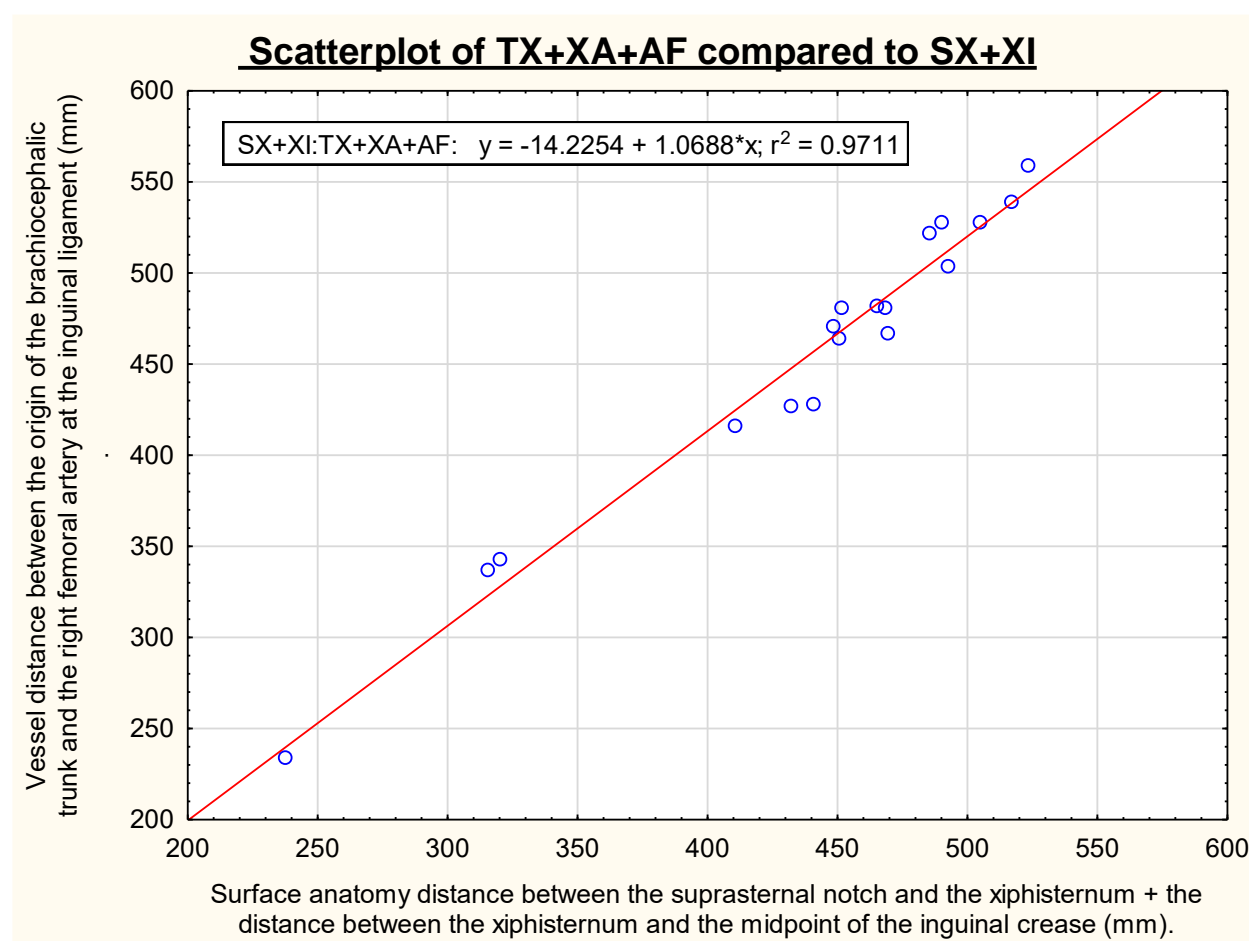


Figure 3.8: Relationship between vessel distance TX+XA+AF (origin of the brachiocephalic trunk to the right femoral artery at the inguinal ligament) and the surface anatomy distance SX+XI (suprasternal notch to the xiphisternum, plus xiphisternum to the midpoint of the right inguinal crease) in children younger than 18 years. Linear regression analysis showed a very strong positive correlation ($r^2 = 0.97$).

3.1.7 Scatterplot of TX+XA+AF compared to SX+XU+UI

Seventeen archived CT scans were used for this comparison, with the youngest person being one year old and the oldest being eighteen years old.

Linear regression analysis showed a significant relationship between the surface anatomy measurements (SX+XU+UI) and vessel measurements (TX+XA+AF). There was a positive correlation between the two variables ($r^2 = 0.97$, $p < 0.001$). A scatterplot summarizes the results (Figure 3.9).

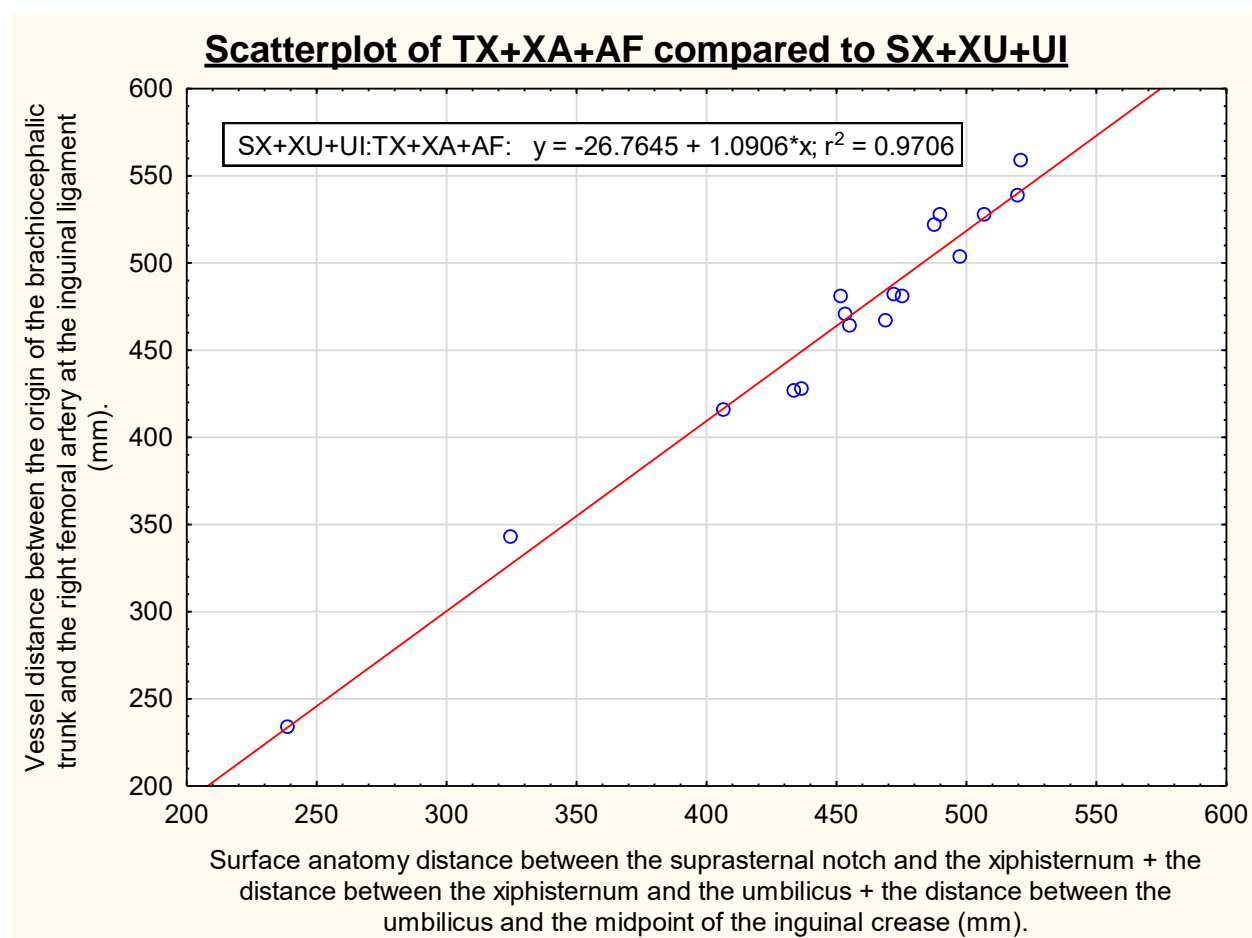


Figure 3.9: Relationship between vessel distance TX+XA+AF (origin of the brachiocephalic trunk to the right femoral artery at the inguinal ligament) and the surface anatomy distance SX+XU+UI (suprasternal notch to the xiphisternum, plus xiphisternum to the umbilicus, plus umbilicus to the midpoint of the right inguinal crease) in children younger than 18 years. Linear regression analysis showed a very strong positive correlation ($r^2 = 0.97$).

3.2 Summary of results

Table 3.2: Summary outcome of each comparison.

Comparison	n	r²	p-value
TC+CD+BE compared to AS	67	0.92	<0.0001
TX compared to SX	152	0.84	<0.0001
XA+AF compared to XI	105	0.99	<0.0001
XA+AF compared to XU+UI	107	0.99	<0.0001
TX+XA+AF compared to SI	18	0.98	<0.0001
TX+XA+AF compared to SX+XI	18	0.97	<0.0001
TX+XA+AF compared to SX+XU+UI	17	0.97	<0.0001

The reader will recall that the data sets and respective comparisons are represented as follows:

Large vessel measurement	Corresponding surface anatomy measurements		
TC	AS		
CB			
BE			
TX	SI	SX	
XA		XI	XU
AF			UI

The aim of the current study was to estimate the true intraluminal distance travelled by pulse wave, which is equal to:

$$(TX+XA+AF) \text{ minus } (TC+CD+BE)$$

This may be estimated using the following component surface anatomy distances:

- $(TC+CD+BE)$ is fairly accurately estimated by AS ($r^2 = 0.92$, $p < 0.0001$).
- $(TX+XA+AF)$ is accurately estimated by either SI, $(SX+XI)$ or $(SX+XU+UI)$, ($r^2 > 0.98$, $p < 0.0001$ for all).

Therefore, the true intraluminal distance travelled by pulse wave may be reasonably estimated by the following (in descending order of r^2):

$$SI - AS$$

$$(SX+XI) - AS$$

$$(SX+XU+UI) - AS$$

CHAPTER 4

4.1 Discussion

The present study was designed to investigate the most accurate estimation of distance travelled by the aorto-femoral pressure wave, using surface anatomy landmarks in children of varying ages. Currently there is no simple validated, non-invasive method to accurately estimate large vessel lengths, for the purpose of PWV calculations. In adult patients (who are no longer growing in height), the inaccuracy of this estimation method is irrelevant because the true distance travelled will not change between one visit and the next. Therefore, a change in transit time in adults reliably reflects a change in large arterial wall stiffness and thereby indicates progression of atherosclerotic vascular disease. However, in growing children and adolescents, the distance travelled by the pulse wave may change between one visit and the next. Therefore, a change in transit time in children or adolescents does not necessarily indicate a change in pulse wave velocity.

The main findings of our study was that there is excellent correlation between all surface anatomy distances and their respective vessel distances. However, each set of surface anatomy measurements requires adjustment using the formulae that we have provided, to more closely estimate the true distance travelled by the pulse wave.

Our results indicate that the combination of surface anatomy measurements that most accurately estimates the true distance travelled by the aorto-femoral pressure wave is the surface distance between the suprasternal notch to the midpoint of the right inguinal crease (SI). This distance estimation requires the surface anatomy distance between the angle of the mandible (right) to the suprasternal notch (AS) to be subtracted to calculate the actual distance travelled between the arrival of the pulse wave at the external carotid sensor, and its arrival at the femoral sensor.

Our results are consistent with previous research that compared non-invasive PWV and invasive PWV, in order to assess the distance travelled by the aorto-femoral pressure wave. The authors concluded that the best agreement between non-invasive PWV and invasive PWV was found, when they used the surface measurements, SI minus AS (Weber, Ammer, Rammer, Adji, O'Rourke, Wassertheurer, Rosenkranz, Eber, Bernd: 2009).

More recent research by Németh et al (2011) concluded that “PWV calculated using suprasternal notch-to-femoral distance minus suprasternal notch-to-carotid distance provides the strongest relationship to cardiovascular mortality.”

However, the results from other research done in adults by Sugawara et al (2008), where the authors compared the MRI-derived arterial length with the surface anatomy measurements typically performed for the PWV, indicated that the carotid-suprasternal notch distance be subtracted from carotid-femoral distance, provided the closest approximate in adults.

The above mentioned studies and other studies with similar aims (Weir-McCall, et al: 2018) (Huybrechts, et al: 2011) were all done in adults. Our work is novel, because to the best of our knowledge, this is the first study of its kind in growing children and adolescents.

It is important to note that the surface distances obtained in the current study are identical to distances one would obtain when using a sliding caliper. The issue of morbid obesity with regards to PWV distance measurement might be overcome by using a sliding caliper instead of a tape measure (Levi-Marpillat, Desamericq, Akakpo, Affes-Ayadi, Tropeano, Millasseau, MacQuin-Mavier: 2013).

Our study had several limitations. First, although our results showed a very strong correlation between the surface anatomy measurements and their respective vessel measurement, the sample size was limited, particularly for comparisons requiring long scans stretching from the neck to the pelvis. We overcame this by comparing subsections of vessel distances (SX compared to TX and XI compared to XA+AF). However, the correlation between SX and TX was not as strong as the other comparisons ($r^2 = 0.84$ versus $0.92 - 0.99$); the reason for this may be related to morphological variability in aortic arch anatomy or the different age range of participants (median 6 versus 13 – 15 years of age). When this distance is combined with others into longer sections (such as SX+XI and TX+XA+AF), the magnitude of the error is reduced and correlations improve.

Second, the surface anatomy measurements were performed using 3D volume rendered images. In a future study, the surface anatomy measurement could be performed on actual patients face-to-face, and then compared to the vessel length obtained from CT imaging. Third, we evaluated the anatomic measurements using only one MPR imaging software. Repeating the study using

different software may be necessary to verify findings. Fourth, we were unable to determine whether there were any systematic racial differences in the measurements, because ethnicity information was not available. Fifth, although we measured the length of the centerline of large vessels, we did not measure the internal diameter of the vessel, which may confound the speed at which the aorto-femoral pressure wave travels. The latter was beyond the scope of the present study.

CHAPTER 5

5.1 Conclusion

Equations obtained in the regression analyses will allow other investigators to obtain an accurate estimation of the true distance travelled by the aorto-femoral pressure wave. This will result in a more reliable PWV calculation in growing children and adolescents. More robust and accurate measurement of PWV will in turn enable healthcare workers to detect atherosclerosis in its early stages and allow for early interventions to prevent vascular events such as strokes and heart attacks later in life. Finally, our findings will enable more robust inter-study comparisons of carotid-femoral PWV data in children and adolescents.

Ultimately, the surface anatomy distance between the suprasternal notch and the angle of the mandible, subtracted from the distance between the suprasternal notch and mid-inguinal crease, provides the closest approximation of true intraluminal distance travelled and would be the best method to standardize pulse wave velocity calculation in children and adolescents. However, surface anatomy estimations using the xiphisternum and umbilicus as landmarks, produced very similar correlations.

6. References

1. Backhouse, K.M. & Hutchings, R.T. 1998. *Clinical surface anatomy*. 2nd ed. London: Mosby.
2. Bushong, S.C. 2001. *Radiologic science for technologist: physics, biology and protection*. 7th ed. St Louis: Mosby Inc.
3. Bushong, S.C. 2004. *Radiologic science for technologist: physics, biology and protection*. 8th ed. St Louis: Mosby Inc.
4. Bushong, S.C. 2013. *Radiologic science for technologist: physics, biology and protection*. 10th ed. St Louis: Mosby Inc.
5. Calhoun, P. S., Kuszyk, B.S., Heath, D.G., Carley, J.C., Fishman, E.K. 1996. Volume rendering of peripancreatic vasculature using biphasic spiral CT data. *Academic Radiology*, 3(12):1057
6. Cunningham, I.A. & Judy, P.F. 2000. *The Biomedical Engineering Handbook*. 2nd ed. CRC Press LLC: Boca Raton
7. El-Khoury, G.Y., Bennett, L.D., & Ondr, G.J. 2004. Multidetector-row computed tomography. *Journal of the American Academy of Orthopaedic Surgeons*, 12(1): 1-5
8. Hong, Y. 2010. Atherosclerotic cardiovascular disease beginning in childhood. *Korean Circulation Journal*, 40(1). <http://www.ncbi.nlm.nih.gov/pmc/articles/PMC2812791> [06 October 2015]

9. Huybrechts, S.A., Devos, D.G., Vermeersch, S.J., Mahieu, D., Achten, E., de Backer, T.L., Segers, P., van Bortel, L.M. 2011. Carotid to femoral pulse wave velocity: a comparison of the real travelled aortic path lengths determined by MRI and superficial measurements. *J Hypertens.* 29:1577-1582.
10. IntelliSpace Portal. Version 4.0.3.10012. October 2012. Koninklijke Philips Electronics: Netherlands.
11. Isokangas, J.M., Hietala, R., Perälä, J., Tervonen, O. 2003. Accuracy of computer-aided measurements in endovascular stent-graft planning: an experimental study with two phantoms. *Investigative Radiology*, 38(3): 164-70.
12. Laurent, S., Cockcroft, J., Van Bortel, L., Boutouyrie, P., Giannattasio, C., Hayoz, D., Pannier, B., Vlachopoulos, C., Wilkinson, I., Struijker-Boudier, H. 2006. Expert consensus document on arterial stiffness: Methodological issues and clinical applications. *European Heart Journal*, 27(21): 2588-2605.
13. Levi-Marpillat, N., Desamericq, G., Akakpo, S., Affes-Ayadi, H., Tropeano, A., Millasseau, S., MacQuin-Mavier, I. 2013. Crucial Importance of using a sliding calliper to measure distance for carotid-femoral pulse wave velocity assessment. *Journal of Hypertension*, 31(5): 940-45.
14. Lumley, J. 2002. *Surface anatomy, the anatomical basis of clinical examination*. 3rd ed. London: Elsevier Limited.
15. Mayo Clinic, n.d. *Arteriosclerosis/atherosclerosis*. <https://www.mayoclinic.org/diseases-conditions/arteriosclerosis-atherosclerosis/symptoms-causes/syc-20350569> [06 October 2015]

16. Moore, K.L., Dalley, A.F. & Agur, A.M.R. 2014. *Clinically Oriented Anatomy*. 7th ed. Philadelphia: Lippincott Williams & Wilkins.
17. Moses, K.P., Banks, J.C., Nava, P.B. & Petersen, D. 2005. *Atlas of clinical gross anatomy*. Philadelphia: Elsevier Limited.
18. Németh, Z.K., Studinger, P., Kiss, I., Othmane, T., Nemcsik, J., Fekete, B.C., Deák, G., Egresits, J., Szathmári, M., Tislér, A. 2011. The Method of Distance Measurement and Torso Length Influences the Relationship of Pulse Wave Velocity to Cardiovascular Mortality. *American Journal of Hypertension*, 24(2): 155-61.
19. Parker, D. 2003. *Selly Oak Imaging, Diagnostic and Interventional procedures*. <http://www.nhs.sellyoakhospital/imaging/cta/ctb/gov/2003.pdf> [June 2005].
20. Patton, K., Thibodeau, G. & Douglas, M. 2012. *Essentials of Anatomy and Physiology*. St. Louis: Mosby Inc.
21. Prokop, M. & Galanski, M. 2003. *Spiral and Multislice Computed Tomography of the Body*. New York: Thieme.
22. Radiology info.org. 2015. *CT Angiography (CTA)*. <http://www.radiologyinfo.org/en/info.cfm?pg=angiact> [06 October 2015].
23. Ross, M.H. & Pawlina, W. 2006. *Histology: a text and atlas*. 5th ed. Philadelphia: Lippincott Williams and Wilkins.

24. Roth, G. A., Johnson, C., Abajobir, A., Abd-Allah, F., Abera, S. F., Abyu, G., et al. 2017. Global, Regional, and National Burden of Cardiovascular Diseases for 10 Causes, 1990 to 2015. *Journal of the American College of Cardiology*, 70(1): 1-25.
25. Sugawara, J., Hayashi, K., Yokoi, T., Tanaka, H. 2008. Age-Associated Elongation of the Ascending Aorta in Adults. *Journal of the American College of Cardiology*, 1(6): 739-748.
26. Tortora, G. J., & Derrickson, B. 2011. *Principles of Anatomy & Physiology*. 13th ed. Asia: John Wiley & Sons, Inc.
27. Tortora, G. J., & Grabowski, S. 2003. *Principles of Anatomy & Physiology*. 13th ed. Asia: John Wiley & Sons, Inc.
28. Weber, T., Ammer, M., Rammer, M., Adji, A., O'Rourke, M. F., Wassertheurer, S., Rosenkranz, S., Eber, B. 2009. Noninvasive determination of carotid-femoral pulse wave velocity depends critically on assessment of travel distance: a comparison with invasive measurement. *Journal of Hypertension*, 27(8): 1624-1630.
29. Weir-McCall, J.R., Brown, L., Summersgill, J., Talarczyk, P., Bonnici-Mallia, M., Chin, S.C., Khan, F., Struthers, A.D., Sullivan, F., Colhoun, H.M., Shore, A.C., Aizawa, K., Groop, L., Nilsson, J., Cockcroft, J.R., McEniery, C.M., Wilkinson, I.B., Ben-Shlomo, Y., Houston, J.G. 2018: Development and Validation of a Path Length Calculation for Carotid-Femoral Pulse Wave Velocity Measurement A TASCFORCE, SUMMIT, and Caerphilly Collaborative Venture. *Hypertension*.
30. Young, B., O'Dowd, G. & Woodford, P. 2014. *Wheaters functional histology: a text and colour atlas*. 6th ed. Philadelphia: Elsevier